

Extrusion-based Additive Manufacturing of Silicone Elastomer Parts

by

Jeffrey S. Plott

A dissertation submitted in partial fulfillment
of the requirements for the degree of
Doctor of Philosophy
(Mechanical Engineering)
in The University of Michigan
2017

Doctoral Committee:

Professor Albert J. Shih, Chair
Professor Thomas J. Armstrong
Assistant Professor Kira L. Barton
Assistant Research Scientist Grant H. Kruger
Assistant Research Scientist Kenneth A. Shorter
Dr. Bizhong (Rocky) Zhu, Dow Performance Silicones

Jeffrey S. Plott
plottjs@umich.edu
ORCID iD: 0000-0002-9479-9428

© Jeffrey S Plott 2017
All Rights Reserved

DEDICATION

To my family for their never ending support in my endeavors, my advisor, Professor Albert Shih, for giving me the flexibility to pursue my dreams, and my committee for their encouragement and guidance.

ACKNOWLEDGMENTS

There is no way to acknowledge every person who provided support and help along my journey through this doctorate degree. Nevertheless, I will make an attempt.

First I would like to thank my advisor, Professor Albert Shih. Throughout our years of working together he has created many unique opportunities for me, supported whatever projects I might decide to pursue, always looks out for my best interest, and provides the gentle reminder to “publish or perish”. For that I am forever thankful.

I would also like to thank my numerous lab mates who assisted me with experiments and shared their expertise with me including (in no particular order): Bruce Tai, Roland Chen, Barry Belmont, Michihiro Kanie, Yang Liu, Bagus Dhamantra, Xiaoqing Tian, Mengyao Ruan, Thuan Doan, David Hodgson, Leo Tse, Robert Chesina, Deokkyun Yoon, Dian-Ru Li, and Yu’an Jin. I would like to extend a special thanks to Xiaoqing Tian for her assistance in the data collection and analysis of the tensile test and force measurement studies (Chapters 3 and 4) and Yang Liu for his CFD modeling expertise (Appendix A).

I would also like to acknowledge the support from Dow Corning and Dow Performance Silicones, in particular Rocky Zhu, Herschel Reese, Sara Schaubroeck, and Zach Milroy, for sharing their silicone expertise with me and providing the support to start this research.

Thank you to the University of Michigan Coulter Translational Research Partnership Program, particularly Tom Marten, for their financial support throughout and for providing me a creative design outlet anytime this research became too frustrating.

Additional thanks to the National Science Foundation (CMMI Grant # 1522877) for their partial support of this research.

Finally I would like to thank my committee for their guidance and suggestions during this research.

TABLE OF CONTENTS

DEDICATION	ii
ACKNOWLEDGMENTS	iii
LIST OF FIGURES	viii
LIST OF TABLES	xiii
ABSTRACT	xiv
CHAPTER 1	
INTRODUCTION	1
1.1 Motivation.....	1
1.2 Research Goal and Objectives	4
1.3 Organization of the Dissertation	5
CHAPTER 2	
THE EXTRUSION-BASED ADDITIVE MANUFACTURING OF MOISTURE-CURED SILICONE ELASTOMER WITH MINIMAL VOID FOR PNEUMATIC ACTUATORS	6
2.1 Introduction.....	6
2.2 Material and Experimental Setup.....	9
2.2.1 Silicone Material Specifications	9
2.2.2 Experimental Setup.....	10
2.2.3 Experiment Design.....	11
2.3 Exp. I: Single-Line Wall.....	15
2.4 Exp. II: Solid.....	19
2.5 Exp. III: Double-Line Wall.....	20

2.6 Exp. IV: Bridging.....	22
2.7 Exp. V: Sphere-Like Balloon.....	27
2.8 Exp. VI: Finger Pneumatic Actuator	30
2.9 Conclusions.....	34
CHAPTER 3	
VOIDS AND TENSILE PROPERTIES IN EXTRUSION-BASED ADDITIVE	
MANUFACTURING OF MOISTURE-CURED SILICONE ELASTOMER.....	
36	
3.1 Introduction.....	36
3.2 Silicone Material and Experimental Setup	39
3.2.1 Silicone Material and Cure Parameters.....	39
3.2.2 AM Machine and Setup	40
3.2.3 Tensile Test Specimen Fabrication.....	41
3.2.4 Tensile Testing Machine and Test Parameters	45
3.3 Voids in Tensile Specimens.....	46
3.3.1 Baseline Sheet Stamped.....	46
3.3.2 AM Specimens with $X = 1.00$	47
3.3.3 AM Specimens with $X = 0.97$	48
3.3.4 AM Specimens with $X = 0.91$	50
3.4 Tensile Testing Results.....	51
3.5 Failure Analysis	52
3.5.1 Deformation of Voids	52
3.5.2 Fracture Surface Analysis	54
3.6 Conclusions.....	60
CHAPTER 4	
MEASUREMENT AND MODELING OF FORCES IN EXTRUSION-BASED	

ADDITIVE MANUFACTURING OF MOISTURE-CURED SILICONE	
ELASTOMER	62
4.1 Introduction.....	62
4.2 Forces in Extrusion-based AM	66
4.3 Experimental Setup.....	67
4.3.1 Silicone Material and Cure Parameters.....	68
4.3.2 AM Machine and Setup	68
4.3.3 Experimental Design.....	70
4.3.4 Displacement to Force Conversion	73
4.4 Results.....	77
4.4.1 Cantilever beam displacements.....	78
4.4.2. Experimental Results of F_t	78
4.4.3. Experimental Results of F_n	83
4.4.4. Comparison of Results.....	85
4.5 Conclusions.....	86
CHAPTER 5	
EXTRUSION-BASED SILICONE ADDITIVE MANUFACTURING GUIDELINES	
.....	88
5.1 Introduction.....	88
5.2 Solid Base Section	88
5.3 Support-less Bridging	90
5.4 Tall/Thin Walled Structures.....	92
5.5 Hollow Silicone AM Hand Example	96
5.6 Conclusions.....	97
CHAPTER 6	
CONCLUSIONS AND FUTURE WORK.....	99

6.1 Conclusions and Major Contributions	99
6.2 Future Work	101
APPENDIX A	
CFD Modeling	103
A.1. Silicone Extrusion CFD Model.....	103
A.2 Governing equations and boundary condition in a moving reference frame ...	104
A.3 Numerical method.....	105
A.4. CFD Results	106
REFERENCES	109

LIST OF FIGURES

Figure 1.1: Hardness scale chart of soft materials [2].	1
Figure 1.2: (a) Lead screw positive displacement extrusion [17], (b) air pressure extrusion [18], and (c) progressive cavity pump extrusion (this research study) [19].	4
Figure 2.1: Experimental setup for extrusion-based silicone AM: legends: (1) motion control platform, (2) progressive cavity pump and controller, (3) pressurized syringe barrel, (4) tapered nozzle, (5) enclosed build chamber, and (6) humidifier.	11
Figure 2.2: (a) Voids at the intersection of extrusion lines in silicone AM and elliptical cross-sectional lines. (b) Horizontal and vertical overlaps used to fill the void through material compression. (c) The layer height t and line spacing c which determines the rectangular cross-sectional area of the deformed extrusion lines.	13
Figure 2.3: Exp. I. the single-line wall: (a) overview and (b) steady-state cross-section.	15
Figure 2.4 Cross-sectional images (under 5x magnification) of the 10-layer tall single-line silicone AM wall, “X” denotes failed silicone AM. Images are scaled equally. Only the first 8 layers are shown for 0.28 mm layer height specimens.	17
Figure 2.5: Cross-sectional images of (a) $Q = 0.14$ ml/min, $t = 0.14$ mm, and $d_i = 0.84$ mm with large taper (1 st layer width = 1.09 mm and 10 th layer width = 0.60 mm) and (b) $Q = 0.10$ ml/min, $t = 0.28$ mm, and $d_i = 0.41$ mm with nearly identical layers including no overall taper and layer edges showing large indentations (crest = 0.35 mm wide and trough = 0.22 mm wide).	19
Figure 2.6: A solid silicone AM test part with six 50 mm long adjacent lines and $n_{height} = 10$ to study the compression factor X : (a) configuration and (b) cross-section view.	19
Figure 2.7: Cross-section of the steady-state region of Exp. II Solid with (a) $X = 1.02$ overview, (b) close-up view with small voids in top layers due to less compression, and (c) $X = 1.16$ overview with no void and some over-extrusion.	20
Figure 2.8: Two adjacent silicone lines, 50 mm long, and $n_{height} = 10$ to study the effect of c_{edge} on the thin double-line wall.	21

Figure 2.9: Cross-section of the double-line wall with (a) $X = 1.02$ and $c_{edge} = 0.48$ mm with voids and (b) $X = 1.16$ and $c_{edge} = 0.42$ mm with no void and taper at the base (initial layers).....	21
Figure 2.10: Key process parameters for parametric stair-stepping in bridging.....	22
Figure 2.11: Bridging test specimen, with dimensions (unit: mm), for Test 5 part: (a) perspective view, (b) side view, (c) cross-section view of A-A, (d) top view, and (e) close-up view of the base and bridge.....	25
Figure 2.12: Bottom view of the bridging in Exp. IV Test 5 specimen.....	26
Figure 2.13: Cross-sectional view of the Exp. IV Test 5 specimen: (a) overview and (b) close-up view showing the onset of successful bridging.....	26
Figure 2.14: Sphere-like silicone balloon: (a) dimensions (unit: mm), (b) base, and (c) curved double-line wall.	28
Figure 2.15: Burst pressure test of sphere-like balloon: (a) the 25.9 mm initial diameter measured with a caliper and (b) the inflated close-to-rupture balloon with the diameter measured using the pixel-distance correlation of the image.	29
Figure 2.16: Finger pneumatic actuator test specimen, with dimensions (unit: mm), for fatigue testing: (a) perspective view and XYZ coordinate system, (b) side views, (c) cross-section view of B-B, (d) cross-section view of C-C.	31
Figure 2.17: Silicone AM of the finger pneumatic actuator: (a) thin-wall vertical structure and (b) and (c) using the bridging technique in Test 5 of Exp. IV to close the horizontal gap with an air tight seal.	32
Figure 2.18: Finger pneumatic actuator in a (a) non-articulated and (b) fully articulated configurations.	33
Figure 2.19: Failures of the finger pneumatic actuator due to a small tear formed near the bottom or top surface.....	34
Figure 3.1: Experimental setup for extrusion-based silicone AM including: (1) motion control platform, (2) progressive cavity pump and controller, (3) pressurized syringe barrels, and (4) tapered nozzle.....	41
Figure 3.2: Sample cross-section including concentric outlines (right side) and infill (left side) along with key process parameters for extrusion-based silicone AM.	42

Figure 3.3: Tool paths for tensile test specimens with a variety of infill angles and outlines, capturing the common solid geometries found in extrusion-based AM of silicone. Infill orientation is with respect to the long axis of the specimen. 45

Figure 3.4: Tensile test machine with the silicone tensile specimen and ink markings for strain measurement under the (a) no strain and (b) 670% engineering strain conditions..... 46

Figure 3.5: Stamped baseline specimen from a cast sheet of material. Spots are from dust particles. 47

Figure 3.6: Detailed top-view of AM Specimens with $X = 1$ (a) 90° , (b) $\pm 45^\circ$, (c) 0° -O, and (d) 0° -NO along with (e) cross sectional view of 0° -NO. 48

Figure 3.7: Detailed bottom-view of AM Specimens with $X = 0.97$ (a) 90° , (b) $\pm 45^\circ$, (c) 0° -O, and (d) 0° -NO along with (e) cross sectional view of 0° -NO. The bottom surface is shown to more easily quantify void size..... 49

Figure 3.8: Detailed bottom-view of AM Specimens with $X = 0.91$ (a) 90° , (b) $\pm 45^\circ$, (c) 0° -O, and (d) 0° -NO along with (e) cross sectional view of 0° -NO. The bottom surface is shown to more easily quantify void size..... 50

Figure 3.9: The maximum tensile strength of each specimen. The stronger specimens (stamped, 90° and $\pm 45^\circ$, $X = 1$ and 0.97) all show a large range of strengths while the weaker specimens tend to show less strength variability. A drop-off in maximum strength was observed in all $X = 0.91$ specimens..... 51

Figure 3.10: Voids in tensile test specimens under tension: (a) 90° ($X = 0.97$), (b) $\pm 45^\circ$ ($X = 0.97$), (c) 90° ($X = 0.91$), (d) $\pm 45^\circ$ ($X = 0.91$), (e) 0° -O ($X = 0.97$), and (f) 0° -NO ($X = 0.97$). 53

Figure 3.11: Failure surface of the (a) 0° -O and (b) 0° -NO specimens. All specimens of this infill type failed in a similar manner regardless of void size..... 54

Figure 3.12: Optical microscopy images of the cross-sectional and top views of failure tensile specimen surfaces (cont.)..... 56

Figure 4.1: Tall soft silicone parts enabled by low force extrusion-based AM (left: high and right: low force in silicone extrusion)..... 63

Figure 4.2: Free body diagrams of the extrusion-based AM forces between the silicone fluid and deposit layer (or build plate) with increasing flowrate, from Q_1 to Q_4 , at a constant layer height, t , and nozzle velocity, v 67

Figure 4.3: Experimental setup for extrusion-based silicone AM including: (1) delta robotic motion control platform, (2) progressive cavity pump and controller, (3) pressurized syringe barrels, (4) tapered nozzle, (5) cantilevered plate, and (6) laser displacement sensor. 69

Figure 4.4: The (a) perspective and (b) side views of the single line wall rounded-edge square part for experimental force measurement (25 mm × 25 mm × 3 mm) with 4 mm corner radius..... 70

Figure 4.5: A rounded-edge square shape silicone part built on the cantilever beam. The displacement of the beam is measured by the laser displacement sensor (sample data in (f)). F_n is measured from points D₂ to A₁ and B₂ to C₁; F_t is measured at points M₁ and M₂..... 72

Figure 4.6: (a) Free body diagram of force vs. displacement calibration of the cantilever beam. A known mass generates a coupled moment M at the free end of the beam which creates displacement x_1 . (b) Free body diagram of the force imparted on the cantilever beam due to the F_t . (c) Free body diagram of the force imparted on the cantilever beam due to F_n . 73

Figure 4.7: Calibration curve to convert cantilever beam displacements to F_t and F_n 74

Figure 4.8: Theoretical F_{nd} for each set of process parameters in this study..... 76

Figure 4.9: Theoretical F_{ng} for each set of process parameters in this study..... 77

Figure 4.10: Displacement vs time graph for the following AM process parameters: $Q = 0.34$ ml/min, $t = 0.15$ mm, and $d_i = 0.41$ mm. 78

Figure 4.11: Selected displacement data including 20 peaks (10 layers) and the least squares fit to find the points M₁ and M₂. 79

Figure 4.12: The average and standard deviation of F_t for three nozzles ($d_i = 0.41, 0.25,$ and 0.20 mm) at three layer heights ($t = 0.20, 0.15,$ and 0.10 mm). 80

Figure 4.13: High-speed camera images taken during the extrusion process and corresponding cross-sectional images taken after curing with $d_i = 0.25$ mm, $t = 0.15$ mm, and $Q =$ (a) 0.22, (b) 0.28, (c) 0.34, and (d) 0.40 ml/min. As Q increased, the degree to which the nozzle impacts the extruded silicone increases, thereby increasing F_t and wall thickness. 82

Figure 4.14: Displacement vs time graph for experimental F_n measurement: $Q = 0.40$ ml/min, $t = 0.15$ mm, $d_i = 0.25$ mm. Three regions where only F_n acts to deflect the cantilever beam were averaged to determine F_n for a given set of process parameters.	83
Figure 4.15: Displacement vs time graph: $Q = 0.16$ ml/min, $t = 0.15$ mm, $d_i = 0.25$ mm. F_n is undetectable, likely in the μN scale.	84
Figure 4.16: The average and standard deviation of F_n for three nozzles ($d_i = 0.41, 0.25,$ and 0.20 mm) at three layer heights ($t = 0.20, 0.15,$ and 0.10 mm).	85
Figure 4.17: The ratio of F_n to F_t . A larger nozzle size generates a larger F_t than a smaller nozzle when the nozzle is sufficiently close or contacts the extruded silicone bead.	86
Figure 5.1: Example for printing of a solid base section of the hand.	89
Figure 5.2: Toolpath of thin wall support-less bridging.	91
Figure 5.3: Deflection ratio F_n/W_t at various Q . A larger nozzle d_i has a greater tendency for unsupported bridging.	92
Figure 5.4: (a) A 10×10 mm single wall tower used to validate the deflection ratio assumption, F_t/I . (b) The graph of deflection ratio F_t/I at various Q with the maximum tower height before failure denoted on the graph (unit: mm). Coil denotes a process parameter combination where a rope coiling phenomenon was observed.	94
Figure 5.5: Side view (top) and top view (bottom) of tall/thin wall towers with $d_i = 0.41$ mm, $t = 0.10$ mm, and $Q =$ (a) $0.16,$ (b) $0.22,$ and (c) 0.40 ml/min.	95
Figure 5.6: Deflection ratio F_t/W_t at various Q with the maximum tower height before failure denoted on the graph (unit: mm).	96
Figure 5.7: Complete hollow hand produced through extrusion-based silicone AM.	97
Figure A1: Silicone deposition CFD modeling: (a) fluid domain, (b) front view an inertial frame, and (c) in a moving reference frame. (unit: mm).....	104
Figure A2: Top, front, and side view of the mesh.	106
Figure A3: Top view and side view of CFD result of silicone fluid deposited on a rigid build plate with (a) $Q = 0.10$ ml/min and (b) $Q = 0.22$ ml/min. The nozzle is contacting the extruded silicone bead.....	107
Figure A4: Predicted F_t on the rigid build plate from the CFD model for: (a) $Q = 0.10$ ml/min and (b) $Q = 0.22$ ml/min.	107

LIST OF TABLES

Table 1.1: Summary of soft materials for AM. Some values for Shore A hardness, denoted with *, were approximated from the elastic modulus using Gent’s correlation [3,4].....	2
Table 2.1: Key printing parameters used in each experiment.....	12
Table 2.2: Process parameters in the bridging parametric study. Test 5 exhibited the best overall results.	23
Table 2.3: Burst testing results from three sphere-like balloons.	30
Table 3.1: Summary of soft materials for AM. Some values for Shore A hardness, denoted with *, were approximated from the elastic modulus using Gent’s correlation [3,4].....	38
Table 3.2: Key process parameters used to adjust the void size within the part mesostructure. ..	43
Table 3.3: Maximum tensile strength results (in MPa) corresponding to those plotted in Figure 9.	52
Table 4.1: Key AM process parameters used for parametric study.....	70

ABSTRACT

The extrusion-based additive manufacturing (AM) of moisture-cured silicone elastomer parts with minimal voids and high strength, elongation, and fatigue life is presented. Due to the soft deformable nature of silicone, AM is technically challenging; as each layer is extruded, it compresses and deforms previous layers, making process parameter selection difficult and dependent on the AM scenario. This research aims to close this knowledge gap and improve the capabilities of silicone AM.

First, a process parameter selection approach to achieve high strength voidless wall structures through previous layer deformation is presented. Effects of flowrate, layer height, and distance between adjacent silicone lines on the vertical layer deformation and void generation are shown. The results are then applied to create hollow sphere-like balloons and finger pneumatic actuators. The sphere-like balloons exhibited diametric expansion between 152 and 207% with burst stress between 1.46 and 2.55 MPa (comparable to the base material properties) while the pneumatic finger actuators fully articulated over 30,000 cycles before failure.

To quantify the strength impact of internal voids and infill direction on silicone AM parts, the tensile strength and failure modes are investigated in tensile test specimens with various infill directions (0° , $\pm 45^\circ$, and 90° relative to the tensile direction) and internal void sizes. These strength results are then compared to baseline silicone specimens. The AM specimens with $\pm 45^\circ$ and 90° infill direction and either the minimal or small voids had the strongest tensile strength (average between 1.44 and 1.51 MPa). This strength is close to that of the sheet stamped specimens which had an average tensile strength of 1.63 MPa. As voids became larger and more elongated in shape, the average tensile strength significantly reduced to 1.15 and 0.90 MPa for specimens with $\pm 45^\circ$ and 90° infill direction, respectively. Counterintuitively, specimens with 0° infill direction were consistently the weakest due to the tangency voids and sharp corners resulting from the tool path. To maximize the tensile strength, it is important to select process parameters which minimize the elongated voids, infill tangency voids, and surface edges. If these conditions can be achieved, the infill direction does not play a significant role.

Finally, to increase the maximum possible height of silicone AM parts, the tangential and normal forces imparted by the AM process were studied to investigate the effects of three key process parameters: volumetric flow rate, nozzle tip inner diameter, and layer height. The interaction between the nozzle tip and extruded silicone bead is controlled to either prevent any interaction, flatten the top surface of the extruded silicone, or immerse the nozzle in the extruded silicone. Results showed that tangential and normal forces strongly depend on this interaction. Specifically, forces remained low (less than 0.2 mN) if the nozzle tip did not contact with the extruded silicone bead but quickly grew to over 1 mN once the nozzle interaction with extruded silicone came into effect. To reduce these tangential and normal forces, process parameters should be selected to prevent the nozzle tip from dragging through the deposited silicone while maintaining sufficient line width for structural integrity.

These findings create a foundational understanding of the extrusion-based AM of silicone and other soft materials. The results presented can be implemented to enable control strategies which may greatly expand the design freedoms for producing compliant, stretchable, and functional custom silicone parts.

CHAPTER 1

INTRODUCTION

1.1 Motivation

Additive manufacturing (AM) refers to the building of physical 3D geometries by the successive addition of material [1]. AM has transformed the product development process by enabling the economic creation of low volume components and allows for the manufacture of unique custom parts that traditional manufacturing methods cannot physically or cost effectively produce. While much research has been previously performed for AM, there is a lack of understanding for the extrusion-based AM of soft components.

Soft materials with 0 to 100 Shore 00 hardness (Figure 1.1) have broad applications in robotic, consumer, automotive, medical, and other wearable, stretchable, and flexible products such as cushions for energy absorption, actuators, seals, and others.

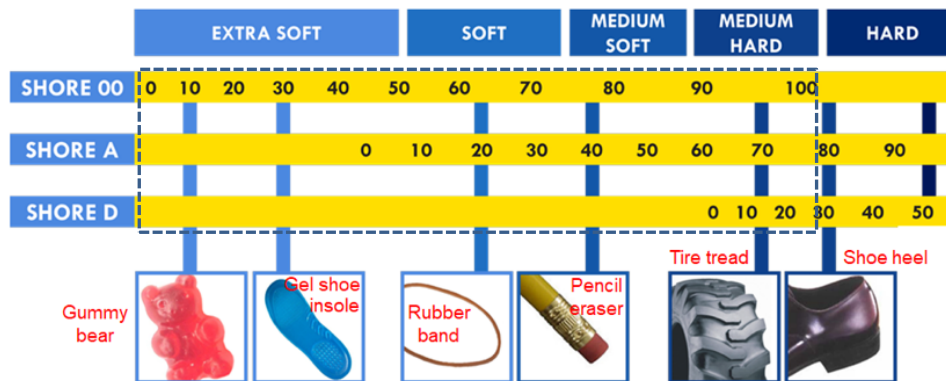


Figure 1.1: Hardness scale chart of soft materials [2].

Molding is the most common fabrication method for parts made of soft materials. Although molding is ideal for high volume production, it has three major barriers. First, the

mold cost is high (often machined from tool steel) and comes with a long lead times. These molds may also require heating or two-part injection, further adding to the mold complexity, cost, and lead time. Second, due to the constraint of demolding, molding cannot fabricate parts with intricate internal features or complex thin wall structures. Third, it is difficult to mold parts with functionally gradient material properties. AM of soft materials can overcome these barriers. A summary of the soft materials in AM is shown in Table 1.1.

Table 1.1: Summary of soft materials for AM. Some values for Shore A hardness, denoted with *, were approximated from the elastic modulus using Gent’s correlation [3,4].

AM Process	Material	Tensile Strength [MPa]	Elongation at Break [%]	Shore A Hardness	Maximum Use Temperature [°C]	Remarks
Selective Laser Sintering	DuraForm Flex [5]	1.8	110	45 – 75	-	Low elongation
Photopolymer Jetting	TangoBlackPlus [6]	0.8 – 1.5	170 – 220	26 – 28	-	Low elongation
	Agilus30 [7]	2.4 – 3.1	220 – 270	30 – 35	-	Low elongation
Stereolithography: Digital light projection	SUV Elastomer [8]	0.9	500	34*	-	Properties depend on formulation. Tensile strength and elongation at break reduce with hardness.
		7.5	1100	65*	-	
	Spot-E resin (Spot-A Materials) [9,10]	2.26 ± 0.71	65 – 140	65	-	Low elongation High hardness ~9 cycle fatigue life
	Carbon Elastomeric Polyurethane 40 [11]	6 ± 1	190 ± 10	68	-	Low elongation High hardness
Extrusion-based: Fused deposition Modeling	NinjaFlex Thermoplastic Polyurethane [12,13]	4	660	85	60	Yield at 65% strain High hardness
Extrusion-based: Direct (this study)	Silicone [14–16]	5 – 11	100 – 1100	3 – 90	-110 – 300	Available in many grades (e.g. food, medical, etc.).
	Dow Corning 737 Silicone	1.2 – 1.8	600 – 710	33	-65 – 177	>100,000 cycle fatigue life [16]

Each soft material in AM has some limitations. For example, most of the current commercially available soft materials for AM [5–7,9–11] have low elongation at break (110-270%). The NinjaFlex thermoplastic polyurethane [12,13] with higher elongation at break (660%) is limited by high hardness (85 Shore A). The SUV elastomer created by blending commercially available materials [8] can achieve a high elongation at break (1100%) but is still limited by high hardness (65 Shore A). This elastomer material blend can also be adjusted to lower the hardness, but the elongation at break quickly deteriorates. Additionally, the maximum operating temperatures of the above materials are typically low (<60°C).

Many silicone elastomers, denoted as silicones hereafter, are readily available and suitable for direct extrusion-based AM with the main requirement being that the material does not self-level or wet-out before curing. This can reduce the cost and barrier to entry while enabling a wide range of material properties such as high elongation at break, high tensile strength, extreme use temperatures, UV and chemical resistance, high fatigue life, hardness ranging from 3-90 Shore A, and other benefits [14–16]. Unfortunately there are many challenges to overcome in direct extrusion of silicone for AM of soft 3D parts.

Several extrusion techniques have been used for extrusion-based AM of silicone. These include the lead screw positive displacement, air pressure, and progressive cavity pump extrusion (the device used in this study), as shown in Figure 1.2.

Lead screw positive displacement extrusion uses a lead screw to advance a plunger of material [17]. Due to the slight compressibility of silicone, shear rate dependence on viscosity, and compliance in the syringes/tubing needed to route the silicone material, delays often occur in flow rates using this technique. This delay makes controlling the silicone flow to fill a small and specific area troublesome. Air pressure extrusion [18] is simple from a mechanical standpoint but lacks the ability to adapt to changing viscosities, making precise flow control difficult. Progressive cavity pumps [19] use the Moineau pump principle for accurate volumetric dispensing of high viscosity fluid with short time delay, making it the ideal for this research.

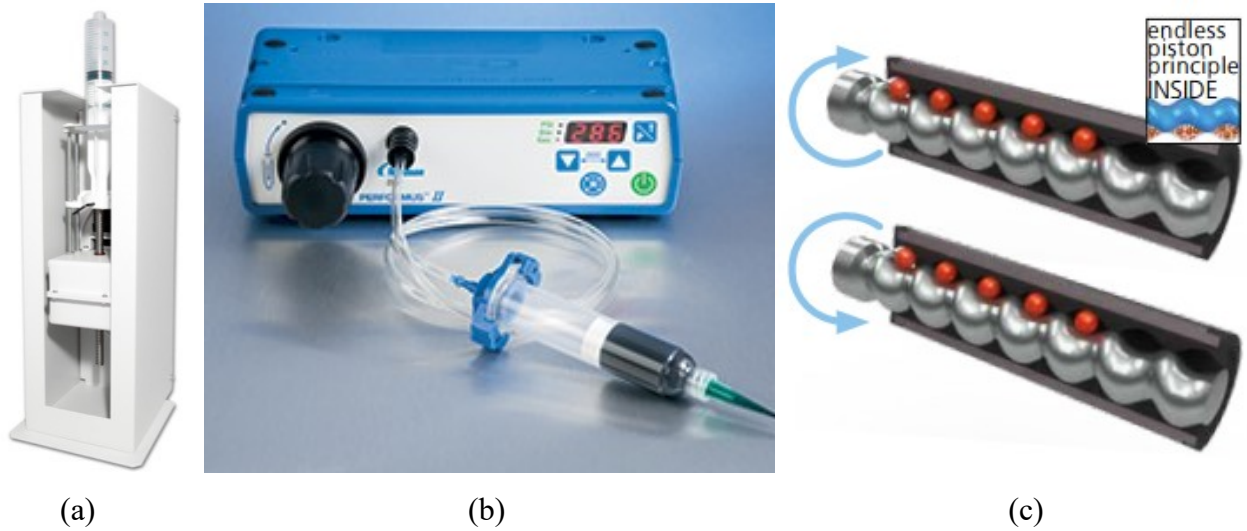


Figure 1.2: (a) Lead screw positive displacement extrusion [17], (b) air pressure extrusion [18], and (c) progressive cavity pump extrusion (this research study) [19].

Although there is great potential to create flexible, high-performance, and functional parts for a wide variety of industries and applications with extrusion-based AM of silicone, there is a need to better understand the AM process parameters and their effects so they can be tailored to increase part performance and expand the potential design space of silicone parts.

1.2 Research Goal and Objectives

The goal of this research is to identify and understand the key aspects of extrusion-based silicone AM, transforming it into a viable process for developing strong, highly flexible parts. To achieve this goal, three objectives are identified:

- (1) Experimentally study the effects of flowrate, layer height, and distance between adjacent silicone lines on the solid and thin-wall vertical layer deformation, void generation, and bridging to close an open area. Use these results to inform and validate a model for rapid process parameter selection.
- (2) Measure the impact of process parameters, specifically the infill direction and adjacent line spacing, on the void formation and maximum tensile strength of parts produced with extrusion-based silicone AM.

- (3) Measure and minimize the tangential and normal forces imparted by the extrusion-based AM of silicone to increase the maximum part height and improve the AM accuracy and reliability.

Achieving these objectives will provide key engineering insights that will significantly improve the extrusion-based AM of silicone and enable the creation of flexible, high-performance, and low cost multi-functional parts.

1.3 Organization of the Dissertation

The rest of this dissertation is organized as follows:

Chapter 2 presents an approach for systematic discovery of silicone AM process parameter combinations to fabricate voidless solid and thin-wall structures. A technique for bridging horizontal ledges in a part is also presented. These techniques are then applied to fabricate sphere-like balloons and finger pneumatic actuators. Functional durability tests are also conducted to demonstrate potentials for this technique.

Chapter 3 details the creation and testing of silicone dumbbell tensile test specimens produced by extrusion-based AM. These specimens are used to measure the impact of process parameters, specifically the infill direction (0° , $\pm 45^\circ$, and 90° relative to the tensile direction) and adjacent line spacing on the void formation and maximum tensile strength of parts produced with extrusion-based silicone AM. These results are compared to non-AM specimens.

Chapter 4 introduces an experimental test setup and CFD model (Appendix A) to measure the tangential and normal forces imparted by the extrusion-based AM of silicone. The four potential extrusion scenarios are presented and the forces acting on the deposit layer are decomposed. The magnitudes of these forces are calculated and minimization strategies are presented.

Chapter 5 summarizes the key process parameter insights discovered in Chapters 2-4 and applies them to the manufacturing of a hollow silicone hand.

Chapter 6 draws the conclusions and summarizes the original contributions of the dissertation. Several topics for future research are also proposed.

CHAPTER 2

THE EXTRUSION-BASED ADDITIVE MANUFACTURING OF MOISTURE-CURED SILICONE ELASTOMER WITH MINIMAL VOID FOR PNEUMATIC ACTUATORS

Nomenclature:

a	Major radius of the cross-section of extruded silicone
b	Minor radius of the cross-section of extruded silicone
c	Distance between two adjacent silicone lines
c_{edge}	Distance between two adjacent silicone lines at edge
d_i	Inner diameter (ID) of nozzle tip
Q	Volumetric flow rate
t	Layer height
n_{wall}	Number of lines in wall thickness
n_{height}	Number of lines in wall height
v	Nozzle speed in the layer

2.1 Introduction

Silicone elastomers are common in automotive, consumer, and medical applications due to their unique material properties which include high elongation to failure (commonly > 500%), softness and compliance in contact, bio-compatibility, thermal and electrical insulation, chemical stability, and resistance to ultraviolet (UV) radiation [20]. Silicone elastomers, denoted as silicone in this paper, are also a common material choice for wearable devices [21–23] and pneumatic actuators in soft robotics [24]. While these soft robotic pneumatic actuators can be designed to generate desired motions, their geometries are limited by the molding process, the most common way to fabricate silicone pneumatic actuators [24,25].

There are no well-established production methods for manufacturing freeform silicone pneumatic parts. Instead, it is common to first machine or additive manufacture (AM) molds which are then filled with silicone and cured in place. Zhao et al. [26] used a rotational casting machine and two to four piece molds to produce spherical, cuboid, and finger-shaped silicone pneumatic actuators. For more complicated hollow silicone pneumatic actuators with freeform internal shape, the molding process is a major technical barrier. Molding and fabrication of the molds can also be time consuming and expensive when only a few parts are needed.

By developing methods for silicone AM, the potential design space for flexible applications requiring high strength, large deformation or elongation, and long fatigue life, such as components for soft robotics, wearable and custom assistive or rehabilitation devices, can be greatly expanded. Several technologies are emerging for silicone AM. One technique uses an inkjet to deposit thin layers of ultraviolet (UV) curable silicone which are cured via UV light and built up layer-by-layer (ACEO, Wacker, Munich, Germany) [27]. Another technique utilizes two-part A/B cure chemistry where silicone part-A is extruded through a nozzle into a bath of silicone part-B. Once extruded, part-A becomes hydrostatically suspended in part-B, curing in place (Fripp Design, Sheffield, UK) [28]. Others have used compressed air pressure [15], positive displacement, or progressive cavity pumps [29] to extrude moisture-cured silicone through a nozzle for AM. These extrusion-based AM methods require silicone deposition on top of previous uncured silicone layers so that inter-layer cross-linking of silicone can occur, chemically bonding the layers together. This cross-linking enables comparable mechanical properties of AM silicone parts to molded silicone parts. Since many silicone materials suitable for extrusion-based AM already exist, costs and barriers to entry are also comparatively low. The technical challenge for pneumatic actuator applications is to control the layer-by-layer extrusion of silicone on the soft, uncured, and weakly supported thin-wall structure. In this study, we investigate the extrusion-based silicone AM for thin-wall pneumatic actuators.

Beyond silicone, other soft materials are currently used in AM. These materials primarily include thermoplastic elastomers (TPE) [5,12] and photopolymer resins [6,10]. TPEs are softened by heat and either extruded through a nozzle via extrusion-based AM or selectively sintered via a laser. Photopolymer resins can be deposited in thin layers via an ink jetting process and cured with light or selectively cured in a resin vat using stereolithography. While these materials and AM methods are established and commercially available, the AM parts typically

have limited elongation (< 220%) [6], poor fatigue life under cyclic loading, and limited softness when compared to moisture-cured silicones.

For silicones to become more widely adopted in extrusion-based AM, additional study of the AM mesostructure is required. A key aspect for achieving AM of silicone parts with comparable mechanical properties to that of molded silicone is to minimize the imperfections, or voids, within the internal structure of the AM parts. Such imperfection can create the stress concentration leading to a tear, causing the part to fail before the predicted yield strength is reached. By eliminating voids within the part, mechanical properties comparable to a traditionally molded silicone part can be achieved. AM research has been conducted to study the process parameters on mechanical strength and porosity in extrusion-based processes, like the fused deposition modeling (FDM) of thermoplastics. Rodriguez et al. [30,31] found that minimizing voids and maximizing bond length can increase the transverse tensile strength of AM parts. The distance between adjacent lines and the extrusion flow rate were major influencers for the void geometry, density, and the inter-layer bonding. Decreasing the distance between adjacent lines reduces the void density and increases the bond length densities in FDM [31]. Longitudinal and transverse strength was increased by 2.9 MPa and 8.4 MPa, respectively, by reducing the void.

Es-Said et al. [32] examined the effects of layer orientation on tensile strength of FDM parts made of acrylonitrile butadiene styrene (ABS). The tensile specimens produced at 0° layer orientation (along the force direction) had the highest strengths. In comparison, those with 90° layer orientation (perpendicular to the force direction) had the lowest strength due to weak interlayer bonding and/or interlayer porosity. Bellini and Güçeri [33] found anisotropic strength results due to different layer directions in FDM specimens for tensile and three-point bending tests. A number of specimens failed prematurely due to intra-laminar defects from excess material on the nozzle dripping onto a layer, inter-laminar defects due to over or under extrusion, and initiation of micro-cracks due to surface roughness. Ahn et al. [34] studied effects of distance between adjacent lines, raster orientation, bead width, color, and build temperature on the tensile strength of FDM parts and compared that to molded parts of the same geometry. All FDM parts had lower tensile strength than the injection molded counterparts. The distance between adjacent lines and raster orientation were two variables significantly affecting the tensile strength. When adjacent lines were overlapped for tensile specimens fabricated in non-axial

directions, a significant improvement in strength was observed so long as excess material build up did not occur. Finally, Mohamed et al. [35] summarized that the distance between adjacent lines, layer thickness, and orientation were the most critical factors for FDM part quality. In summary, our literature survey shows there is a lack of research in process parameters on the internal structure of soft materials, like silicone, in extrusion-based AM.

The material properties of moisture-cured silicone also change during the extrusion-based AM process. After extrusion from the nozzle, the silicone is exposed to atmospheric moisture. This moisture starts to cure and harden the silicone at a rate dependent on the silicone material and the exposure time/humidity in the environment.

This study presents a methodology for identifying and predicting process parameters to fabricate voidless solid and thin-wall structures using extrusion-based AM of moisture-cured silicone. An approach for systematic discovery of layer height, flow rate, feed rate, and adjacent line spacing combinations for silicone AM is first introduced. The infill and tool path strategy are then selected. A technique for bridging horizontal ledges in a part is also presented. These extrusion-based silicone AM techniques are then applied to fabricate sphere-like balloons and finger pneumatic actuators. Finally, functional durability tests are conducted to demonstrate potentials for this technique.

2.2 Material and Experimental Setup

This section outlines the selection of silicone material along with the equipment and calibration procedures for extrusion-based AM of silicone.

2.2.1 Silicone Material Specifications

The silicone material used in this study is a clear, one-part oxime cure silicone elastomer that cures upon exposure to atmospheric moisture (Dow Corning® 737, Dow Corning, Midland, Michigan). It features a durometer hardness of Shore 33A, a skin-over time, or time to develop a firm surface, of 3 to 6 minutes, a tack-free time of 14 minutes, a cure to handling time of 24 hours, and a zero shear rate viscosity of about 62.5 Pa·s [15,36]. These material properties,

along with the thixotropic nature of the silicone, make it an attractive material for extrusion-based AM. Due to the sub-minute layer times of the parts printed in this study, the silicone is assumed to be in an uncured liquid state when analyzing layer-layer interactions. Although only one specific silicone is utilized in this study, other types of silicone may also be suitable as long as they have large enough viscosity to resist wetting out, or self-leveling, before curing and low enough viscosity such that they can be extruded from the nozzle.

2.2.2 Experimental Setup

The experimental setup is shown in Figure 2.1. The system consists of six key components: (1) a motion control platform based on an open-source FDM machine (LulzBot TAZ5 by Aleph Objects, Loveland, Colorado), (2) a progressive cavity pump and its controller (Model preeflow eco-PEN 450 pump and Model EC200 controller by Viscotec, Töging am Inn, Germany) to dispense the silicone with a dosing accuracy of $\pm 1\%$ [29], (3) a clear syringe barrel (Model Optimum by Nordson EFD, Westlake, Ohio) pressurized to 340 ± 30 kPa which feeds the progressive cavity pump with silicone material while preventing the introduction of air bubbles into the silicone, (4) tapered nozzles with 22 gauge (0.41 mm) and 18 gauge (0.84 mm) tips (Model SmoothFlow™ by Nordson EFD, Westlake, Ohio) to deposit the silicone on the build plate, (5) an enclosed chamber to maintain the humidity, and (6) a humidifier to maintain a $\sim 70\%$ relative humidity environment for consistent cure rates. Room temperature was maintained at approximately 22°C . For parts with high layer times, the humidity can be lowered so the uppermost silicone layers do not cure prior to depositing subsequent layers (maximizing interlayer bonding strength). The silicone is extruded on a glass build plate lined with removable wax paper so that the silicone print can be easily removed after curing.

A calibration was run on the progressive cavity pump to ensure accurate volumetric flow rates during extrusion. Initial calibration was achieved by purging all air from the extrusion system, fitting the nozzle tip, and extruding 0.500 g of silicone at a flow rate of 0.20 ml/min. The dispensed silicone was then collected and weighed using a balance (Model HRB 103 by LW Measurements, Santa Rosa, CA) with resolution of 0.001 g. The specific gravity of the silicone, 1.04 [36], was then used to compare the measured and expected weights. Calibration was adjusted until the dispensed weight was within ± 0.001 g of the expected weight. Before each test,

calibration verification was also performed by extruding 0.104 g of silicone with identical nozzle and flow rate as used in the test. The same flow rate tolerance (± 0.001 g of the expected weight) was used to tune the calibration before proceeding with the test.

All silicone AM experiments were performed using the open-source 3D printing console (Printrun Pronterface by Kliment Yanev) to control the 3D printer while Simplify3D[®] (Blue Ash, Ohio) was used for tool path generation.

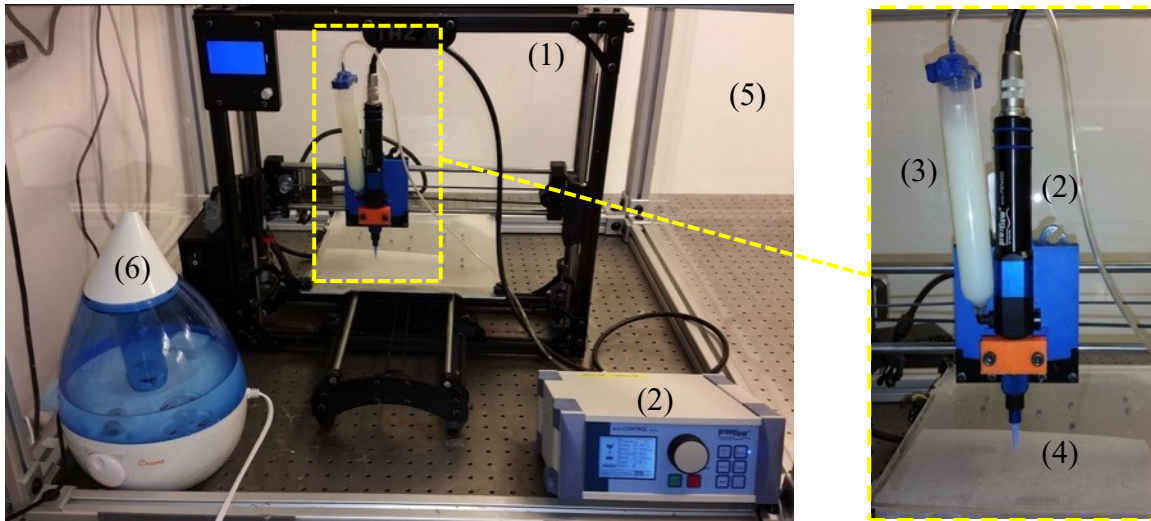


Figure 2.1: Experimental setup for extrusion-based silicone AM: legends: (1) motion control platform, (2) progressive cavity pump and controller, (3) pressurized syringe barrel, (4) tapered nozzle, (5) enclosed build chamber, and (6) humidifier.

2.2.3 Experiment Design

To discover a set of process parameters suitable for extrusion-based silicone AM, six experiments, marked as Exps. I to VI, were performed.

- Exp. I: Single-Line Wall. Single-line walls of silicone were built to study effects of volumetric flow rate (Q), layer height (t), and nozzle inner diameter (d_i) on layer deformation and surface variation.
- Exp. II: Solid. The solid build scenario was evaluated to determine the effect of distance between adjacent infill lines (c) on voids.
- Exp. III: Double-Line Wall. Based on results in Exps. I and II, walls composed of two adjacent silicone lines were built to study the effect of distance between adjacent lines on the edge (c_{edge}) on the layer deformation and void.

- Exp. IV: Bridging. Six process parameters of c , c_{edge} , bridge step-over, number of layers before step over, number of outlines before infill, and the infill overlap with outline were studied on rectangular bridging to create an overhang structure.
- Exp. V: Sphere-Like Balloon. A hollow sphere-like balloon structure was created to evaluate the inter-layer bonding strength and the burst pressure by analyzing the maximum elongation and pressure before break.
- Exp. VI: Finger Pneumatic Actuator. To test the overhang structure (Exp. IV) and inter-layer bonding fatigue strength of a complicated structure, a finger pneumatic actuator with multiple chambers was fabricated and actuated under pulses of pressurized air until fatigue failure took place.

Process parameters for Exps. I to VI are listed in Table 2.1 and will be elaborated in the following sections.

Table 2.1: Key printing parameters used in each experiment.

Variable	Exp. I	Exp. II	Exp. III	Exp. IV	Exp. V	Exp. VI
Q [ml/min]	0.06, 0.08, 0.10, 0.12, 0.14, 0.16, 0.18, 0.20, 0.22	0.12	0.12	0.12	0.12	0.12
t [mm]	0.14, 0.205, 0.28	0.205	0.205	0.205	0.205	0.205
d_i [mm]	0.41, 0.84	0.41	0.41	0.41	0.41	0.41
v [mm/s]	20	20	20	20	20	20
n_{wall}	1	6	2	-	-	-
n_{height}	10	10	10	-	-	-
c [mm]	-	0.42, 0.48	-	0.42, 0.48	0.48	0.48
c_{edge} [mm]	-	-	0.42, 0.48	0.42, 0.48	0.42	0.42
Bridge Step-Over [mm]	-	-	-	0.42, 0.48	0.42	0.42
# Layers before step over	-	-	-	1, 2	2	2
# Outlines before infill	-	-	-	2, 4	4	4
Infill overlap with outline [mm]	-	-	-	0, 0.06	0	0

2.2.4 Process Parameters and Compression Factor for Voidless Extrusion-Based AM

Since many applications of silicone involve high elongation, it is critical to minimize internal voids (or air gaps) as these voids can create stress concentrations and initiate tears in the part. An example of these voids is shown in a cross sectional view of a silicone part fabricated using the extrusion-based AM in Figure 2.2(a). The semi-axes of the elliptical cross-section are a and b . A potential voidless section, as shown in Figure 2.2(b), requires the silicone material to overlap with adjacent extrusion lines, deforming the overlapped material and filling the void. By assuming the silicone volume is conserved and the silicone deformation is symmetrical with respect to the a and b axes during the layer-by-layer extrusion in AM, the overlapped material is deformed such that the elliptical cross section is now rectangular. This is illustrated in Figure 2.2(c) where the overlapped material (red) deforms to fill voided space (blue). Please note that this illustration assumes additional extrusion lines on all exterior sides (not shown). Given a rectangular cross section and the conservation of volume, the required volumetric flow rate (Q) for void filling is calculated by the rectangular area times the nozzle speed (v) where rectangular area equals adjacent line spacing (c) multiplied by layer height (t), as marked in Figure 2.2(c).

$$Q = ctv \quad (2.1)$$

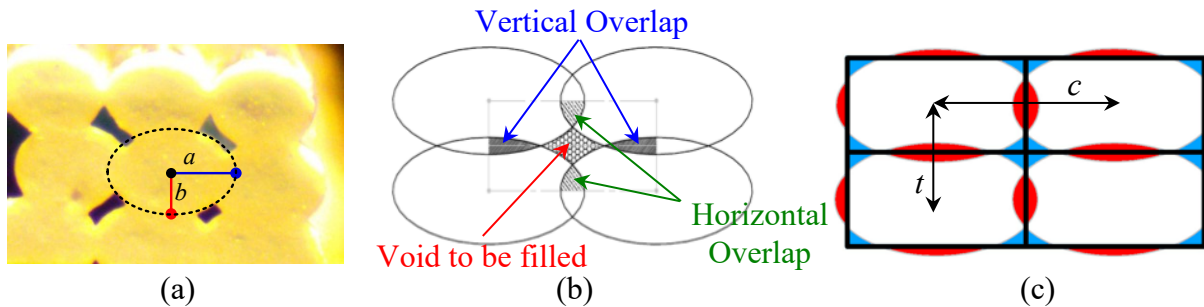


Figure 2.2: (a) Voids at the intersection of extrusion lines in silicone AM and elliptical cross-sectional lines. (b) Horizontal and vertical overlaps used to fill the void through material compression. (c) The layer height t and line spacing c which determines the rectangular cross-sectional area of the deformed extrusion lines.

In practice, since an ideal silicone for extrusion based AM will have sufficient viscosity to self-support and is not free-flowing, a compressive force is required to deform the surrounding

silicone to fill the interstitial space for voidless AM. For the steady-state flow rate in extrusion-based AM with a specific layer height t and constant nozzle speed v , a compression factor X (with value slightly larger than 1.0) is introduced to Eq. (2.1) to artificially lower adjacent line spacing c so the desired compression can be achieved, Eq. (2.2).

$$Xc = \frac{Q}{tv} \quad (2.2)$$

Equation 2.2 can also be re-written so that any value (c , t , v , Q), or combination thereof, may also be adjusted to achieve a given compression factor X . In this study, the value for X is determined based on various empirical silicone extrusion-based AM tests solely by varying c . However, the ideal value for X will be dependent on a number of additional factors neglected in this equation including: (1) the material properties of the extruded silicone, (2) the kinetic energy of the silicone as it leaves the nozzle, (3) the resultant edge profile of the overlapped extrusion lines, and (4) the area of the part where material deposition is occurring. For example, a material with lower viscosity may require a lower compression factor to achieve a voidless cross-section (all else equal) since the uncured liquid silicone will require less force to deform and fill the void. Additionally, if the nozzle outlet diameter is reduced or Q and v are increased proportionally, the exit velocity of the silicone will increase, potentially imparting a larger kinetic energy and greater deforming compression of the previous silicone layers. Also, due to the lack of adjacent line compression on the edge of an AM part, a separate adjustment of the c is required and is replaced by c_{edge} , which is generally less than c . Similarly, when the silicone is extruded against a rigid build plate on its first layer it is likely to deform more than the final top layer which is not compressed by additional extruded layers above, potentially warranting additional compression factors for each situation.

In this study, all outlines and infill were extruded directly on top of one another instead of using cross-hatching patterns. Cross-hatching, or printing at different angles in different layers, is common in FDM because it can act to knit the material together. However, since the silicone is chemically cross-linking (or bonding) at the contact region, cross-hatching is unnecessary for strength and, therefore, not adopted in this study due to the potential complications caused by inconsistent deformation of the silicone as it is extruded over the peaks and valleys of the previous layer. Nozzle speed in the layer, v , was also held constant in all experiments to simplify the experimental process, reduce the potential kinetic energy effects discussed in the previous

paragraph, and minimize potential differences in horizontal dragging forces caused by the AM process.

By utilizing Eq. (2.2) as a tool in conjunction with the experimental approach in the next sections, suitable process parameters for extrusion-based AM can be determined.

2.3 Exp. I: Single-Line Wall

To visualize the layer-layer deformation caused by extrusion based AM of silicone and find suitable process parameters which can be inputs for Eq. (2.2) and extended to more complex shapes, sequential vertical stacking tests of extruded silicone layers to form a single-line wall, as shown in Figure 2.3(a), were performed. Since the silicone undergoes pressure changes as flow is stopped or started and slight silicone buildup can occur on directional changes where the nozzle speed may momentarily decrease, the length of the single-line wall is 50 mm in this study so an equilibrium pressure in the nozzle and steady-state flow of silicone in the central length of the wall is achieved. In practice, equilibrium flow typically occurs within the first 10 mm of constant flow/motion. The number of layers in height is designated as n_{height} . In this experiment, $n_{height} = 10$. After curing, the steady-state zone of the single-line wall was sectioned for analysis.

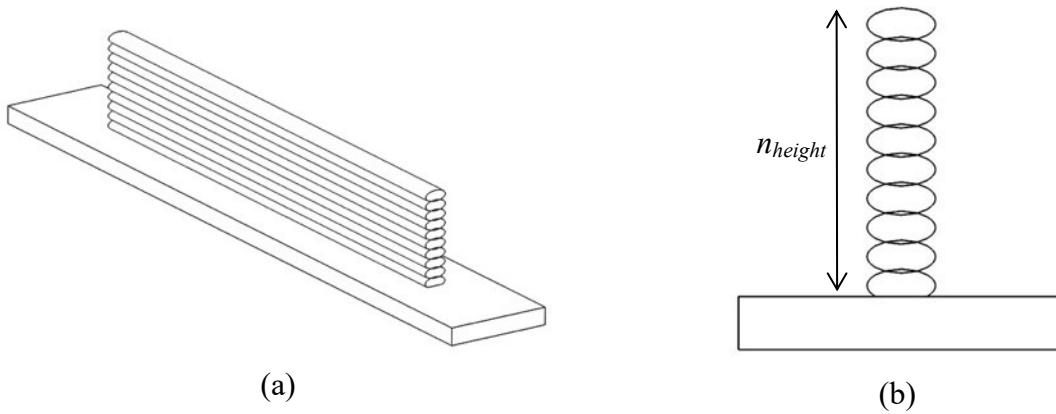


Figure 2.3: Exp. I. the single-line wall: (a) overview and (b) steady-state cross-section.

For this experiment a parametric study, as summarized in Table 2.1, was performed to comprehensively evaluate nine levels of Q (0.06, 0.08, 0.10, 0.12, 0.14, 0.16, 0.18, 0.20, 0.22

ml/min), three levels of t (0.14, 0.205, and 0.28 mm), and two levels of d_i (0.41 and 0.84 mm) on the silicone single-line wall. In total, 54 tests were conducted.

Results of cross-sectional images of single-line walls are shown in Figure 2.4. The moisture-cure silicone used in these experiments remains uncured during AM, allowing the compressive force during extrusion to deform the layers below. This phenomenon is seen to some degree in all tests but is most notable under high Q and low t . For example, with $Q = 0.14$ ml/min, $t = 0.14$ mm, and $d_i = 0.84$ mm, as shown in the close-up view in Figure 2.5(a), the entire cross-section is tapered where the most current layers have deformed and pushed the previous layers outward. On the other extreme, for example with $Q = 0.10$ ml/min, $t = 0.28$ mm, and $d_i = 0.41$ mm, as shown in the close-up view in Figure 2.5(b), a comparatively low normal compressive force is placed on previous layers since there is little deformation of the cross-section. These low normal compressive forces can create significant cross-sectional width variations, which may facilitate voids in subsequent layer-by-layer AM.

To identify process parameters which minimize voids, we looked for cross-sections with (1) minimal vertical taper so that c will be constant regardless of layer number and (2) minimal variation in cross-sectional width to minimize the required deformation of silicone in adjacent lines/layers to fill the voids.

Based on these two criteria, $Q = 0.12$ ml/min, $t = 0.205$ mm, and $d_i = 0.41$ mm is the set of process parameters selected. These are baseline extrusion process parameters for all other experiments in this study. It should be noted that other potential combinations with similar favorable attributes for void minimization exist but were not explored in this study. These specific process parameters may not be suitable for all extrusion-based AM materials but, by following a similar experimental process, they can be quickly discovered. Process parameters could also be adjusted based on the layer height, as described in Section 2.4, to further increase the feasible range of suitable combinations.

t [mm]	$d_i = 0.41$ mm			$d_i = 0.84$ mm		
	0.14	0.205	0.28	0.14	0.205	0.28
Q [ml/min] 0.06		X	X	X	X	X
0.08			X		X	X
0.10	 ↑ 1.4 mm	 ↑ 2.05 mm				
0.12	X Chosen for further study					
0.14	X					

Figure 2.4 Cross-sectional images (under 5x magnification) of the 10-layer tall single-line silicone AM wall, “X” denotes failed silicone AM. Images are scaled equally. Only the first 8 layers are shown for 0.28 mm layer height specimens.








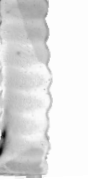





		$d_i = 0.41$ mm			$d_i = 0.84$ mm		
t [mm]		0.14	0.205	0.28	0.14	0.205	0.28
Q [ml/min]	0.16	X			X		
	0.18	X			X		
	0.20	X	X		X		
	0.22	X	X	X	X		

Figure 2.4 Cross-sectional images (under 5x magnification) of the 10-layer tall single-line silicone AM wall, “X” denotes failed silicone AM. Images are scaled equally. Only the first 8 layers are shown for 0.28 mm layer height specimens (cont.).

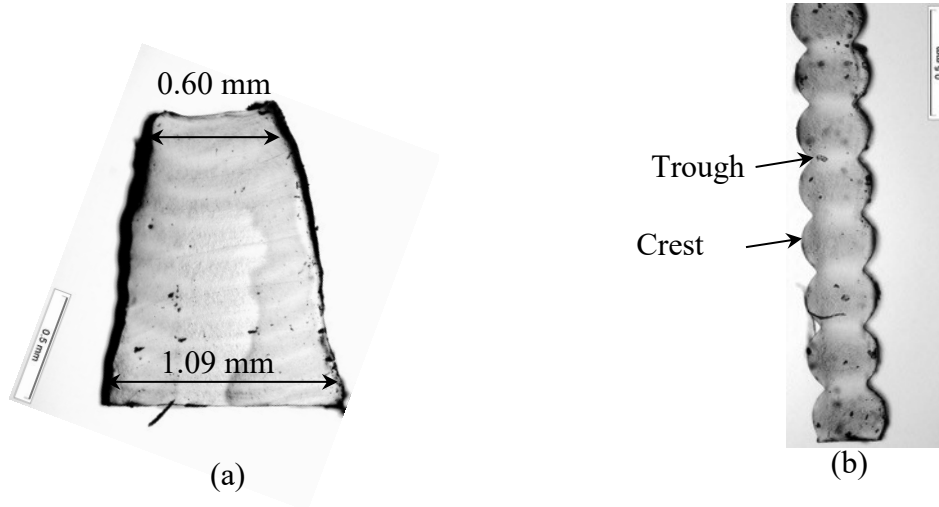


Figure 2.5: Cross-sectional images of (a) $Q = 0.14$ ml/min, $t = 0.14$ mm, and $d_i = 0.84$ mm with large taper (1st layer width = 1.09 mm and 10th layer width = 0.60 mm) and (b) $Q = 0.10$ ml/min, $t = 0.28$ mm, and $d_i = 0.41$ mm with nearly identical layers including no overall taper and layer edges showing large indentations (crest = 0.35 mm wide and trough = 0.22 mm wide).

2.4 Exp. II: Solid

Solid silicone parts, as shown in Figure 2.6, with six adjacent 50 mm long lines, spacing of c , and n_{height} ($=10$) layers in height, were fabricated by AM to study the effect of compression ratio X on internal voids.

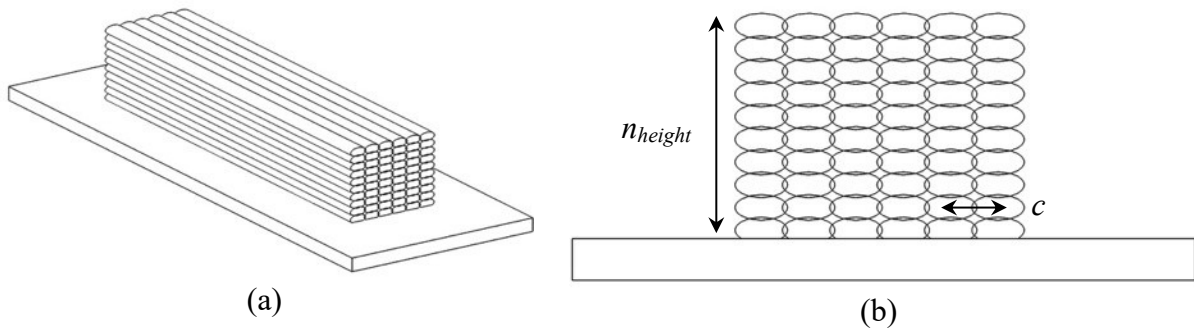


Figure 2.6: A solid silicone AM test part with six 50 mm long adjacent lines and $n_{height} = 10$ to study the compression factor X : (a) configuration and (b) cross-section view.

Using Exp. I process parameters ($Q = 0.12$ ml/min, $t = 0.205$ mm, and $d_i = 0.41$ mm) and setting the compression factor $X = 1$ in Eq. (2.2), the spacing between lines (c) to fill the internal void is 0.489 mm. Two levels of $X = 1.02$ and 1.16, corresponding to $c = 0.48$ mm and 0.42 mm, respectively, were studied (as listed in Table 2.1) to demonstrate a lower/upper limit of X and how it affects the AM part. Two cross-sectional views of the steady-state region on the solid specimens are shown in Figure 2.7. For $X = 1.02$, the overall cross-section (Figure 2.7(a)) is essentially voidless, except small voids are occasionally observed on the top layers (Figure 2.7(b)) due to less compression on these layers. When X is increased to 1.16, a voidless cross-section (Figure 2.7(c)) can be observed in all areas of the cross-section. However, this high compression factor ($X = 1.16$) may create an over extrusion scenario whereby there is too much silicone filling a given volume. This can create silicone buildup at the nozzle which may cause excess deformation of the weakly supported silicone structure leading to dimensional errors and high surface roughness in AM. In summary, a voidless solid silicone AM part can be reliably achieved by adjusting the compression factor. A higher compression factor is needed at the top to while lower layers require a lower compression factor to minimize internal voids.

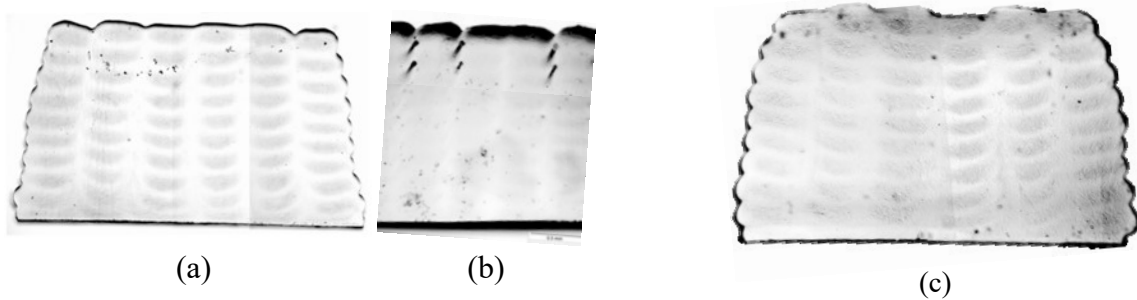


Figure 2.7: Cross-section of the steady-state region of Exp. II Solid with (a) $X = 1.02$ overview, (b) close-up view with small voids in top layers due to less compression, and (c) $X = 1.16$ overview with no void and some over-extrusion.

2.5 Exp. III: Double-Line Wall

A double-line wall with adjacent line spacing of c_{edge} is fabricated to find the cross-section with minimal voids and deformation for thin-wall silicone AM. As shown in Figure 2.8, the length of silicone lines is 50 mm, $n_{height} = 10$, and two levels of c_{edge} (0.42 mm for $X = 1.16$ and 0.48 mm for $X = 1.02$) are investigated.

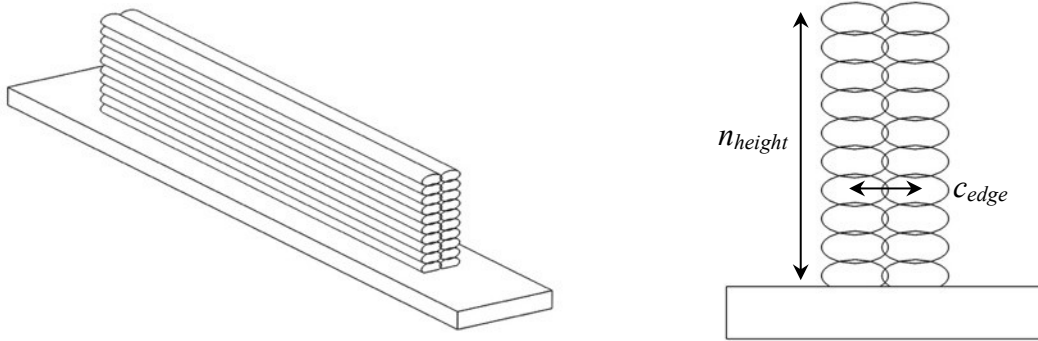


Figure 2.8: Two adjacent silicone lines, 50 mm long, and $n_{height} = 10$ to study the effect of c_{edge} on the thin double-line wall.

Cross-sectional images of two double-line walls fabricated based on the silicone AM process parameters in Exp. I ($Q = 0.12$ ml/min, $t = 0.205$ mm, and $d_i = 0.41$ mm) and Exp. II ($X = 1.02$ and 1.16) are shown in Figure 2.9. With $X = 1.02$, small voids were often observed between layers due to the lack of compression. With $X = 1.16$, voids between layers were eliminated although a high amount of taper is observed in initial layers. This taper is likely due to the rigid build plate restricting the directions in which the silicone can deform. This observation demonstrates that voidless thin-walled silicone AM can be reliably achieved. Varying compression factors could be used throughout to minimize taper and eliminate voids.



Figure 2.9: Cross-section of the double-line wall with (a) $X = 1.02$ and $c_{edge} = 0.48$ mm with voids and (b) $X = 1.16$ and $c_{edge} = 0.42$ mm with no void and taper at the base (initial layers).

2.6 Exp. IV: Bridging

Since the silicone AM material is not self-supporting, a parametric stair-stepping approach for bridging to build a roof which covers open space in extrusion-based silicone AM is studied. The concept for bridging and key process parameters is shown in Figure 2.10. The space between two adjacent lines is c_{edge} for layers around edges for bridging. In this study, six combinations of tests with c_{edge} equals to 0.42 mm ($X = 1.16$) and 0.48 mm ($X = 1.02$), as listed in Table 2.2, were performed. Four new parameters for bridging are illustrated in Figure 2.10 and their values in the six tests are:

- Bridge step-over: This parameter is the overhang distance of the silicone. The bridge step-over is equal to c_{edge} in this study.
- Number of layers before step-over: This parameter is the number of layers to build the base before step-over. In this study, the number is 2 except in Test 2 which only one layer before step over is experimented.
- Number of outlines before infill: This parameter is the number of lines with c_{edge} spacing to build the width of the outline for bridging. In this study, the number was 4 except in Test 6, which only used two outlines before infill was tested.
- Infill overlap with outline: This parameter is defined as the over-extrusion (or overlap) of the infill lines with the outline. The overlap generates a strong bond between the outlines and infill; however, it may also over-extrude the silicone and create dimensional error. Tests 1 to 4 has the infill lines over-travel by 0.06 mm, while Tests 5 and 6 have 0 mm of over-travel.

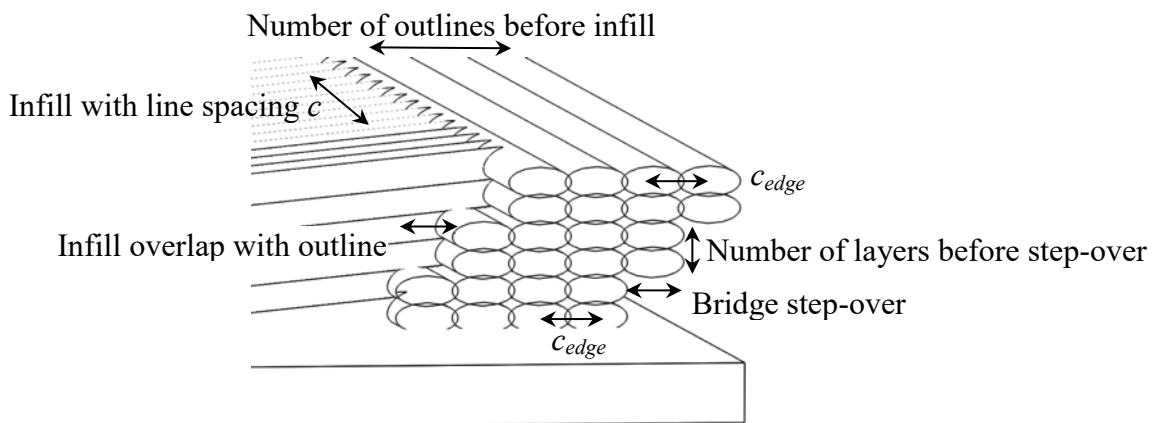

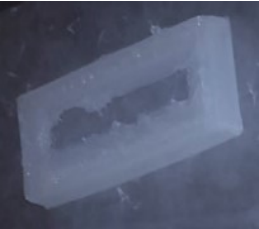
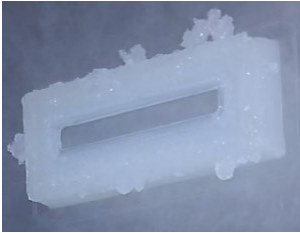





Figure 2.10: Key process parameters for parametric stair-stepping in bridging.

Table 2.2: Process parameters in the bridging parametric study. Test 5 exhibited the best overall results.

Test	c [mm]	c_{edge} [mm]	Bridge step- over [mm]	Number of layers before step over	Number of outlines before infill	Infill overlap with outline [mm]	Shape
1	0.48	0.48	0.48	2	4	0.06	
2	0.42	0.42	0.42	1	4	0.06	
3	0.42	0.42	0.42	2	4	0.06	
4	0.48	0.42	0.42	2	4	0.06	
5	0.48	0.42	0.42	2	4	0	
6	0.48	0.42	0.42	2	2	0	

Process parameters in Tests 1 to 6 are listed in Table 2.2. These process parameters were selected based on the following rationale:

- Test 1: Since the bridging test specimen is similar to the solid section of Exp. II where a low compression factor ($X = 1.02$) achieved a mostly voidless part, this test with $X = 1.02$ was setup as the baseline.
- Test 2: The line spacing c and c_{edge} were reduced and a higher compression factor ($X = 1.16$) was used throughout this test. The number of layers before step-over was reduced to 1 to experiment bridging in as few layers as possible.
- Test 3: The number of layers before step-over was increased to 2 to create redundancy to explore a more robust bridging.
- Test 4: The compression factor for infill (not the outline) was reduced to $X = 1.02$ to reduce the amount of over extrusion.
- Test 5: The same process parameters as Test 4 were utilized except the infill overlap with outline was reduced to 0 to decrease the amount of silicone over extrusion.
- Test 6: The number of outlines before infill was reduced to test the ability of the circumferential outline to mitigate deformation on the bridging edge caused by the infill printing forces.

The shape and dimensions of the workpiece to study bridging is shown in Figure 2.11. Figure 2.11(a) shows a perspective view of the part with an open space in the base and step-over to fill the open space and build a roof. The side view in Figure 2.11(b) illustrates the base, bridge, and roof regions of the Test 5 part with $c = 0.48$ mm, $c_{edge} = 0.42$ mm, and $t = 0.205$ mm. The cross-section A-A (Figure 2.11(c)) shows the dimensions of the base with 10 layers totaling a height of 2.05 mm ($= 10 \times 0.205$ mm) and a four line width of 1.68 mm ($= 4 \times 0.42$ mm). The bridge has sequentially stair-stepped layers and is completed by 19 step-overs, each with 0.41 mm (two 0.205 mm thick layers before step-over) and 0.42 mm ($= c_{edge}$) bridge step-over. Once the bridge is closed, the roof region is created with an additional 5 layers at a height of 1.025 mm ($= 5 \times 0.205$ mm) built above the closed off section. The top view (Figure 2.11(d)) shows the overall size of 50 mm \times 20 mm. The close-up view of the base and bridge regions is shown in Figure 2.11(e).

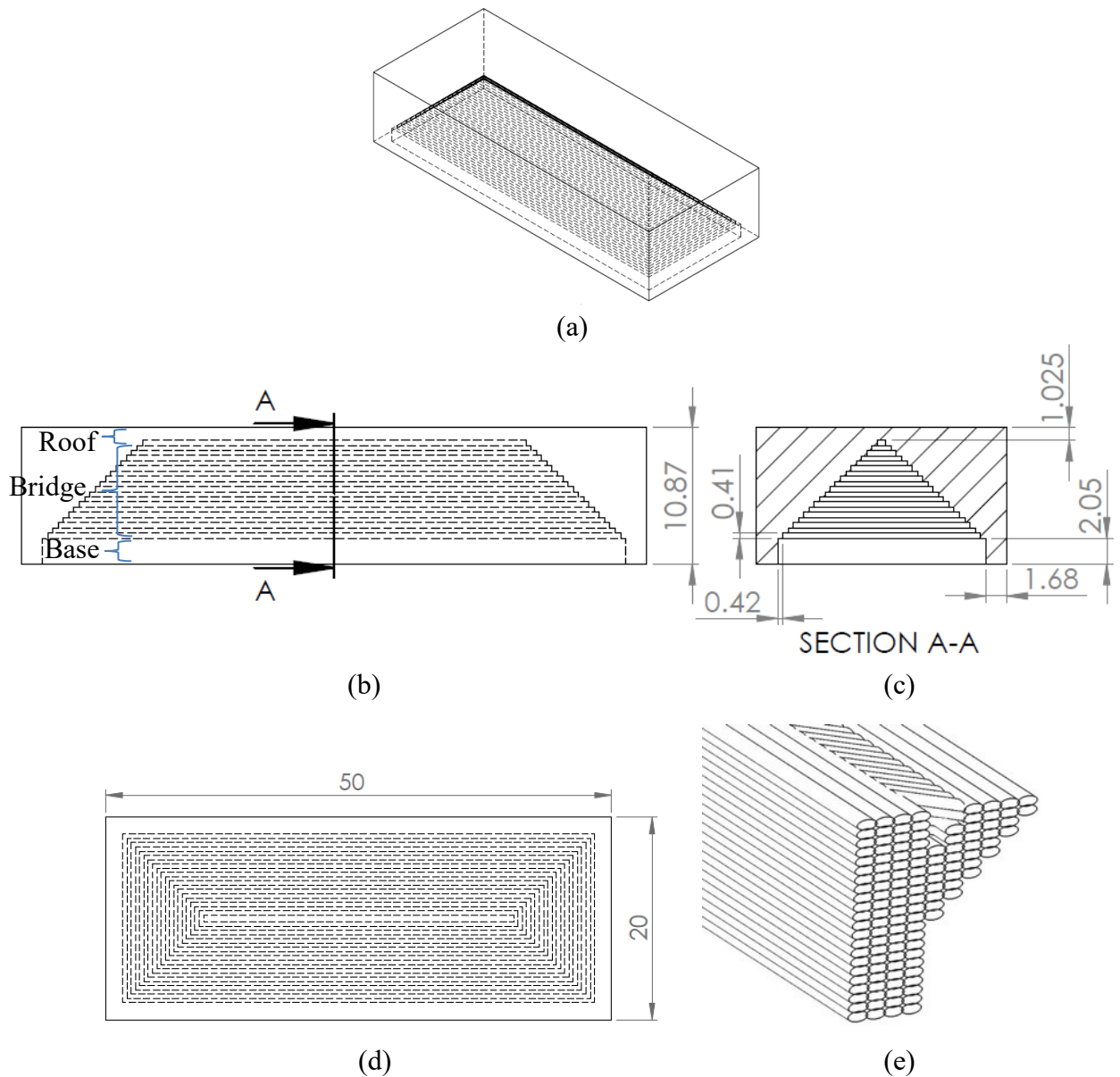


Figure 2.11: Bridging test specimen, with dimensions (unit: mm), for Test 5 part: (a) perspective view, (b) side view, (c) cross-section view of A-A, (d) top view, and (e) close-up view of the base and bridge.

The process parameters used in Test 5 resulted in the best bridging quality among all tests performed. Images of bottom and top views of the specimen in Test 5 are shown in Figure 2.12 and Table 2.2, respectively. By making the bridge step-over distance (0.42 mm, equivalent to $X = 1.16$), there was sufficient compression to adhere the bridging silicone to the outlines. By using a low compression factor ($X = 1.02$) for the infill and a 0 infill overlap with the outline, the over

extrusion of silicone was minimized while maintaining a voidless section. Using two layers before stepping over, each layer was repeated before doing a bridge step-over to minimize the chances of an imperfection ruining the bridging. The 4 outlines before infill separated the infill from the bridging edge, mitigating deformation on the bridging edge caused by the compressive and dragging forces while building the infill. It is noted that process parameters of Test 5 are also applicable to curved geometries for silicone AM of the sphere-like balloon in Exp. V.



Figure 2.12: Bottom view of the bridging in Exp. IV Test 5 specimen.

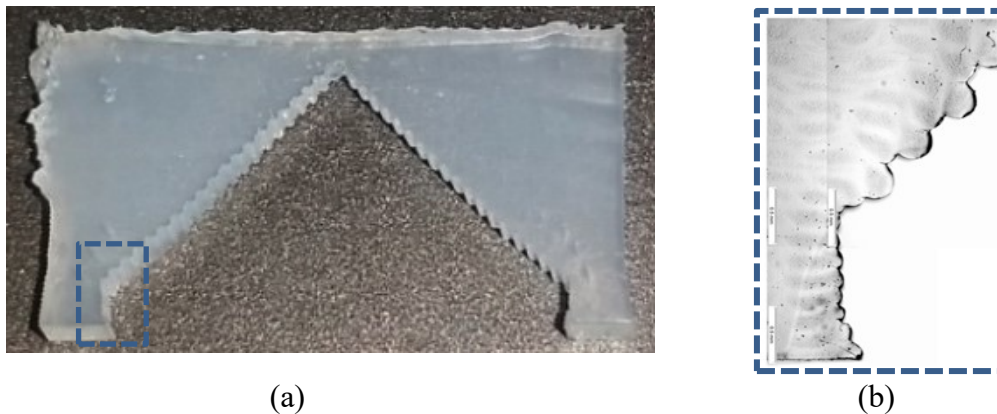


Figure 2.13: Cross-sectional view of the Exp. IV Test 5 specimen: (a) overview and (b) close-up view showing the onset of successful bridging.

The other five tests failed for three reasons: (1) under-extrusion, (2) over-extrusion, and (3) part distortion.

- Under-extrusion, Test 1: As shown in Table 2.2, the bridge step-over line did not have adequate adhesion in Test 1 with $X = 1.02$. While the low compression factor is suitable for

solid sections, it did not provide enough compression to adhere the bridging silicone to the rest of the part.

- Over-extrusion, Tests 2, 3, and 4: Test 2 utilized a larger compression factor, $X = 1.16$, which provided ample compression for the interior bridging edges. However, this test attempted to stair-step over on each layer. While this method should theoretically work, in practice there are imperfections (i.e. over-extrusion) in AM. Without redundancy, any imperfection on the bridging edge accumulates and propagates up to subsequent layers, leading to a failed build, as shown in Table 2.2. In Test 3, very high amounts of over extrusion occurred due to the high compression factor ($X=1.16$) for the entire part leading to failure even with bridging edge redundancy. Test 4 succeeded in bridging but still included excessive over-extrusion (Table 2.2) due to an infill overlap with the perimeter.
- Part distortion, Test 6: As shown in Table 2.2, the only difference between the successful Test 5 and failed Test 6 was the number of outlines before infill. Test 5 had 4 and Test 6 had 2 outlines before infill. Since the infill was printed at a 45° angle with respect to the outline, there was a compression and horizontal dragging force acting on the part by the nozzle and extruding silicone as it was deposited. With 4 outlines (Test 5), there was sufficient buffer between the bridging edge. However, with only two outlines, such forces distorted the dimensional accuracy of the bridging edge and caused the failed bridging.

2.7 Exp. V: Sphere-Like Balloon

To implement the findings from Exps. I – IV, a difficult to manufacture hollow sphere-like balloon was created, Figure 2.14. This balloon is designed to test the inter-layer bonding strength and maximum elongation of a pneumatic actuator made by silicone AM. This hollow sphere-like balloon has three regions: base, double-line wall, and roof. Process parameters in Test 5 for bridging, as summarized in Table 2.1, were applied to fabricate the axisymmetric sphere-like balloon. Dimensions and tool path of the three regions are described as follows:

- Base: As shown in Figure 2.14(b), the base included 4 circumferential outlines (with line spacing $c_{edge} = 0.42$ mm) and 15 layers of height (15×0.205 mm = 3.075 mm). Inside the outline was the solid infill with line spacing $c = 0.48$ mm.
- Double-line wall: As shown in Figure 2.14(c), the double-line wall in Exp. III with $c_{edge} = 0.42$ mm ($X = 1.16$) was applied with the specific bridge step-over to build the curved sphere-like wall. The initial wall thickness is about 0.84 mm. The 12.7 mm cross-section radius of curvature determined the distance of bridge step-over between each layer.
- Bridge and roof: Process parameters from Test 5 in Exp. IV Bridging were used to close off and seal the top of the sphere. A roof with layers height (5×0.205 mm = 1.025 mm) was fabricated after the bridging was completed.

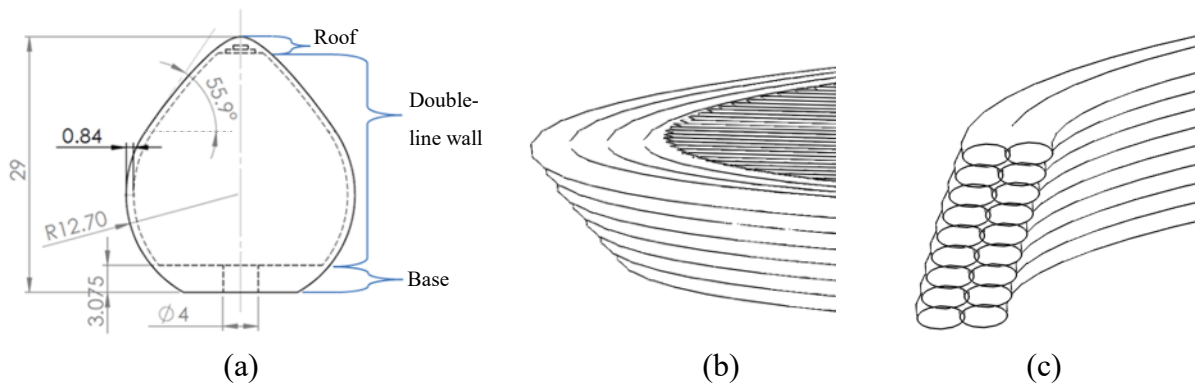


Figure 2.14: Sphere-like silicone balloon: (a) dimensions (unit: mm), (b) base, and (c) curved double-line wall.

After AM, burst testing was performed by slowly increasing the air pressure inside three sphere-like balloons until the burst. These test specimens were cured in a high humidity environment at 65°C for 2 days to ensure the complete cure [37]. A 3.18 mm inner diameter polyvinyl chloride (PVC) hose was attached to a pressure regulator (Performus™ III by Nordson, Westlake, Ohio) set at 34 kPa. A digital pressure gauge with a range of 0 to 344.7 kPa and a full-scale accuracy of $\pm 1.0\%$ (Model DPGA Series of Dwyer Instruments) was attached in-line with the PVC hose to measure the pressure inside the silicone balloon. A digital camcorder was used to continuously monitor the pressure and dimensions of the balloon during inflation. The ImageJ 1.50i software (National Institutes of Health, USA) was used to measure the diameter of the balloon using pixel-distance correlation during inflation. Figure 2.15 shows an example of the silicone balloon burst tests. The original shape of the sphere-like balloon, about 25.9 mm in diameter, is shown in Figure 2.15(a). This balloon was inflated and burst at about 10.6 kPa (1.54 psi), as shown in Figure 2.15(b), with a diameter of 76.1 mm.

The wall stress σ (assuming uniform distribution) in a sphere under pressure P is equal to $Pr/(2h)$, where r is the radius of the balloon and h is the thickness [38]. The initial balloon wall thickness was about 0.84 mm (the double-line wall thickness). Assuming the conservation of volume and perfect spherical geometry, the thickness of the wall h before rupture is estimated based on the diameter at rupture, from that, σ can be calculated.

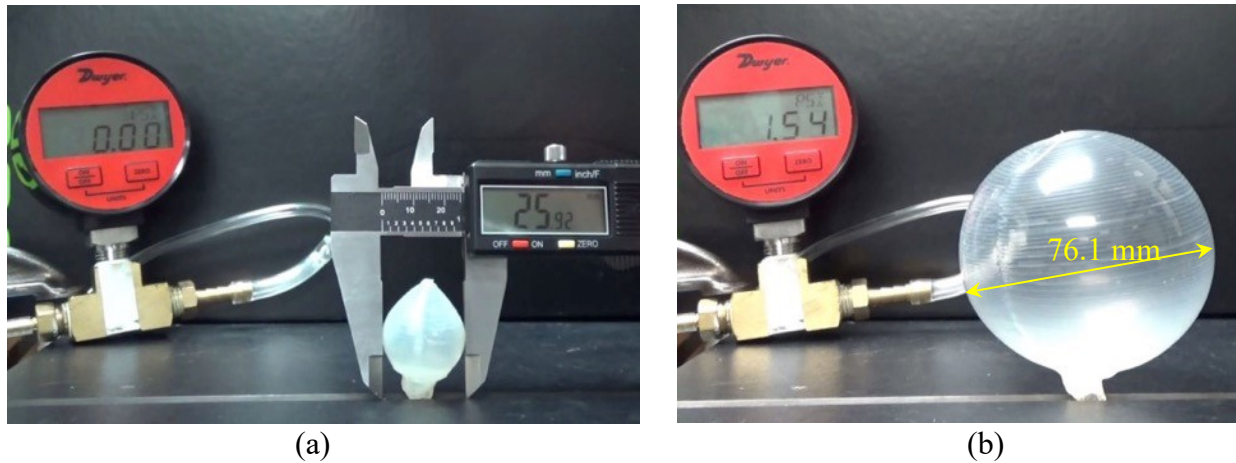


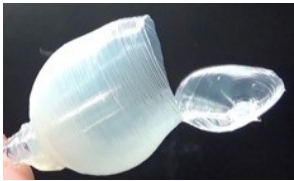


Figure 2.15: Burst pressure test of sphere-like balloon: (a) the 25.9 mm initial diameter measured with a caliper and (b) the inflated close-to-rupture balloon with the diameter measured using the pixel-distance correlation of the image.

Three sphere-like silicone balloons were built by AM for burst experiment. Table 2.3 shows the results. Balloons had burst pressures ranging between 10.6 and 11.7 kPa, a diametrical expansion between 152 and 207%, and burst stress between 1.46 and 2.55 MPa. According to the datasheet for the silicone used in this study [36], the tensile strength of the silicone material is expected to be greater than 1.2 MPa. Our experiment shows the value of silicone fabricated by AM is comparable to this value.

In all three tests, failure initiated near the top of the balloon parallel to the printed layer. This is likely due to a stress concentration caused by (1) the oblong balloon geometry without support structure and (2) the void in the thin-walled silicone structure during AM. As the thin structure grows in height, it becomes increasingly less stable under extrusion forces during AM. This lack of stability could lead to geometric errors causing variations in c_{edge} which may result in void formation. The thin structure also may not provide adequate opposing compressive force to minimize void formation during extrusion-based AM. For weakly supported thin-wall structures at elevated height, an additional compression factor or a faster curing material may be required to eliminate voids which can lead to stress concentration and rupture under tension.

Table 2.3: Burst testing results from three sphere-like balloons.

	Balloon 1	Balloon 2	Balloon 3
			
Initial diameter (mm)	26.09	25.9	26.08
Diameter at burst (mm)	65.9	79.6	76.1
Initial thin-wall thickness (mm)	0.84	0.84	0.84
Final thin-wall thickness (mm)	0.13	0.09	0.10
% change in diameter, Lagrangian strain	152.4	207.3	191.7
Rupture pressure (kPa)	11.7	11.4	10.6
Stress at burst (MPa)	1.46	2.55	2.05

2.8 Exp. VI: Finger Pneumatic Actuator

The finger pneumatic actuators, commonly referred to as pneu-nets [39], were fabricated to test fatigue life of the silicone AM parts. As shown in Figure 2.16, the actuator is approximately $110 \text{ mm} \times 18 \text{ mm} \times 15 \text{ mm}$ with 12 chambers. Under positive internal air pressure, this finger actuator curls and creates a bending motion. Figure 2.16(a) shows the perspective view and the XYZ coordinate system of the pneumatic finger actuator (layers are built up in the Z direction). Dimensions in the top view (XY plane) and side view (XZ plane) of the finger actuator are shown in Figure 2.16(b). Two cross-sections, marked as B-B and C-C are shown in Figure 2.16(c) and (d). These cross sections illustrate four regions of this pneumatic actuator: base, double-line wall, four-line wall, and bridge and roof. Dimensions and tool path of three regions are described as follows:

- Base: As marked in Figure 2.16(c) and (d), the base included 4 circumferential outlines (with line spacing $c_{edge} = 0.42$ mm) and 9 layers of height (9×0.205 mm = 1.845 mm). Inside the outline was the solid infill with line spacing $c = 0.48$ mm.
- Double-line and four-line wall: The double-line wall in Exp. III with $c_{edge} = 0.42$ mm ($X = 1.16$) was applied to create vertical sections either 0.84 mm or 1.68 mm thick.
- Bridge and roof: Process parameters from Test 5 in Exp. IV Bridging were used to close off and seal the top of the finger pneumatic actuator and to create a 5-layer (1.025 mm thick) roof.

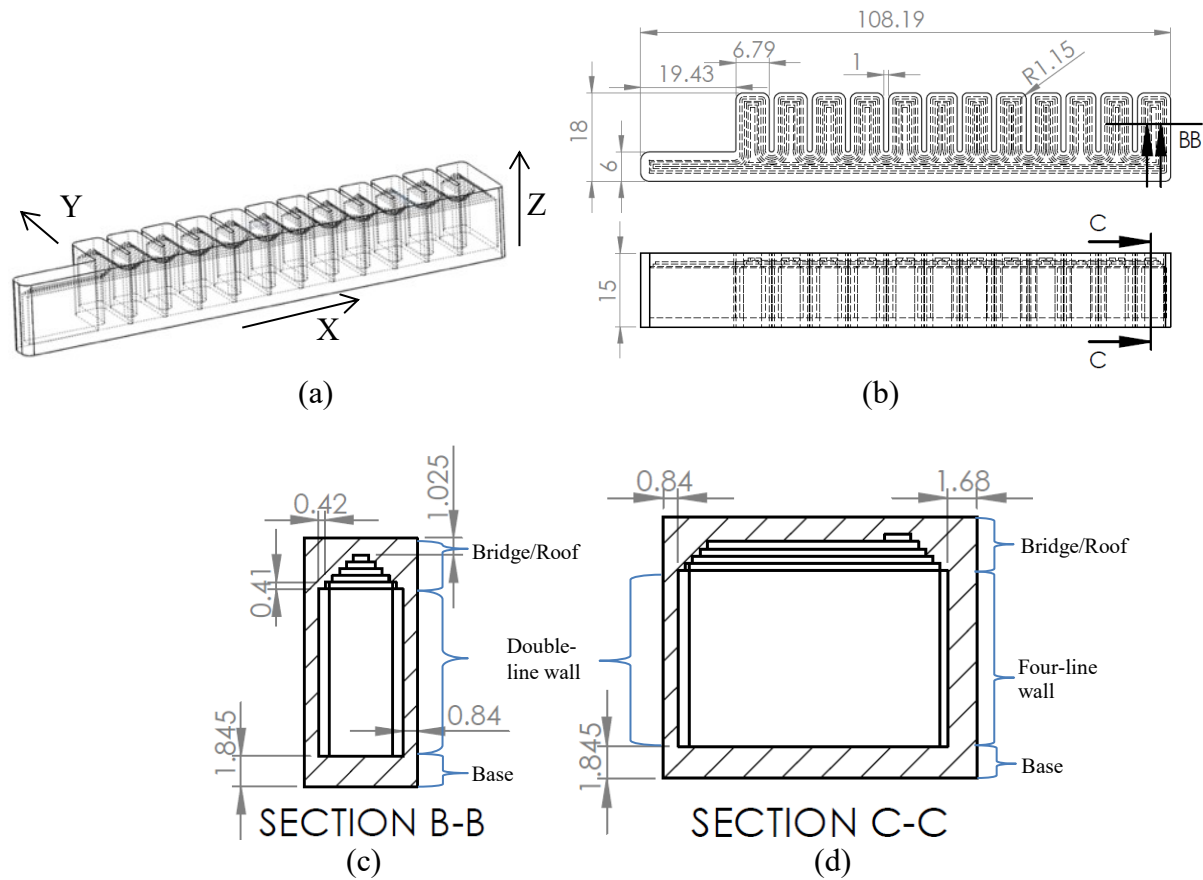
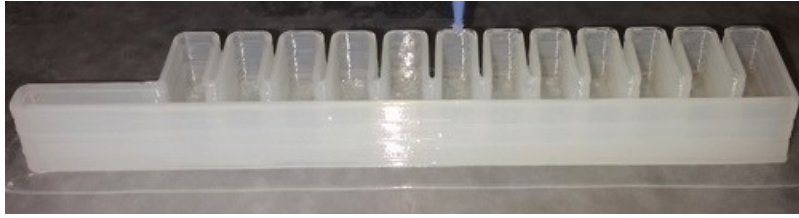


Figure 2.16: Finger pneumatic actuator test specimen, with dimensions (unit: mm), for fatigue testing: (a) perspective view and XYZ coordinate system, (b) side views, (c) cross-section view of B-B, (d) cross-section view of C-C.

The extrusion-based AM of silicone finger pneumatic actuator thin-wall and bridging roof is illustrated in Figure 2.17.



(a)



(b)



(c)

Figure 2.17: Silicone AM of the finger pneumatic actuator: (a) thin-wall vertical structure and (b) and (c) using the bridging technique in Test 5 of Exp. IV to close the horizontal gap with an air tight seal.

Like in Exp. V, specimens were cured in a high humidity environment at 65°C for 2 days. A 3.175 mm ID PVC tube was embedded into the end of the finger actuator and attached to a pressure regulator (Performus™ III by Nordson, Westlake, Ohio). Air was injected into the finger actuator at 70 kPa in the stress-free state (Figure 2.18(a)) until full circular articulation with inside radius of about 13 mm was reached (Figure 2.18(b)). An infra-red (IR) sensor (Model pna4602m by Panasonic) was used to detect when full articulation occurred and triggered a relay to release the air pressure to atmosphere for 1 s, allowing the finger actuator to return to its original state. Every time the IR sensor was triggered, a counter was incremented so that the number of full cycles before failure could be recorded. This fatigue test was repeated on

three figure pneumatic actuators fabricated by AM to evaluate the number of cycles before the failure occurs.

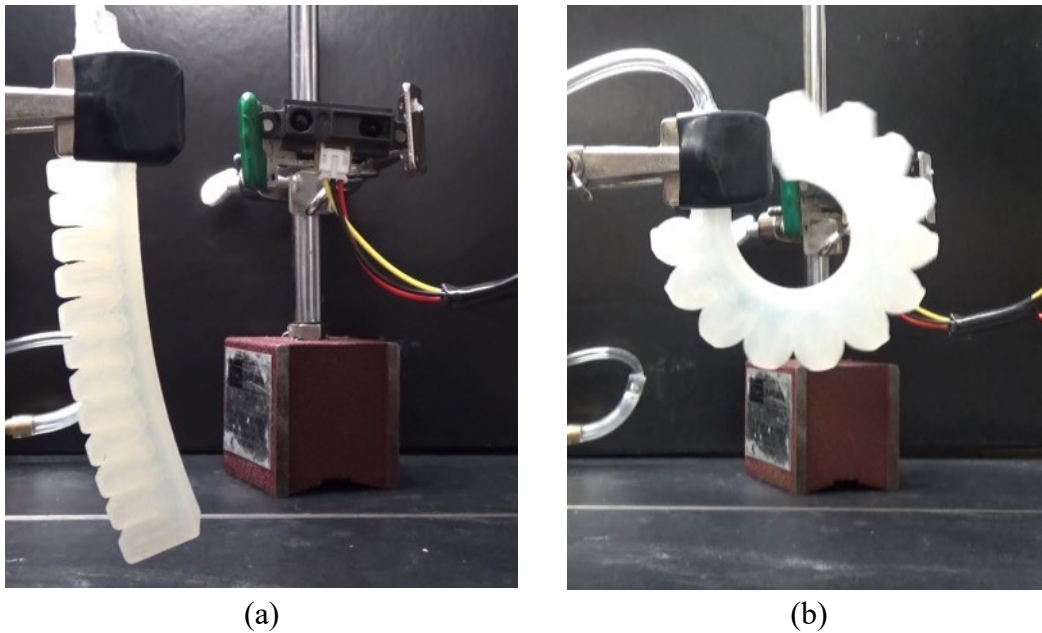


Figure 2.18: Finger pneumatic actuator in a (a) non-articulated and (b) fully articulated configurations.

Three finger actuators all lasted for >30,000 cycles. Figure 2.19 shows the close-up view of the failure location and the number of cycles to failure. The tearing initiated at these points due to imperfections likely caused by the buildup of excess silicone which distorts the dimensional accuracy of the layers leading to less than optimal adjacent line spacing and void filling. In particular, Test 1 likely failed earlier than the rest of the specimens due to an over extrusion buildup on the nozzle tip that dislodged at the high stress corner of one of the chambers.

the part during the AM process to minimize distortion in thin-walled sections along with modeling the start/stop dynamics of the silicone flow in the nozzle to further minimize void creation and over-extrusion.

CHAPTER 3
VOIDS AND TENSILE PROPERTIES IN EXTRUSION-BASED ADDITIVE
MANUFACTURING OF MOISTURE-CURED SILICONE ELASTOMER

Nomenclature:

c	Distance between two adjacent silicone lines
c_{edge}	Distance between two adjacent silicone lines at edge
d_i	Inner diameter (ID) of nozzle tip
Q	Volumetric flow rate
t	Layer height
v	Nozzle speed in the layer

3.1 Introduction

Additive manufacturing (AM) can fabricate a wide range of soft, flexible custom parts for applications in soft robotics, wearables, assistive and rehabilitation devices, seals, actuators, cushioning, energy absorption, and others. As summarized in Table 3.1, five major AM processes, the selective laser sintering [5], photopolymer jetting [6,7], stereolithography based on digital light projection [8–11], extrusion-based fused deposition modeling of thermoplastic elastomers (TPE) [12,13], and direct extrusion of silicone [15,16] have been studied for AM of soft parts.

Each soft material in AM comes with certain limitations (Table 3.1). For example, most of the current commercially available soft materials for AM [5–7,9–11] have low elongation at break (110-270%). The thermoplastic polyurethane [12,13] with higher elongation at break (660%) is limited by high hardness (85 Shore A). The elastomer created by blending commercially available materials [8] can achieve a high elongation at break (1100%) but is still limited by high hardness (65 Shore A). This elastomer material blend can also be adjusted to

lower the hardness, but the elongation at break quickly deteriorates. Additionally the operating temperatures of the above materials are typically between -20°C – 60°C .

Conversely, many silicone elastomers, denoted as silicone hereafter, are readily available and suitable for direct extrusion-based AM (the main requirement being that the material does not self-level or wet-out before curing). This can reduce the cost and barrier to entry while enabling a wide range of material properties such as high elongation at break, high tensile strength, extreme use temperatures, high fatigue life, and hardness ranging from 3-90 Shore A and beyond [14–16]. Unfortunately there are many challenges to overcome in direct extrusion of silicone for AM of soft 3D parts. One of particular importance is understanding how voids generated during the AM process impact the tensile strength and strain.

In the direct extrusion AM process, uncured silicone is extruded through a moving nozzle line-by-line, building up multiple layers to fabricate a 3D part [15,16]. When two silicone lines are in contact with each other, the inter-layer cross-linking occurs and chemically bonds adjacent lines together. Because of this, the inter-layer bonding strength in AM of silicone can be close to the original silicone material. However, it can be difficult to completely fill the 3D geometry without internal voids (or internal gaps within the part) which can lead to the stress concentration under loading.

Voids are inevitable in extrusion-based AM of silicone. They are also a key factor impacting the strength and durability of silicone parts fabricated by AM. There are two regions for void generation in extrusion-based AM: “between layers” and “within layers”. For between layers, Plott et al. [16] studied the effects of compression in extrusion-based AM of silicone to avoid or reduce the void formation. The cross-sectional view of the vertical stack of extruded silicone lines showed that the so called “voidless” AM of silicone was feasible. Compression of silicone during extrusion-based layer deposition also caused the deformation which affected the part mesostructure [16]. The other source of void generation, within the layer, is caused by geometrical situations (e.g. the sharp corner) where a given line width cannot fill 100% of the area within a layer. Tensile testing of dumbbell (or dog-bone) shaped specimens is a standard way of quantifying the effects of AM process parameters on void formation and tensile strength and strain.

Table 3.1: Summary of soft materials for AM. Some values for Shore A hardness, denoted with *, were approximated from the elastic modulus using Gent’s correlation [3,4].

AM Process	Material	Tensile Strength [MPa]	Elongation at Break [%]	Shore A Hardness	Maximum Use Temperature [°C]	Remarks
Selective Laser Sintering	DuraForm Flex [5]	1.8	110	45 – 75	-	Low elongation
Photopolymer Jetting	TangoBlackPlus [6]	0.8 – 1.5	170 – 220	26 – 28	-	Low elongation
	Agilus30 [7]	2.4 – 3.1	220 – 270	30 – 35	-	Low elongation
Stereolithography: Digital light projection	SUV Elastomer [8]	0.9	500	34*	-	Properties depend on formulation. Tensile strength and elongation at break reduce with hardness.
		7.5	1100	65*	-	
	Spot-E resin (Spot-A Materials) [9,10]	2.26 ± 0.71	65 – 140	65	-	Low elongation High hardness ~9 cycle fatigue life
	Carbon Elastomeric Polyurethane 40 [11]	6 ± 1	190 ± 10	68	-	Low elongation High hardness
Extrusion-based: Fused deposition Modeling	NinjaFlex Thermoplastic Polyurethane [12,13]	4	660	85	60	Yield at 65% strain High hardness
Extrusion-based: Direct (this study)	Silicone [14–16]	5 – 11	100 – 1100	3 – 90	-110 – 300	Available in many grades (e.g. food, medical, etc.).
	Dow Corning 737 Silicone (this study)	1.2 – 1.8	600 – 710	33	-65 – 177	>100,000 cycle fatigue life [16]

A plurality of tensile test studies have been performed for extrusion-based fused deposition modeling (FDM) of acrylonitrile butadiene styrene (ABS) material [30–35]. These studies showed that the build direction, material flowrate, distance between adjacent lines, layer orientation, and layer thickness all affect the strength of the FDM parts. Another study utilized computed tomography (CT) to reveal that voids of various sizes exist inside a FDM part [40]. It

is evident that parts produced by FDM had a lower tensile strength than an injection molded part of the same shape and material due to the void formation and other factors [34].

In this study, the ASTM D412 Type C dumbbell tensile specimen [41] is selected as the standard shape for extrusion-based silicone AM to fabricate the tensile specimen and investigate the void formation and its effect on tensile strength and strain. Corresponding to prior tensile test studies of ABS produced through FDM, a variety of AM tool paths and process parameters were used to fabricate these specimens with voids of varying dimensions and locations. Tensile specimens of the same dumbbell shape were also stamped out of a solid sheet of the cured silicone material and evaluated as the baseline results for comparison. Prior to the tensile tests, optical examination was used to quantify voids, or internal gaps, within the specimens to determine the effects of void geometry and orientation on tensile strength and strain. After the tensile tests, the broken surfaces were imaged for failure mode analysis. Breaking these specimens in tension allows for the quantification of tensile strength and strain, observation of the fracture surface, and correlation of voids and AM process parameters on the failure mode and tensile test results.

The silicone material, extrusion-based AM methods, and tensile test setup are introduced in the next section. The pre-tensile test inspection of voids, tensile strength results, and failure analysis are then presented.

3.2 Silicone Material and Experimental Setup

This section outlines the silicone material, the equipment and tool path used for AM of tensile test specimens, and the testing apparatus.

3.2.1 Silicone Material and Cure Parameters

A commercially available one-part oxime cure silicone elastomer (Dow Corning® 737, Dow Corning, Midland, Michigan, USA) was used as the base material for all tensile specimens in this study. Based on the datasheet, this silicone has 33 Shore A durometer hardness, over 1.2 MPa tensile strength, and over 300% elongation. The material has a zero shear rate viscosity of

about 62.5 Pa·s and begins curing under exposure to atmospheric moisture. Once exposed to this moisture, it has a skin-over time of 3 to 6 minutes, a tack-free time of 14 minutes, and a cure to handling time of 24 hours at 25°C and 50% relative humidity [15,36].

3.2.2 AM Machine and Setup

The experimental setup for extrusion-based AM of tensile specimens is shown in Figure 3.1. The system consists of four key components: (1) a motion control platform based on an open-source FDM machine (LulzBot TAZ5 by Aleph Objects, Loveland, Colorado, USA), (2) a progressive cavity pump and its controller (Model preeflow eco-PEN 450 pump and Model EC200 controller by Viscotec, Töging am Inn, Germany) to dispense the silicone with a dosing accuracy of $\pm 1\%$ [29], (3) syringe barrels (Model Optimum by Nordson EFD, Westlake, Ohio, USA) pressurized to 70 ± 10 kPa which feed the progressive cavity pump with silicone material while preventing the introduction of air bubbles into the silicone, and (4) a tapered nozzle with 22 gauge (0.41 mm inner diameter) tip (Model SmoothFlow™ by Nordson EFD, Westlake, Ohio, USA) to deposit the silicone on the build plate.

Temperature during AM was between 21 to 23°C with humidity between 10 to 30% to ensure the cure rate was not artificially increased. Each part consisted of 12 layers and took about 38 minutes to complete, equating to a layer time of about 3 minutes. Since the layer time was on the low end of the silicone skin-over time, 3 to 6 minutes [36], the potential for reduced interlayer bonding strength caused by printing on top of a cured silicone layer is minimized.

The silicone was extruded through the nozzle directly onto a glass build plate which was coated in a thin layer of mold release (Ease Release® 205, Smooth-On, Pennsylvania, USA) before each print. Specimens were then cured in place, on the glass build plate, at ambient conditions (19°C ambient temperature and 10 to 30% relative humidity) for 24 hours before handling. Specimens were then removed from the glass plate and post-cured in an oven at approximately 38°C and 15 to 40% relative humidity for at least 24 hours to ensure complete cure [37].

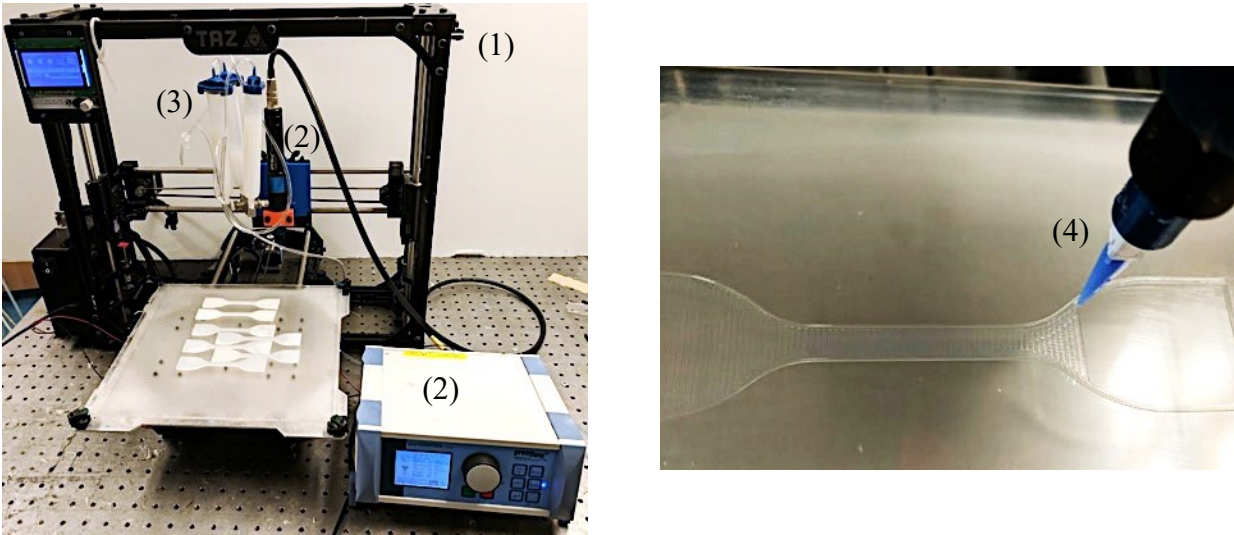


Figure 3.1: Experimental setup for extrusion-based silicone AM including: (1) motion control platform, (2) progressive cavity pump and controller, (3) pressurized syringe barrels, and (4) tapered nozzle.

3.2.3 Tensile Test Specimen Fabrication

Tensile test specimens were produced using both an extrusion-based AM process along with a sheet casting and stamping process to compare the tensile strength results between the AM and traditional molding/casting techniques.

Extrusion-Based AM Specimens: To produce the extrusion-based AM silicone tensile specimens, a 3D model of the tensile test specimen, based on the ASTM D412 Type C Dumbbell Specimen with a thickness of 2.4 mm [41], was first created using SolidWorks 2016 (Dassault Systemes SOLIDWORKS Corp). This 3D model was then exported as a stereolithography file (STL) and a G-code based tool path was generated with specific printing process parameters using Simplify3D[®] (Blue Ash, Ohio). This G-code file was then sent to the 3D-printer for AM of the dumbbell specimen.

The process parameters for tool path generation were adopted from the extrusion-based AM of moisture-cured silicone elastomers with minimal internal voids [16], as shown in Figure 3.2. Accordingly, to test the effects of internal voids on tensile strength, process parameters were selected with the goal of achieving minimal, small, or large voids between adjacent

extruded lines. One of the process parameter to control the void size is the spacing between infill lines (c). According to Eq. (3.1) [16], assuming the incompressible condition of the silicone and given the volumetric flow rate (Q), layer height (t), and nozzle speed (v), the compression factor (X) can be adjusted to calculate the spacing between infill lines (c) necessary to achieve minimal voids ($X \geq 1$), small voids ($X < 1$), or large voids ($X \ll 1$), within the part mesostructure.

$$Xc = \frac{Q}{tv} \quad (3.1)$$

Parameters Q , t , and v were selected based on suitable “voidless” process parameters [16].

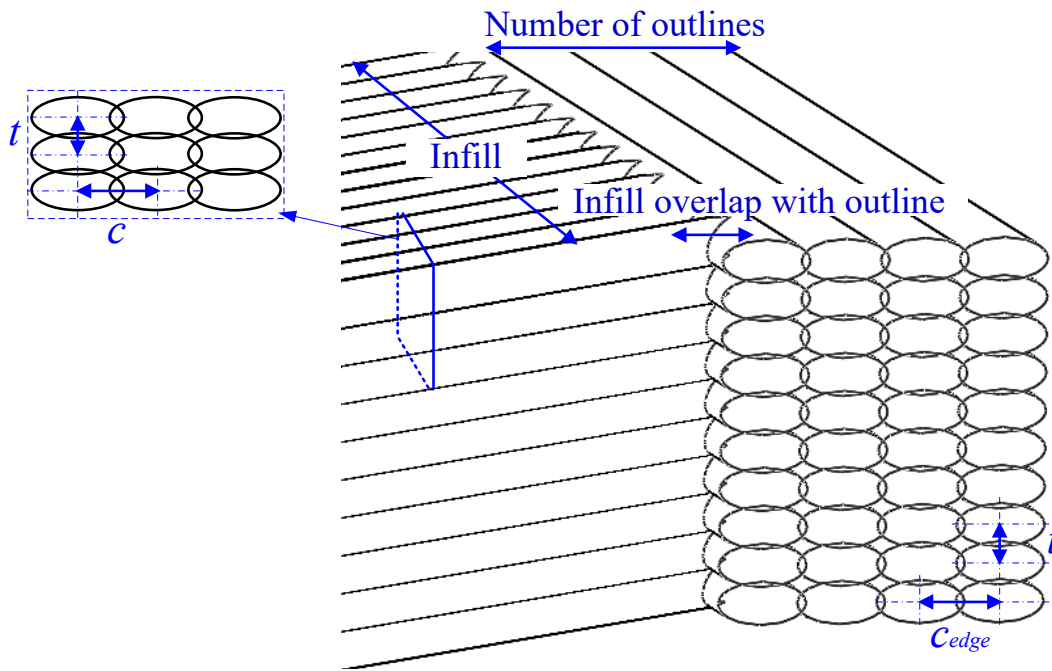


Figure 3.2: Sample cross-section including concentric outlines (right side) and infill (left side) along with key process parameters for extrusion-based silicone AM.

In this study, six silicone AM process parameters remain as constant: (1) the flow rate $Q = 0.12$ ml/min, (2) the layer height $t = 0.2$ mm, (3) the nozzle diameter $d_i = 0.41$ mm, (4) the nozzle speed $v = 20$ mm/s, (5) the distance between two adjacent lines at the outline edge $c_{edge} = 0.43$ mm, and (6) infill overlap with outline = 15%. Other factors can affect void size and dimensional accuracy including but not limited to the initial extrusion height from the build

plate, the incident angle between the infill and the part outline, the dynamics of the machine used to actuate the nozzle for material deposition, and the flow properties of the extruded material. All these parameters remain as constant in this study.

Three key AM process parameters varied in this study are: compression factor X , number of outlines, and infill angle for AM. Values of these and corresponding parameters used to produce the tensile specimens are listed in Table 3.2.

Table 3.2: Key process parameters used to adjust the void size within the part mesostructure.

Compression factor	c [mm]	Number of outlines	Infill angle	Number of specimens
$X = 1.00$	0.50	2	90°	7
		2	$\pm 45^\circ$	7
		6	0° -O	3
		0	0° -NO	3
$X = 0.97$	0.52	2	90°	7
		2	$\pm 45^\circ$	7
		6	0° -O	3
		0	0° -NO	3
$X = 0.91$	0.55	2	90°	5
		2	$\pm 45^\circ$	5
		6	0° -O	3
		0	0° -NO	3

- Compression factor X : Three levels of X at 1.00, 0.97, and 0.91 (corresponding to the spacing between infill lines c of 0.50, 0.52, and 0.55 mm, respectively) to achieve the minimal voids, small voids, and large voids, respectively, within the AM tensile specimen mesostructure are studied.
- Number of outlines: For each X , as shown in Table 3.2, the number of outlines around the tensile test specimens is 0, 2, or 6. Example tool paths of tensile test specimens with 0, 2, or 6 outlines are illustrated in Figure 3.3.
- Infill Angle: As shown in Figure 3.3, three infill angles of 90° , $\pm 45^\circ$ (alternating layers of $+45^\circ$ and -45°), and 0° relative to the long axis of the dumbbell tensile specimen are investigated. In Table 3.2, for 90° and $\pm 45^\circ$ infill angle, the number of outlines is 2. For 0° infill angle, the number of outline is either 6 or 0, which are denoted as 0° -O (with outline) and 0° -NO (no outline), respectively.

The number of specimens was chosen to achieve a representative sample size and corresponds to the variation of the tensile test strength. As shown in Table 3.2, for samples with 90° and ±45° infill angle, the number of tensile sample evaluated is higher, either 5 or 7. For 0°-O and 0°-NO samples, the number of tensile sample studied is 3.

For specimens with 0° infill with respect to the long axis of the specimen, as shown in Figure 3.3, two tool paths were created in an attempt to minimize tangency voids in the narrow section of the dumbbell specimen and maintain a smooth edge profile. The specimen 0°-O has six concentric outlines and 0°-NO specimen has no outlines.

Baseline Sheet Stamped Tensile Specimens: For baseline tensile strength comparison, seven tensile test specimens were stamped out of a sheet of the cured silicone (same material as in AM specimens) using a die cutter to create the tensile specimens with the similar shape and thickness as those fabricated by extrusion-based AM. Since the silicone used in the study cures in the presence of atmospheric moisture, these specimens could not be molded.

The stamped tensile specimens were produced by Dow Performance Silicones (Midland, Michigan) using the following procedure: (1) A 75 µm thick Mylar sheet, 300 by 600 mm in size, was taped onto a flat bench top; (2) A 1.9 mm thick stainless steel shim stock was taped onto each long edge of the Mylar sheet; (3) Silicone was carefully dispensed onto the Mylar sheet without air entrapment; (4) A rectangular stainless steel bar was placed on the shim stocks and steadily drawn toward the uncovered end to form a uniform thickness silicone sheet on the Mylar sheet; (5) The silicone sheet was left at room temperature to cure for at least 48 hours with 19°C ambient temperature and 3% relative humidity; (6) A dumbbell shaped die was used to stamp out specimens for testing with the help of a hand operated press; and (7) Specimens were then post-cured in an oven at approximately 38°C and 15 to 40% humidity for at least 24 hours to ensure complete cure.

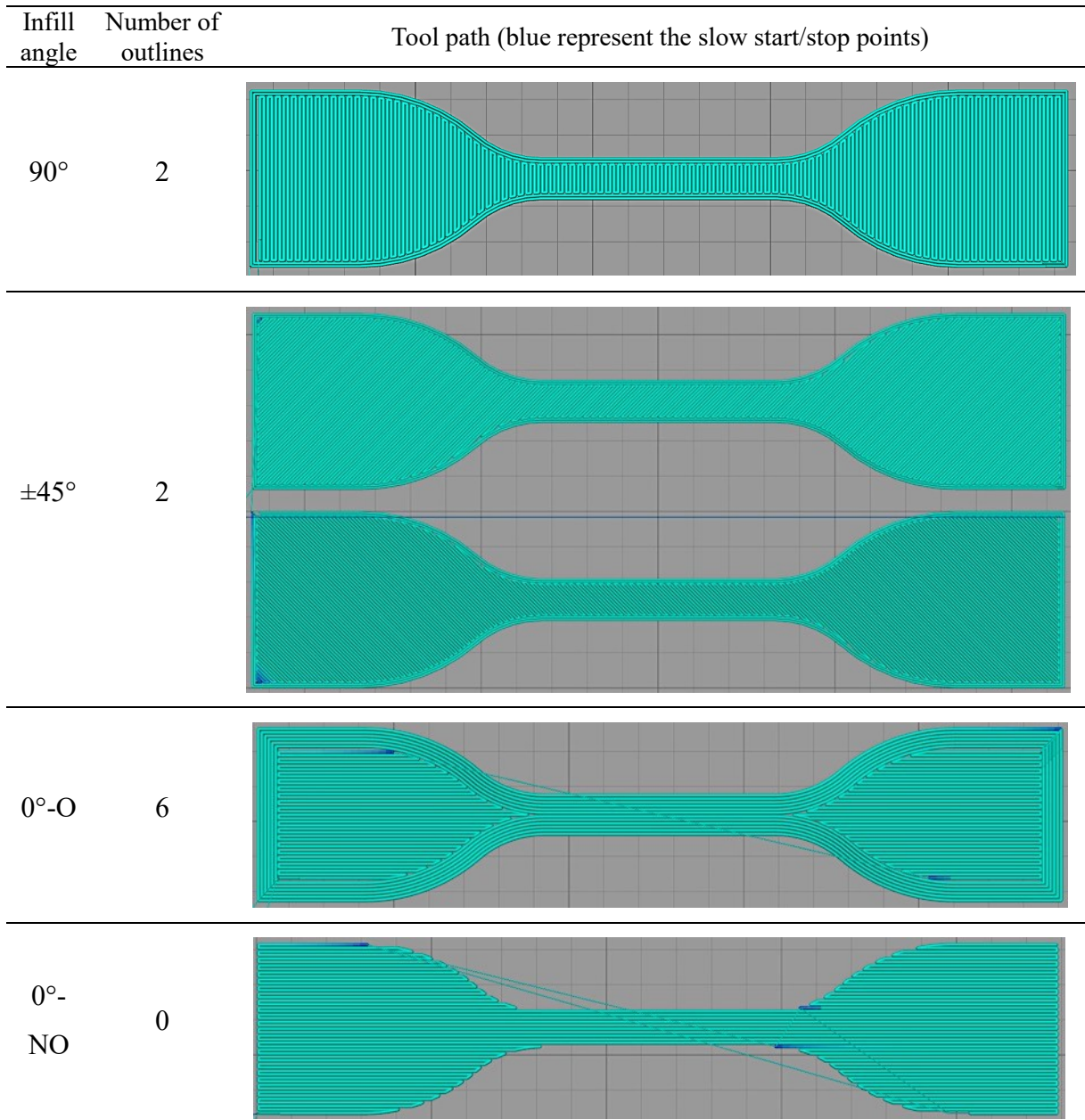


Figure 3.3: Tool paths for tensile test specimens with a variety of infill angles and outlines, capturing the common solid geometries found in extrusion-based AM of silicone. Infill orientation is with respect to the long axis of the specimen.

3.2.4 Tensile Testing Machine and Test Parameters

The tensile tests were performed using an MTS Insight™ electromechanical tensile test machine with 10 kN load cell (MTS Systems Corporation, Eden Prairie, Minnesota) at a rate of 500 mm/min, in accordance with ASTM D412 [41]. Testing was performed at ambient

conditions (21 to 23°C with humidity between 10 to 30%). As shown in Figure 3.4, specimens were also marked with ink and filmed during elongation to measure strain.

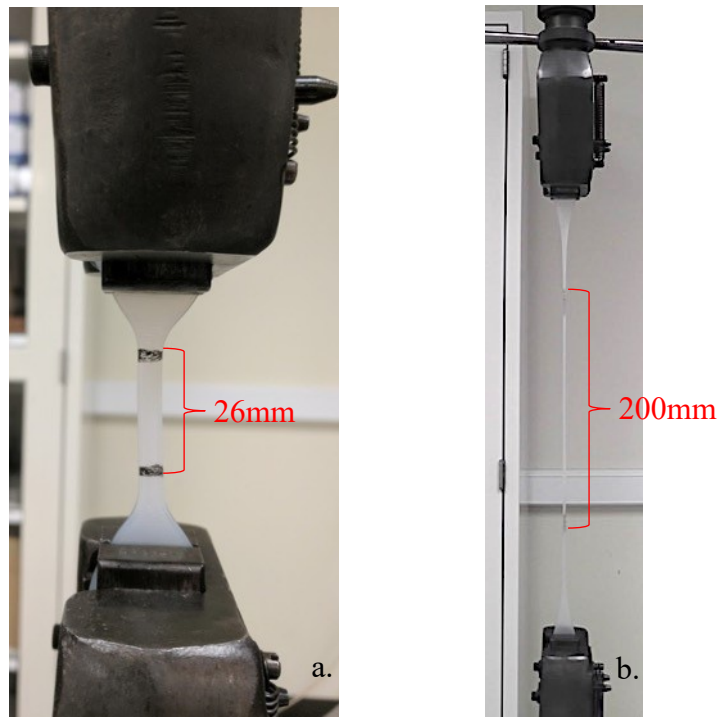


Figure 3.4: Tensile test machine with the silicone tensile specimen and ink markings for strain measurement under the (a) no strain and (b) 670% engineering strain conditions.

3.3 Voids in Tensile Specimens

Prior to performing the tensile tests, each specimen was imaged using an optical microscope with 10 megapixel digital camera (Amscope, Irvine, California, USA) to quantify voids created by the manufacturing process. The 0° AM tensile specimens were also sectioned to inspect for voids in the cross-section using another optical microscope with 5x optical zoom.

3.3.1 Baseline Sheet Stamped

No internal voids were observed in the baseline stamped specimens. The surface finish, as shown in Figure 3.5, was the best out of all the specimens. Minor imperfections exist due to the nature of the fabrication procedure but no specific voids could be observed.



Figure 3.5: Stamped baseline specimen from a cast sheet of material. Spots are from dust particles.

3.3.2 AM Specimens with $X = 1.00$

The optical microscopy images of 90° , $\pm 45^\circ$, 0° -O, and 0° -NO AM tensile specimens with $X = 1.00$ are shown in Figure 3.6(a)-(e). In the layer, the 90° , $\pm 45^\circ$, and 0° -NO specimens showed no internal voids from the AM process. For the 0° -O specimens, as shown in Figure 3.6(c), an internal void at the tangency where the infill met the outlines at a nearly parallel angle was observed due to the contact angle between the infill and the part outline.

Figure 3.6(a) and (b) show that the top surface of the specimens with 90° and $\pm 45^\circ$ infills contained mild irregularities due to over-extrusion of silicone within the given volume, possibly from an imperfect starting layer height, overlap of the two outlines on the part edge, infill overlap with the outlines, and/or material overlap at infill corners due to machine response time. Figure 3.6(c) and (d) show that the 0° -O and 0° -NO specimens had a very smooth top surface finish. The 0° -NO specimens also contain several nearly 90° corners (Figure 3.6(d)) which may cause stress concentrations and lead to premature part failure.

Figure 3.6(e) shows the cross-section of the 0° -NO specimen with $X = 1.00$. No voids were observed.

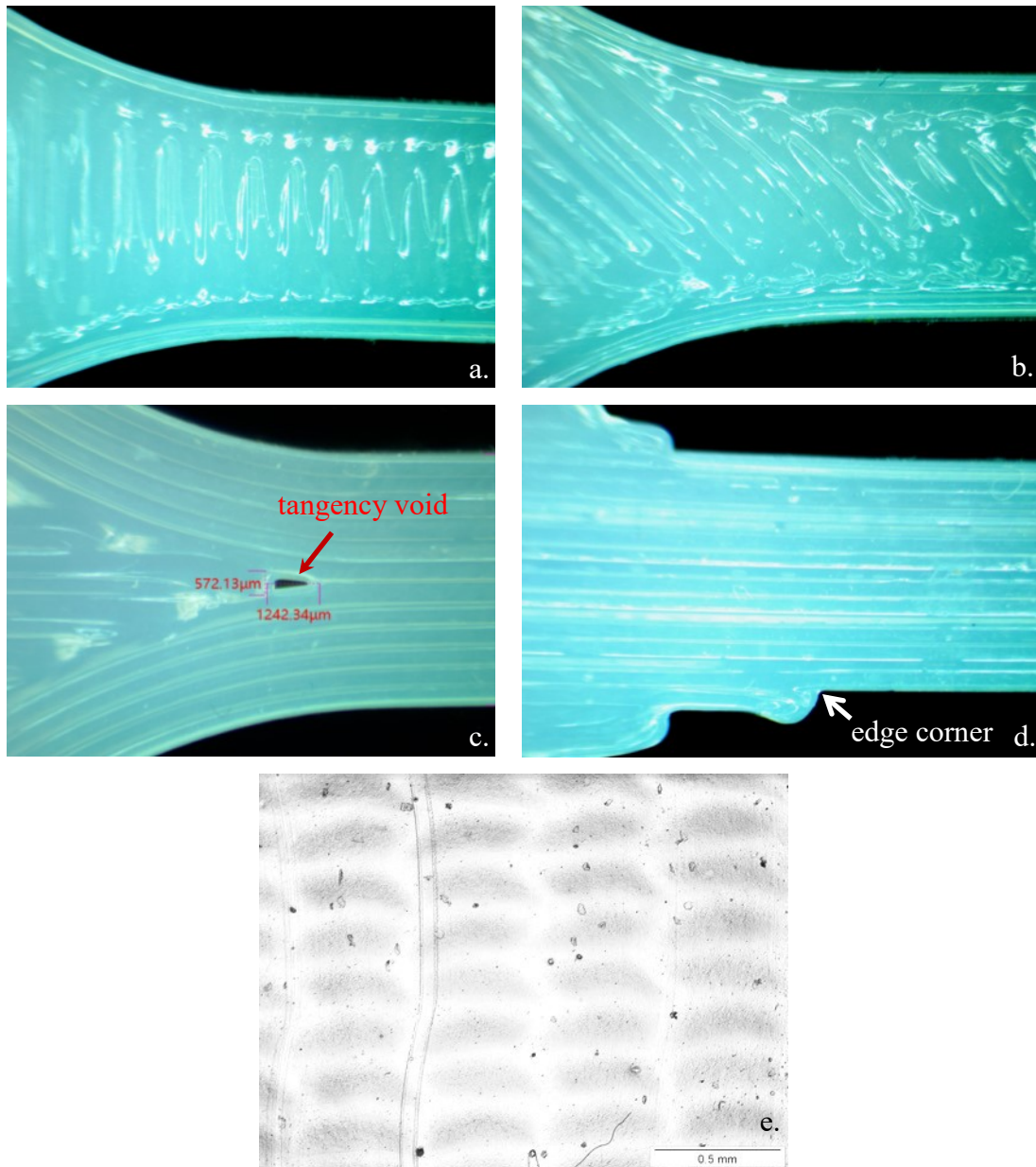


Figure 3.6: Detailed top-view of AM Specimens with $X = 1$ (a) 90° , (b) $\pm 45^\circ$, (c) 0° -O, and (d) 0° -NO along with (e) cross sectional view of 0° -NO.

3.3.3 AM Specimens with $X = 0.97$

Four AM tensile specimens with $X = 0.97$ are shown in Figure 3.7. Small internal voids from the AM process are observed at some, but not all, infill corners of the 90° and $\pm 45^\circ$ specimens, as shown in Figure 3.7(a) and (b), respectively. These voids were small (300 to 500 μm in diameter) and circular in shape. Small voids (about 90 μm diameter) also appear

internally along the long axis for 0° -O and 0° -NO specimens, Figure 3.7(e). Larger voids, due to the sharp tangency infill angle, for the 0° -O case were observed, Figure 3.7(c). The 0° -NO specimens again have corner edges.

The top surface (not shown) of the specimens with 90° and $\pm 45^\circ$ infills contained less irregularities than the AM specimens produced with $X = 1$ since the smaller compression factor is less likely to lead to an over extrusion condition. The 0° -O and 0° -NO specimens again had a very smooth top surface finish.

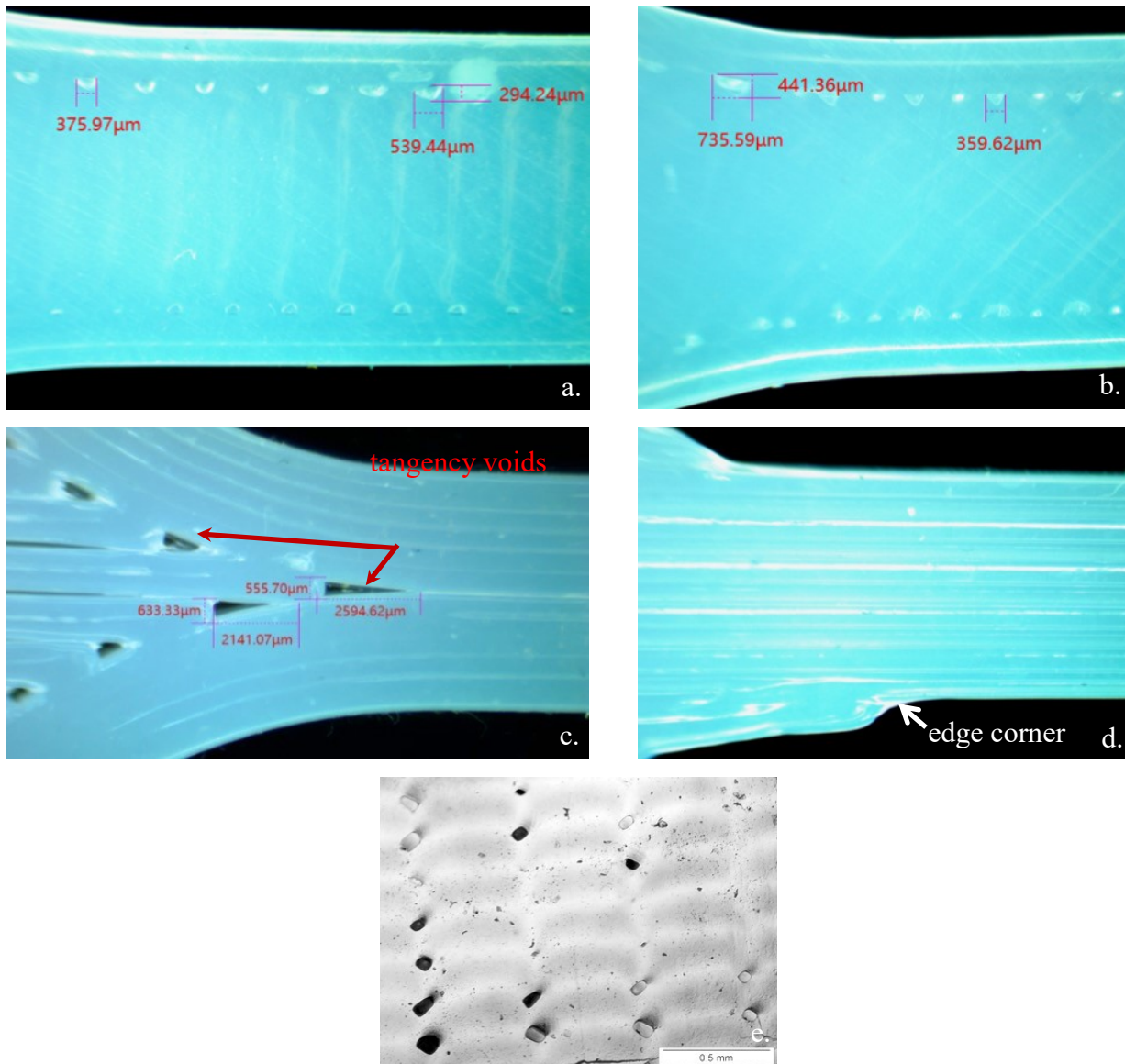


Figure 3.7: Detailed bottom-view of AM Specimens with $X = 0.97$ (a) 90° , (b) $\pm 45^\circ$, (c) 0° -O, and (d) 0° -NO along with (e) cross sectional view of 0° -NO. The bottom surface is shown to more easily quantify void size.

3.3.4 AM Specimens with $X = 0.91$

Four specimens produced with a compression factor $X = 0.91$ showed distinct internal voids from the AM process, Figure 3.8. Most notably, the internal voids for the 90° and $\pm 45^\circ$ specimens changed into elongated features that span at least half the width of the specimen, as shown in Figure 3.8(a) and (b). The 0° -O specimen had the greatest tangency voids, Figure 3.8(c). The 0° -NO specimens again contain corner edges, Figure 3.8(d). The gap between adjacent lines in 0° -O and 0° -NO specimens extended nearly the entire vertical length of the specimen, Figure 3.8(e).

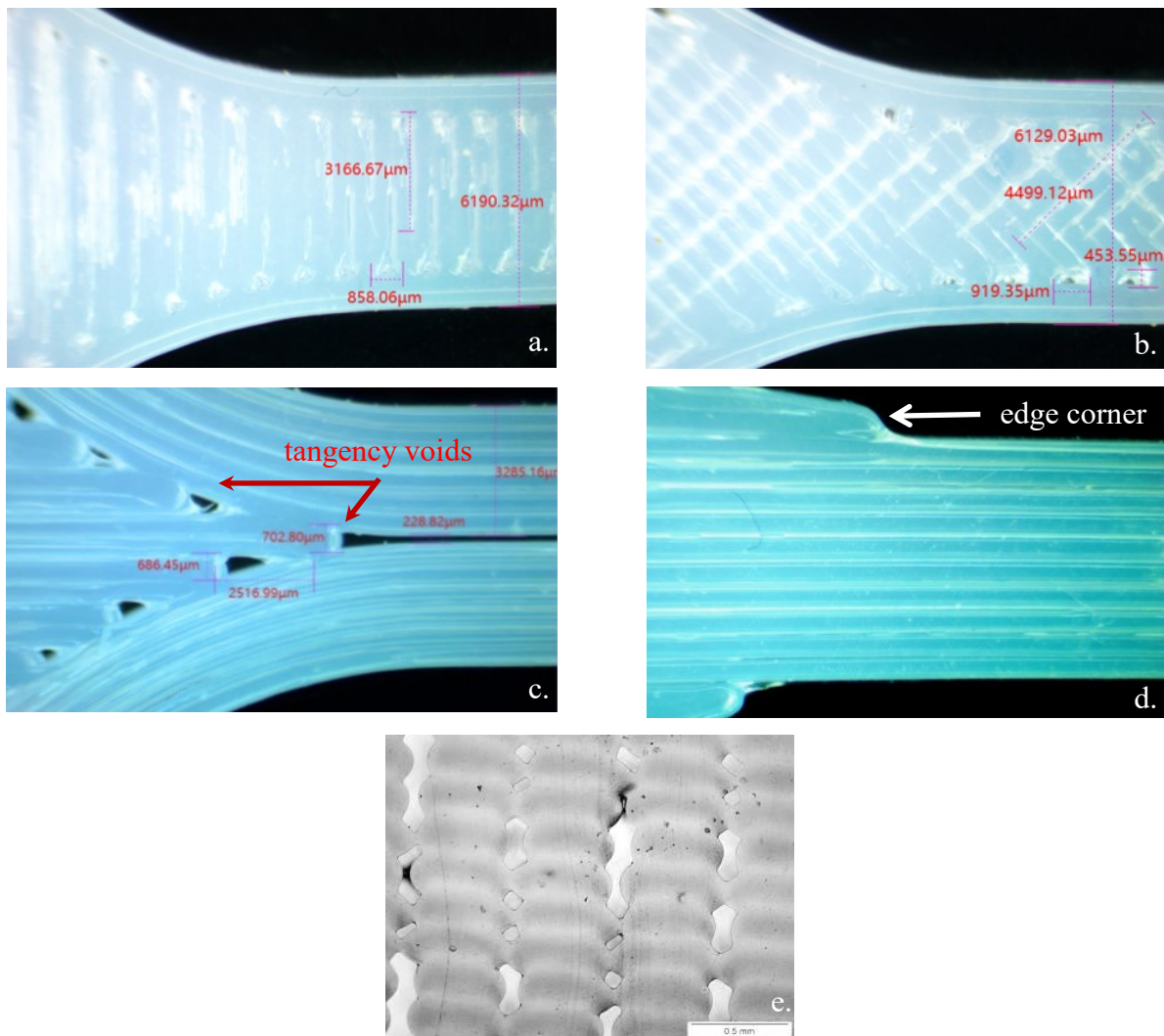


Figure 3.8: Detailed bottom-view of AM Specimens with $X = 0.91$ (a) 90° , (b) $\pm 45^\circ$, (c) 0° -O, and (d) 0° -NO along with (e) cross sectional view of 0° -NO. The bottom surface is shown to more easily quantify void size.

3.4 Tensile Testing Results

Tensile strengths for 13 specimens (stamped and 4 configurations for $X = 1.00, 0.97,$ and 0.91) are summarized in Figure 3.9. Each configuration has between 3 and 7 tensile tests to correlate the tensile strength to AM process parameters. In total, 61 tensile specimens were tested and the maximum tensile strength values are listed in Table 3.3.

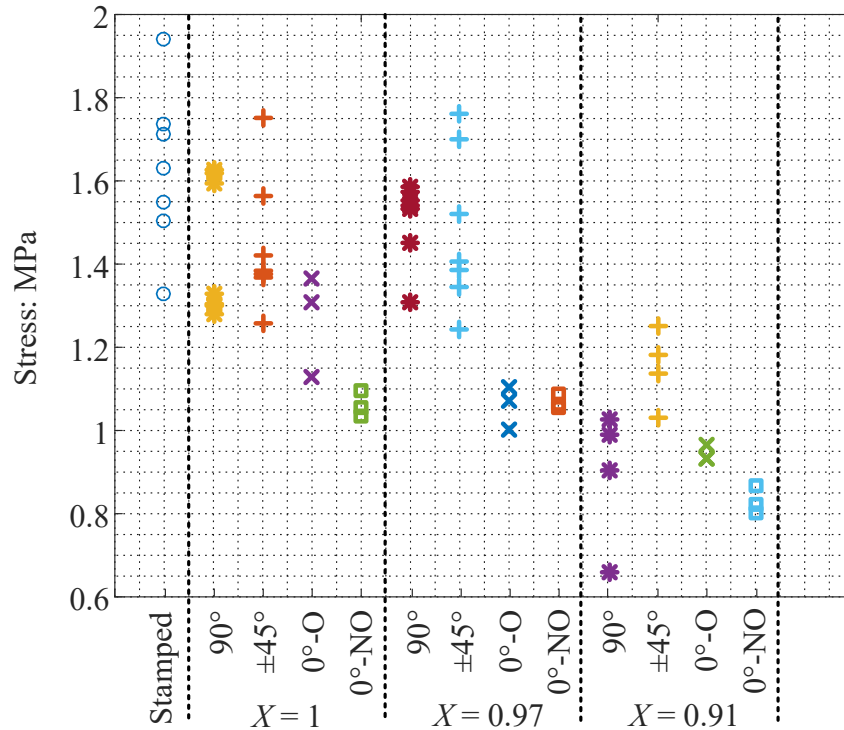


Figure 3.9: The maximum tensile strength of each specimen. The stronger specimens (stamped, 90° and ±45°, $X = 1$ and 0.97) all show a large range of strengths while the weaker specimens tend to show less strength variability. A drop-off in maximum strength was observed in all $X = 0.91$ specimens.

The strongest specimens were the sheet stamped dumbbells with an average tensile strength of 1.63 MPa. The next strongest configurations were the 90° and ±45° specimens with $X = 1.00$ and $X = 0.97$. The average tensile strengths of these specimens ranged from 1.44 to 1.51 MPa and were nearly indistinguishable from one another. The 0°-O and 0°-NO specimens were consistently the worst performing.

To verify that the strain of the AM specimens was within the expected value for the silicone material (over 300% [36]), strain was measured optically on 90° and ±45° AM specimens with $X = 1.00$. The strain of these specimens ranged from 600% to 710%, with an average strain of 650%, showing that the strain of the AM specimens lies within the expected strain range of the material.

Table 3.3: Maximum tensile strength results (in MPa) corresponding to those plotted in Figure 3.9.

Sheet Stamped (baseline)	AM Specimens, $X = 1$				AM Specimens, $X = 0.97$				AM Specimens, $X = 0.91$			
	90°	±45°	0°-O	0°-NO	90°	±45°	0°-O	0°-NO	90°	±45°	0°-O	0°-NO
1.51	1.33	1.76	1.31	1.10	1.55	1.52	1.10	1.06	0.91	1.14	0.93	0.80
1.33	1.62	1.37	1.13	1.05	1.54	1.34	1.07	1.05	0.99	1.25	0.96	0.82
1.94	1.63	1.38	1.37	1.04	1.45	1.41	1.00	1.09	1.03	1.18	0.93	0.87
1.55	1.59	1.39			1.58	1.39			0.66	1.03		
1.74	1.30	1.56			1.59	1.76						
1.63	1.28	1.42			1.53	1.70						
1.71	1.30	1.26			1.31	1.24						
Avg. 1.63	1.44	1.45	1.27	1.06	1.51	1.48	1.06	1.07	0.90	1.15	0.94	0.83

3.5 Failure Analysis

To determine the cause of specimen failures, two sets of observations were conducted. First, the tensile specimens were visually monitored during the tensile pull tests so void deformation under high elongations could be observed. Second, after failure, an optical microscope was used to image the fracture surfaces of the strongest and weakest specimens in each category, allowing for the identification of failure initiation point(s) and crack propagation.

3.5.1 Deformation of Voids

Figure 3.10 shows pictures of void deformation for AM specimens under tension with 90° and ±45° infill orientations (Figure 3.10(a) and (b) with $X = 0.97$ and Figure 3.10(c) and (d)

with $X = 0.91$, respectively) along with a 0° -O and 0° -NO specimen (Figure 3.10(e) and (f) with $X = 0.97$, respectively). In Figure 3.10(a) and (b), under large elongations, the original small and circular voids (300-500 μm in diameter) grew in length but were largely oriented along the direction of force. For the $X = 0.91$, Figure 3.10(c) and (d) show the voids were of sufficient length that they could not fully orient themselves along the direction of force, causing internal stress concentrations to occur. The tangency voids in the 0° -O specimen (Figure 3.10(e)) and the edge corners in the 0° -NO specimen (Figure 3.10(f)) also led to stress concentrations.

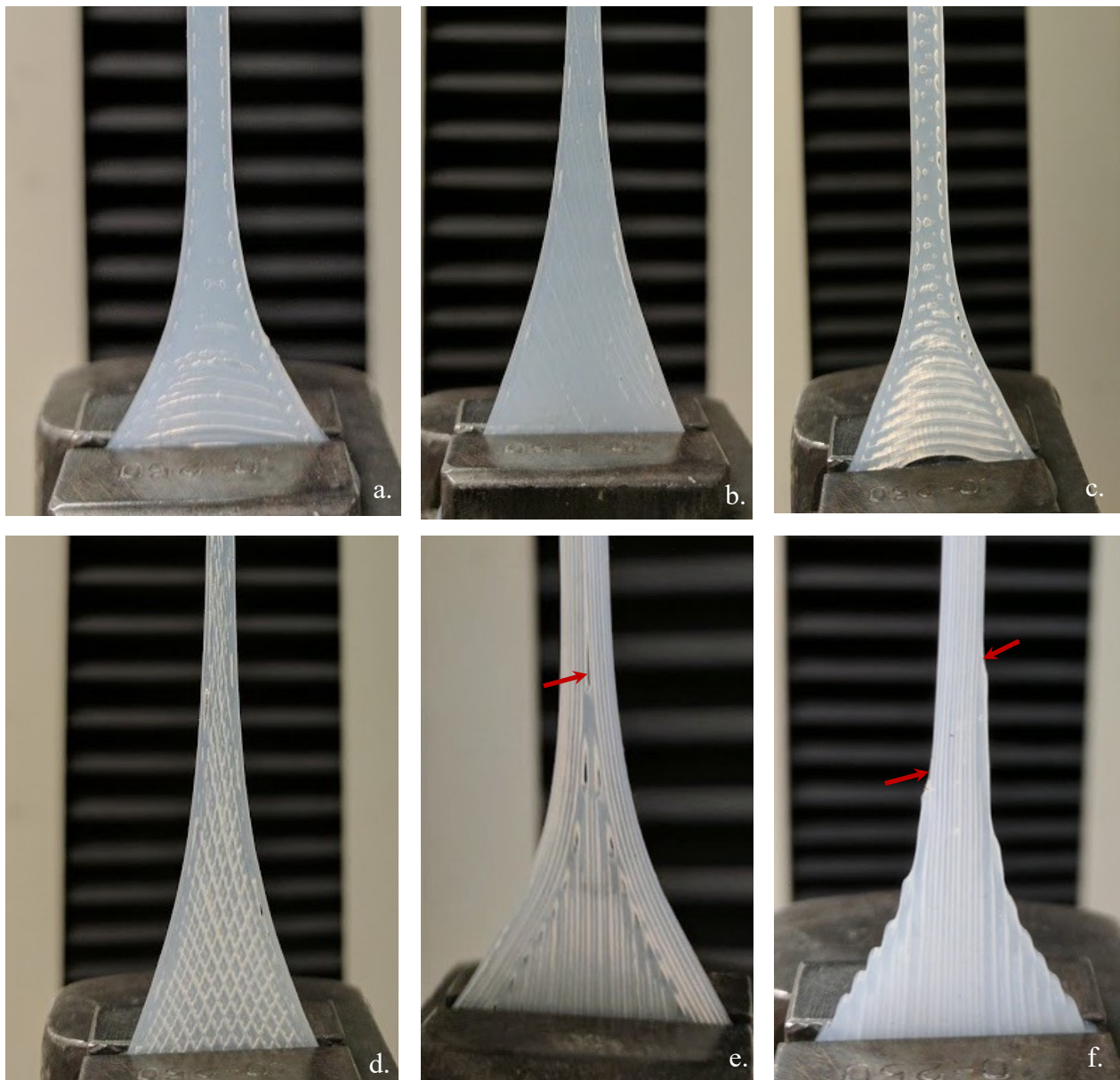


Figure 3.10: Voids in tensile test specimens under tension: (a) 90° ($X = 0.97$), (b) $\pm 45^\circ$ ($X = 0.97$), (c) 90° ($X = 0.91$), (d) $\pm 45^\circ$ ($X = 0.91$), (e) 0° -O ($X = 0.97$), and (f) 0° -NO ($X = 0.97$).

Figure 3.11 shows a close-up top surface view of the 0°-O and 0°-NO specimens after failure. For the 0°-O specimen, the failure mechanism is due to stress concentration at the tangency void in the narrow to thick transition of the specimen. For 0°-NO specimens, the stress concentration at the corner initiated the failure.

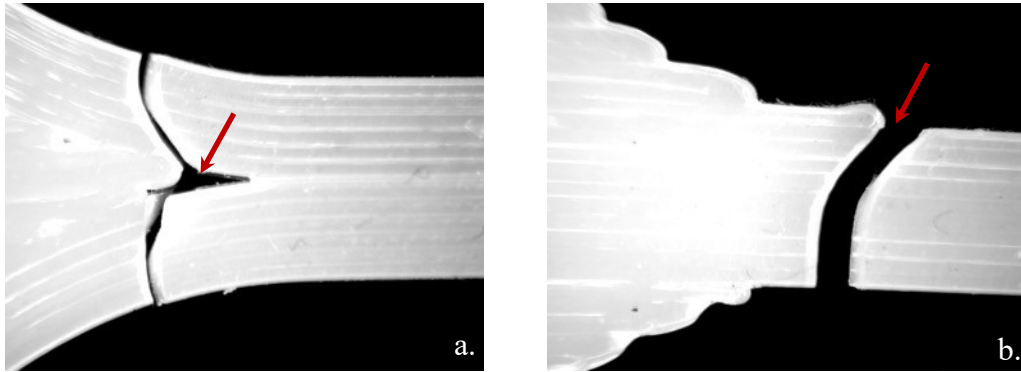


Figure 3.11: Failure surface of the (a) 0°-O and (b) 0°-NO specimens. All specimens of this infill type failed in a similar manner regardless of void size.

3.5.2 Fracture Surface Analysis

Optical microscopy images under 5x zoom were taken of the failure cross-sections for strongest and weakest stamped, 90°, and ±45° specimens. About 6 to 8 images were patched together to visualize the whole cross-sectional failure surface.

Stamped: Figure 3.12 shows failure surface cross sectional images of the strongest (1.94 MPa) and weakest (1.33 MPa) sheet stamped tensile specimens. The strongest specimen failure initiated within the part, likely due to a small inclusion in the material. The weakest specimen failure initiation began near the right edge of the part. As shown in the top views of the specimen fracture surfaces, the break was perpendicular to the direction of force with the exception of the small grey region around two failure points.

X = 1.00: Four failure surfaces of the strongest 90° (1.63 MPa), weakest 90° (1.28 MPa), strongest ±45° (1.76 MPa), and weakest ±45° (1.26 MPa) AM tensile specimens with $X = 1.00$ are shown in Figure 3.12. The strongest specimens both failed in similar locations on the bottom surface of the specimen. This was a surprising failure location since the bottom surface was

originally connected to the build plate and therefore has a very flat/smooth surface finish. One potential reason for this failure location is due to the oxime cure system of the silicone. For the silicone to cure, water must diffuse into the part while the curing byproducts diffuse out. Because of this, a cure gradient is expected from the outer surfaces in towards the bottom surface in contact with the build plate. This can create a crosslink density difference within the specimen and reduce the local tensile strength at the bottom surface [37,42]. Another possible reason is the excess silicone in the first layer due to printing on a non-deformable surface (glass build plate). Since the same parameters were used for each layer, excess material exists on the first layer (as seen by the edge taper on the bottom layer) which may lead to imperfections and stress concentrations. The combination of these two phenomena may lead to more frequent fracture initiation from the bottom surface of the part.

The two weakest specimens also failed on the bottom surface. There is a much darker region, which indicates an initial crack propagation at a 45° (bottom view) with respect to the pull direction, around the crack initiation point for these two specimens. This indicates the combination of crosslink density difference and imperfections near the first layer also likely contributed to the failure initiation of those tensile specimens.

$X = 0.97$: Failure surfaces of the strongest 90° (1.59 MPa), weakest 90° (1.31 MPa), strongest $\pm 45^\circ$ (1.76 MPa), and weakest $\pm 45^\circ$ (1.24 MPa) AM tensile specimens with $X = 0.97$ are shown in Figure 3.12. The failure modes for these specimens have similarities, and differences, to specimens with $X = 1.00$. Both of the strongest specimens have failure surfaces that span mostly perpendicular to the pull direction but they failed at the top surface instead of the bottom surface. Visually, the top surfaces of $X = 0.97$ specimens appear to be smoother than $X = 1.00$ specimens due to reduced over extrusion. However, the failure started at the interface between the outline and the infill, indicating surface imperfections at that interface, particularly since the top layer does not experience the same type of deforming compression as layers below. Even though there are many internal voids at intersections between the outlines and infill (see Figure 3.12 and Figure 3.10), no failure initiated from these internal voids for both the strongest and weakest specimens.

For the weakest specimens, a much darker region around the crack initiation point exists. This darker region indicates an initial crack propagation at about 45° with respect to the pull

direction. The failure initiation point was different for the 90° (on the top) and ±45° (at the bottom).

X = 0.91: The failure surfaces of the strongest 90° (1.03 MPa), weakest 90° (0.66 MPa), strongest ±45° (1.25 MPa), and weakest ±45° (1.03 MPa) AM specimens with $X = 0.91$ are shown in Figure 3.12. Failure modes for these specimens are very distinct from the other AM specimens with higher compression factors. Unlike previous specimens that appear to initiate failure at a distinct point on the top or bottom surface, specimens with $X = 0.91$ have multiple internal failure points (indicated by the numerous dark sections within the part) caused by stress concentrations at the elongated voids. The average tensile strength of the 90° specimens (0.90 MPa) is markedly lower than the ±45° specimens (1.15 MPa) due to the elongated voids in the 90° specimens having a greater difficulty aligning along the direction of force and therefore experience greater stress concentrations at the corners. A reduction in cross sectional area could also impact the strength since only the external dimensions were measured.



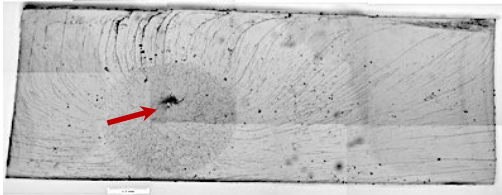
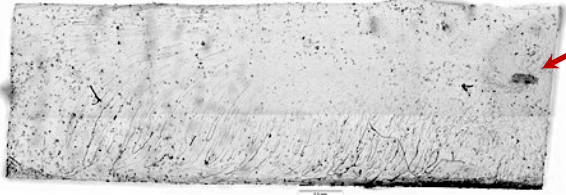
		Stamped	
		Strongest (1.94 MPa)	Weakest (1.33 MPa)
Top View			
Cross-Section			

Figure 3.12: Optical microscopy images of the cross-sectional and top views of failure tensile specimen surfaces (cont.).

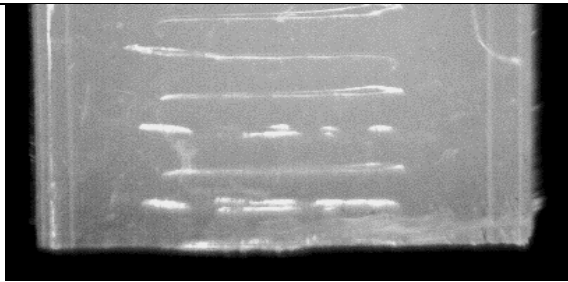
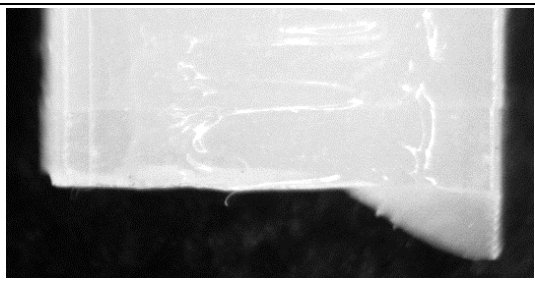

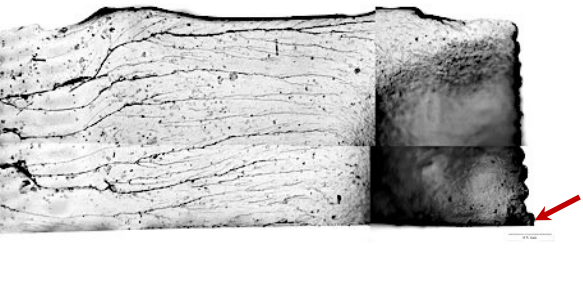
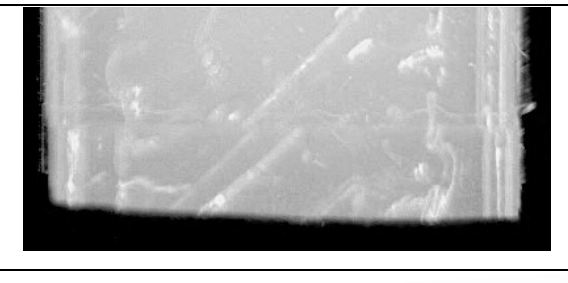
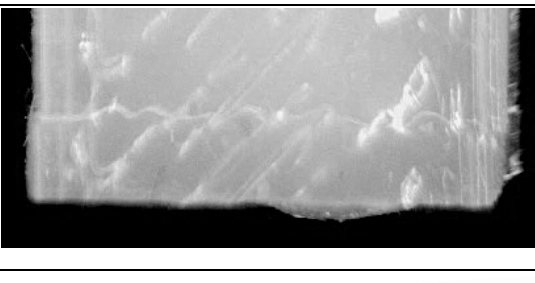
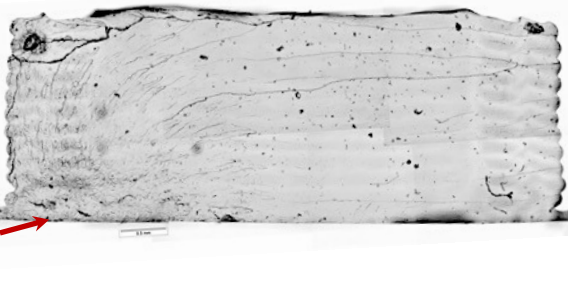
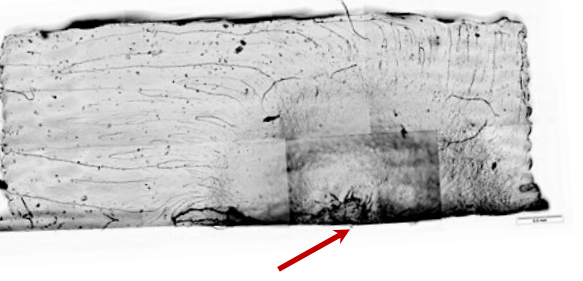
		$X = 1.0$	
		Strongest 90° (1.63 MPa)	Weakest 90° (1.28 MPa)
Top View			
Cross-Section			
		Strongest $\pm 45^\circ$ (1.76 MPa)	Weakest $\pm 45^\circ$ (1.26 MPa)
Top View			
Cross-Section			

Figure 3.12: Optical microscopy images of the cross-sectional and top views of failure tensile specimen surfaces (cont.).

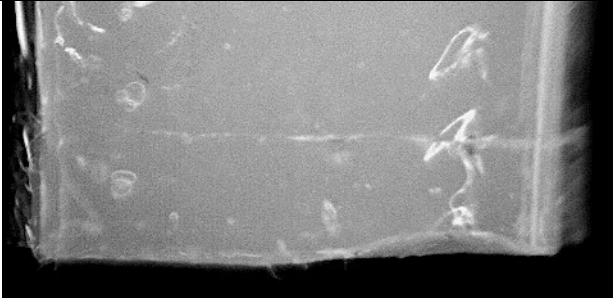
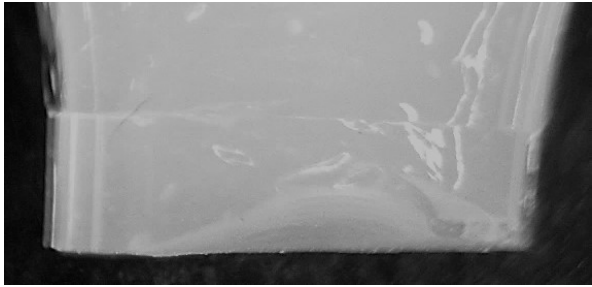
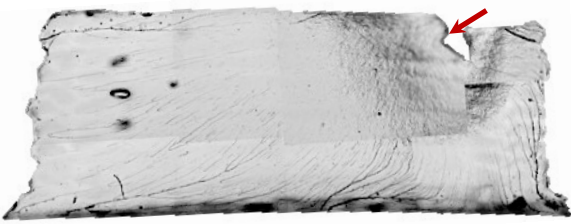
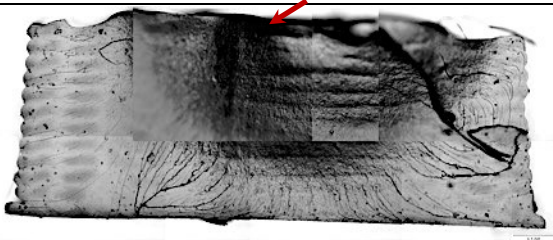
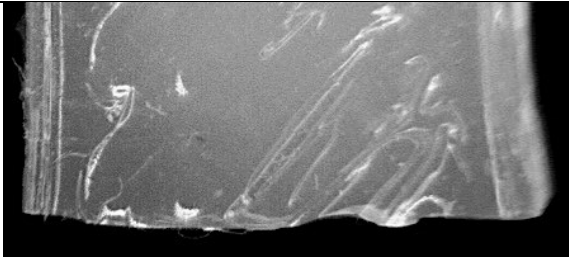
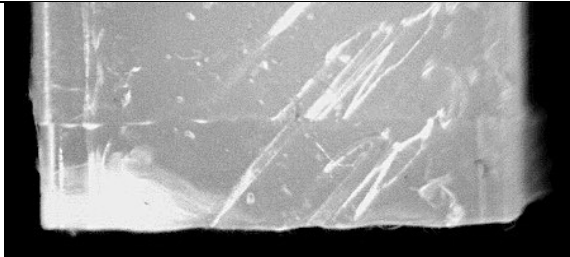
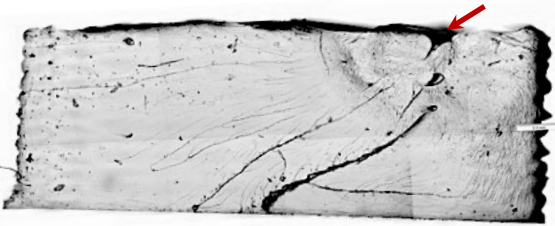
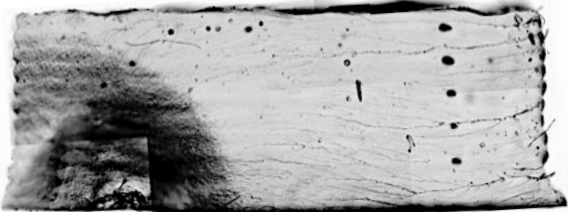
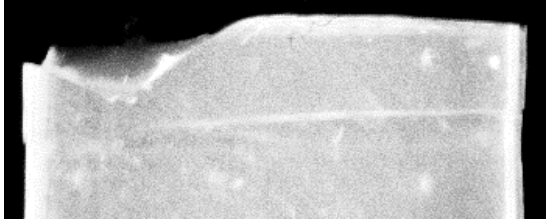
$X = 0.97$	
Strongest 90° (1.59 MPa)	Weakest 90° (1.31 MPa)
Top View	 
Cross-Section	 
Strongest ±45° (1.76 MPa)	Weakest ±45° (1.24 MPa)
Top View	 
Cross-Section	   <p style="text-align: center;">(Bottom View)</p>

Figure 3.12: Optical microscopy images of the cross-sectional and top views of failure tensile specimen surfaces (cont.).

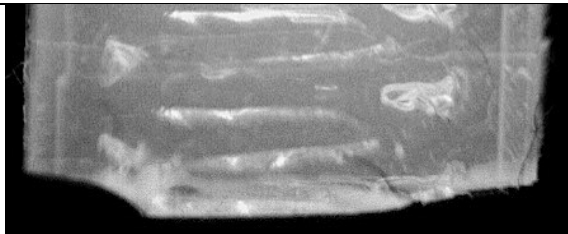
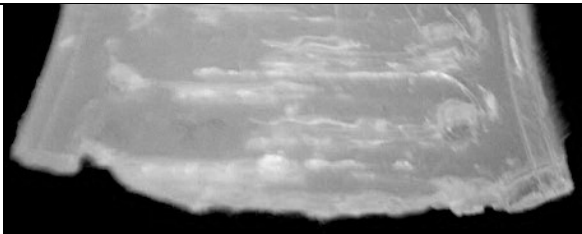
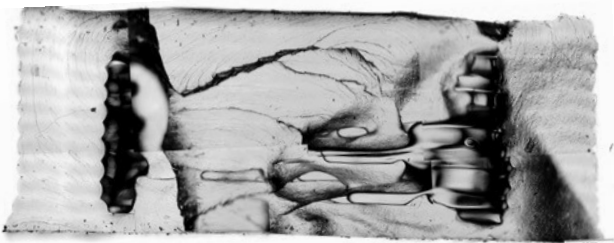

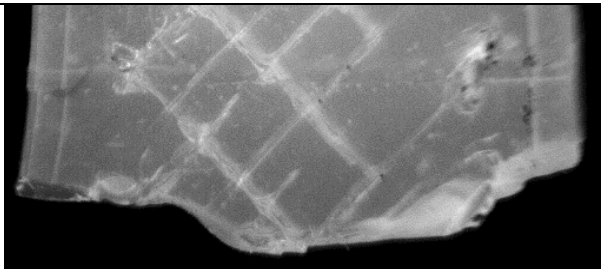
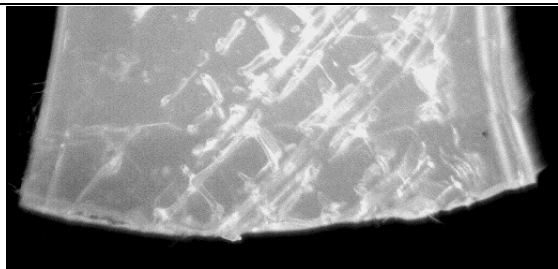
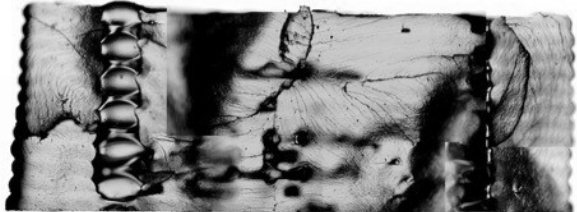
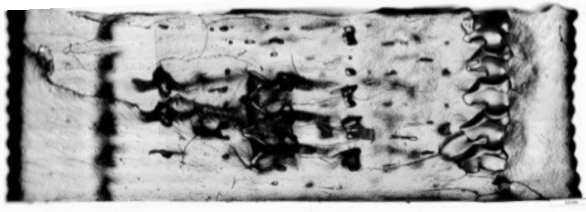
$X = 0.91$		
Strongest 90° (1.03 MPa)		
Weakest 90° (0.66 MPa)		
Top View		
Cross-Section		
Strongest $\pm 45^\circ$ (1.25 MPa)		
Weakest $\pm 45^\circ$ (1.03 MPa)		
Top View		
Cross-Section		

Figure 3.12: Optical microscopy images of the cross-sectional and top views of failure tensile specimen surfaces (cont.).

3.6 Conclusions

This study demonstrates that direct extrusion-based AM of silicone can produce isotropic parts nearly equivalent in strength to the stamped material. Compared to the 1.63 MPa average tensile strength of the baseline stamped specimens, the tensile specimens fabricated by AM with $X=1.00$ (“minimal void” configuration) and $X=0.97$ (“small void” configuration) and 90° and $\pm 45^\circ$ infill had a similar level of tensile strength, ranging from 1.44 to 1.51 MPa. These AM specimens were nearly indistinguishable from one another in strength. Even though there were visible voids, typically 300 to 500 μm in diameter and circular in shape, at the interface between the part outline and infill for the $X = 0.97$ specimens, high tensile strength was maintained because the voids were able to orient themselves along the direction of force with crack initiations typically occurring on the surface of the AM specimen.

As the internal void geometries resulting from the AM process transitioned in size from small and circular to a more elongated shape for $X=0.91$ (“large void” configuration), the average tensile strength significantly reduced to 1.15 MPa and 0.90 MPa for specimens with $\pm 45^\circ$ and 90° infill, respectively, with crack/failure initiation starting internally rather than on the surface.

For each set of process parameters tested, the 0° -O and 0° -NO specimens were consistently the worst performing in tensile strength. As seen in the failure analysis, this result was not specifically due to the infill direction but rather the internal tangency voids and poor edge surface finish resulting from the tool path required to create those specimens. These results will likely improve if a different print path was utilized which could eliminate these imperfections.

Based on these findings, when fabricating silicone parts with extrusion-based AM requiring high tensile strength, it is advantageous to select process parameters which have some compression ($X = 1$ and 0.97) in order to minimize elongated voids between adjacent line spacing. Voids that were less than approximately 500 μm and circular in shape had no measured effect on tensile strength. It is also important to minimize jagged edge geometry, internal tangency voids, and surface roughness. If these properties can be achieved, infill direction does not play a significant role in tensile strength of silicone parts fabricated by extrusion-based AM.

Although this study was performed using a single type of silicone, it is expected that the

overall findings will apply to any type of silicone (and potentially other flexible materials) produced by direct extrusion AM whereby the material chemically bonds to adjacent layers after deposition due to similar failure mechanisms.

Future research can be performed to examine the root causes of the top and bottom surface failure initiation points found in 90° and $\pm 45^\circ$ AM specimens with $X = 1.00$ and 0.97 . By adjusting the process parameters at and near the bottom and top layers it may be possible to further minimize layer imperfections and increase the tensile strength in the silicone AM parts. For example, by reducing the relative flowrate in the first layer to prevent over extrusion caused by a non-deformable build plate and increasing the relative flowrate on the top layer where there is less compression, it may be possible to reduce the imperfections found in the failure analysis thereby increase the tensile strength of the silicone AM parts.

CHAPTER 4
MEASUREMENT AND MODELING OF FORCES IN EXTRUSION-BASED ADDITIVE
MANUFACTURING OF MOISTURE-CURED SILICONE ELASTOMER

Nomenclature:

c	Distance between two adjacent silicone lines
d_i	Nozzle tip inner diameter
Q	Volumetric flow rate
t	Layer height
v	Nozzle speed in the layer
F_t	Total tangential force
F_{td}	Tangential force on deposit layer caused by the silicone bead dragging (F_{td}' – reactive force)
F_m	Tangential force on deposit layer caused by the nozzle contact with the silicone (F_m' – reactive force)
F_n	Total normal force
F_{ng}	Normal force on deposit layer caused by the weight of silicone (F_{ng}' – reactive force)
F_{nd}	Normal force on deposit layer caused by the deposition of the silicone (F_{nd}' – reactive force)
F_{nn}	Normal force on deposit layer caused by the nozzle interaction with the silicone (F_{nn}' – reactive force)

4.1 Introduction

Silicone elastomer deposited using direct extrusion additive manufacturing (AM) has demonstrated great potential for fabricating a wide variety of custom flexible parts, such as the thin-walled pneumatic actuators and parts with high elongation and fatigue life [15,16,43]. This AM process is particularly attractive over other AM methods, such as selective laser sintering, photopolymer jetting, and fused deposition modeling, because it enables the use of a wide variety of commercially available silicone elastomers, denoted as silicones, with broad material

properties ranging from 3 to 90 Shore A hardness, up to 1100% elongations, -65°C to 177°C functional temperature range, long fatigue life, and high chemical and UV resistance [14,20].

In direct extrusion AM, a nozzle moves line-by-line to directly extrude the material on the AM part, building up multiple layers to create a 3D object. Unfortunately, this process can generate forces which can act to deform and skew a soft AM part. This is a key challenge for extrusion-based AM of silicone because the low elastic modulus, ranging around 0.5 to 30 MPa, makes the parts easily deformable by forces generated during the extrusion of high-viscosity silicone fluid. Generally, the taller and thinner the part becomes, the greater the impact of the AM forces. However, by simply adjusting extrusion process parameters (e.g. flowrate, layer height, nozzle size, and acceleration), the AM forces are reduced and the maximum height of a soft, thin-walled part can be greatly increased. The larger these extrusion forces become on a silicone workpiece during AM, the greater the design space is limited. For example, as shown in Figure 4.1, the maximum height of soft silicone parts produced by extrusion-based AM can be significantly increased with lower extrusion forces. This research measures and studies the effects of silicone extrusion process parameters on forces for AM.

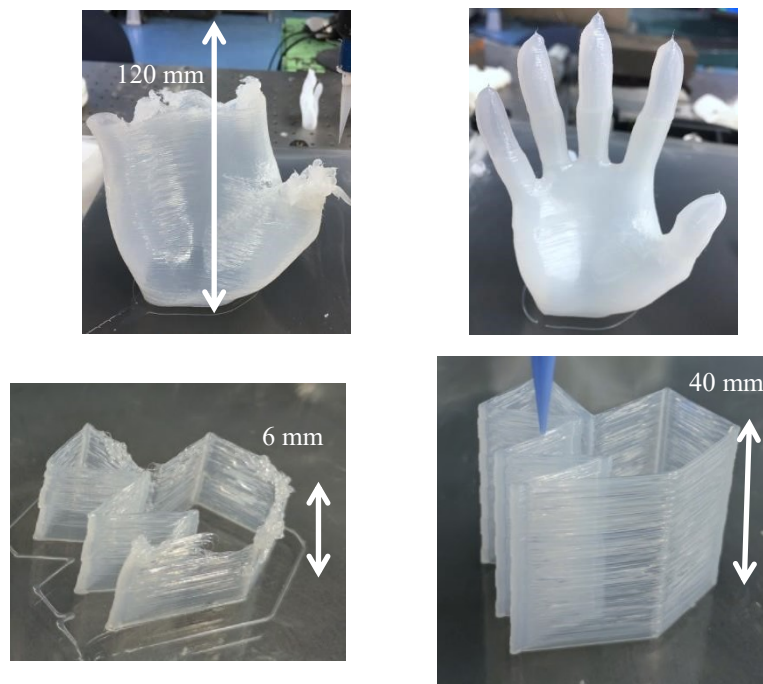


Figure 4.1: Tall soft silicone parts enabled by low force extrusion-based AM (left: high and right: low force in silicone extrusion).

Throughout an extrusion-based silicone AM process, external force is imparted in three modes: (1) machine vibration and build plate movement, (2) tangential and normal forces caused by silicone deposition and the nozzle tip, and (3) normal force caused by gravity. Forces due to machine vibration and build plate movement can be overcome through control of accelerations, stationary build plates using a prismatic-input delta robotic 3D-printer, and increasing the stiffness of the 3D-printer. Silicone deposition can create tangential forces due to the dragging or pulling of the extruded silicone between the AM part and moving nozzle tip and normal forces due to the momentum of the extruded silicone impacting the AM part. Additional tangential and normal forces may also be created from the nozzle side and bottom surfaces dragging through the deposited material. Finally, gravitational forces may cause creep or negatively affect thin overhanging structures but can be largely overcome through silicone cure methods and geometric design.

External forces have always existed in extrusion-based AM but were not taken into account for process parameter selection until soft materials became more prevalent. With rigid parts, such as those made from acrylonitrile butadiene styrene (ABS) produced using fused deposition modeling (FDM), a type of extrusion-based AM processes, the molten thermoplastic solidifies quickly after deposition from the nozzle (typically within seconds) and has high rigidity once cooled. This high rigidity allows the solidified material to resist forces imparted on it from the AM process. However, when silicone is used instead, the liquid silicone that is extruded from the nozzle may go through a chemical reaction to cure. This curing process typically takes minutes to hours, creating a high likelihood that subsequent layers of material will be deposited on the un-cured liquid form of the material. This allows for strong interlayer bonding strength but makes parts highly susceptible to the forces described above. Additionally, even if a silicone was able to cure in seconds, the cured state can still be extremely flexible and prone to deformation by the AM forces.

Although deformation of the soft silicone AM parts has been observed within and between the extruded layers [16,43], the research to measure and quantify the forces during the extrusion-based AM process is still lacking. Compliant silicone structures can be skewed by forces in the mN level. Therefore, understanding and modeling the forces in extrusion-based soft silicone AM is important. Plott et al. [43] showed that an adjacent line spacing increase of just 0.05 mm can significantly reduce the tensile strength of the part due to the creation of internal

voids between adjacent silicone lines. If a silicone part is deformed by even less than 1 mm, there is the potential for reduced tensile strength of over 30%. Furthermore, if the deformation is too large, overall part accuracy can quickly deteriorate and lead to a failed part, as shown in Figure 4.1 (left).

Fluid modeling has been applied to study the material flow and heat dissipation in AM. Die swelling is the radial expansion of the liquid material as it moves from a compressed, high pressure state within the nozzle to atmospheric pressure as it leaves the nozzle [44]. The swelling ratio, or the maximum diameter of the extruded material divided by the nozzle diameter, is typically 1.05 to 1.3 for FDM-like extrusion processes and is dependent on the material properties and process parameters [45,46]. Bellini [45] used computational fluid dynamics (CFD) to create a 2D model of the extruded material spreading process during and after deposition from the nozzle onto the build plate. Since the behavior of the melted filament in the extrusion nozzle is typically shear thinning, a power law dependency of the viscosity for the shear rate is used. One variation of the model included a nozzle tip as a contact condition while another variation neglected the nozzle tip. Results showed that the presence of the nozzle tip added stability to the material flow and that it smoothed and flattened the top surface of the deposited material. Subsequent layers were modeled by re-running the model using the geometry results from the previous layer as the base [45]. Results of this CFD model showed that extrusion-based AM of silicone can be simulated. The CFD modeling is adapted to study silicone extrusion force in AM and compared to experimental measurements to gain better understanding of the flow of silicone in layer deposition.

The forces in extrusion-based AM of silicone are first introduced. Details of the experimental setup for silicone extrusion and force measurement are then presented. Results of tangential and normal forces created during the AM process, along with this force ratio, are discussed and compared. Appendix A includes the preliminary CFD model, predicted force results, and a comparison to the experimental measurements.

4.2 Forces in Extrusion-based AM

The magnitudes of forces caused by extrusion-based AM of silicone are dependent on several factors including: the silicone viscosity, flowrate, nozzle speed, nozzle tip inner diameter, layer height, extruded silicone material mechanical properties, and geometry and material properties of the surface for deposition. Figure 4.2 shows the free body diagrams of four scenarios in extrusion-based AM. From Figure 4.2a-d, the flowrate, Q , is gradually increased. In Figure 4.2a, the extruded silicone is leaving the nozzle such that it is deposited onto a deposit layer or build plate without contacting the nozzle exterior surface. This scenario is not commonly seen in extrusion-based AM because it is more difficult to control where the material deposition is occurring. There are three main force components in this scenario: F_{ng} – normal force caused by the weight of the silicone line, F_{nd} – normal force caused by deposited silicone decelerating, and F_{td} – tangential force caused by the nozzle as it drags and stretches the extruded silicone on the deposit layer or build plate.

In Figure 4.2b, Q is increased and the left side of nozzle is dragging through the extruded bead of silicone, acting to flatten the top surface. In this scenario, the three forces that existed in the previous scenario are present (F_{ng} , F_{nd} , F_{td}) with the addition of the fourth force, F_{tn} , which is a tangential force caused by nozzle movement through the deposited silicone, and the fifth force, F_{nm} , which is a normal force caused by the nozzle interacting with the deposited silicone. Additionally, since more silicone is being deposited in a given space, F_{ng} will increase due to an increase in weight, F_{nd} will increase due to the greater momentum of the material as it leaves the nozzle and decelerates on the deposit layer/build plate, and F_{td} will decrease since the extruded silicone will not be stretched as much by the nozzle movement.

In Figure 4.2c, Q is increased further causing the silicone to flow forward from the inner diameter of the nozzle as it contacts the deposit layer. This outward push of silicone will create a flow field that leads in front of the nozzle opening. Through this phenomenon, it is expected that F_{td} will be eliminated since the extruded silicone is no longer being stretched by the nozzle movement. Conversely, F_{ng} and F_{nd} are expected to increase for the same reasons described in the previous scenario.

Finally, in Figure 4.2d, Q is increased so much that the material flow field has moved in front of the nozzle, causing the side of the nozzle to drag through the material in addition to the

bottom surface of the nozzle. In this scenario, it is expected that F_{ng} , F_{nd} , and F_{tm} will all be at the greatest level among four scenarios.

With an understanding of force originates in a given silicone AM scenario, it is important to measure the magnitude of these forces in each scenario. By determining these magnitudes, the process parameters can be optimized to minimize the part deformation and improve the accuracy and reliability of the extrusion-based AM for silicone and other soft materials. The next section explains the experimental setup to measure these forces.

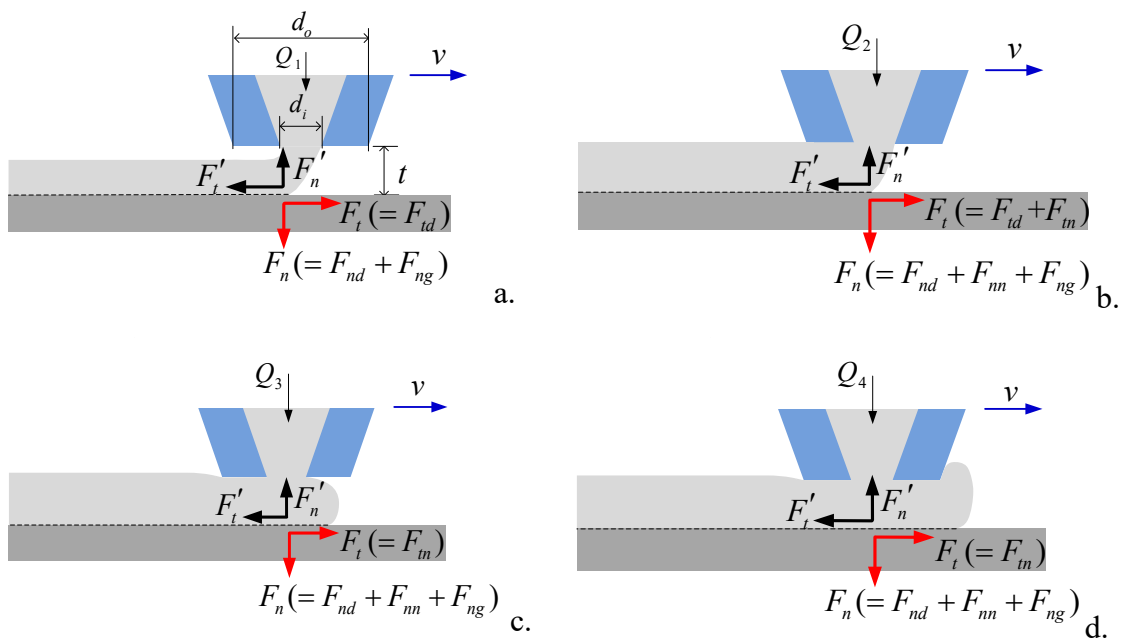


Figure 4.2: Free body diagrams of the extrusion-based AM forces between the silicone fluid and deposit layer (or build plate) with increasing flowrate, from Q_1 to Q_4 , at a constant layer height, t , and nozzle velocity, v .

4.3 Experimental Setup

This section outlines the silicone material, AM machine and setup, experimental design, and displacement to force conversion for force measurement of the silicone extrusion-based AM.

4.3.1 Silicone Material and Cure Parameters

A one-part oxime cure silicone elastomer (Dow Corning[®] 737, Dow Chemical, Midland, Michigan) was used as the base material for all experiments in the study. This silicone has a 33 Shore A durometer hardness, over 300% elongation, over 1.2 MPa tensile strength, and a specific gravity of 1.04 [36]. This silicone has a zero shear rate viscosity of about 62.5 Pa·s and begins curing with exposure to atmospheric moisture [15]. Once exposed to this moisture, it has a skin-over time of 3-6 minutes, a tack-free time of 14 minutes, and a cure to handling time of 24 hours [36].

4.3.2 AM Machine and Setup

The experimental setup for force measurement of extrusion-based AM of silicone is shown in Figure 4.3. The system consists of six key components: (1) a prismatic-input delta robotic 3D-printer as a motion control platform based on an open-source FDM machine (Rostock Max[™] V3 by SeeMeCNC[®], Goshen, Indiana, USA) which allows for XYZ nozzle movement independent of the stationary build plate, (2) a progressive cavity pump and its controller (Model preeflow eco-PEN 450 pump and Model EC200 controller by Viscotec, Töging am Inn, Germany) to dispense the silicone with a dosing accuracy of $\pm 1\%$ [29], (3) syringe barrels (Model Optimum by Nordson EFD, Westlake, Ohio) pressurized to 70 ± 10 kPa which feed the progressive cavity pump with silicone while preventing the introduction of air bubbles into the silicone, (4) a tapered nozzle with either 22 gauge (0.41 mm), 25 gauge (0.25 mm) or 27 gauge (0.20 mm) tip inner diameter (Model SmoothFlow[™] by Nordson EFD, Westlake, Ohio) to deposit the silicone on the cantilevered plate, (5) a cantilevered plate consisting of a polylactic acid (PLA) base, brass beam, PLA top plate, and mirror, and (6) a laser displacement sensor (Model LK-G10 by Keyence, Itasca, Illinois, USA) with 0.02 μm repeatability and $\pm 0.03\%$ linearity over ± 1 mm measuring range. The laser displacement sensor was connected to a display panel (Model LK-GD500 by Keyence, Itasca, Illinois, USA) and the LK-Navigator software (Keyence) which records the sensor displacement data. A 3 Hz low-pass filter was used to smooth the data since the nozzle moves about the square test part at approximately 1 Hz. Due to the sensitivity of the force measurement setup, each moving component is isolated from one another and fixed to an optical table with vibration dampening.

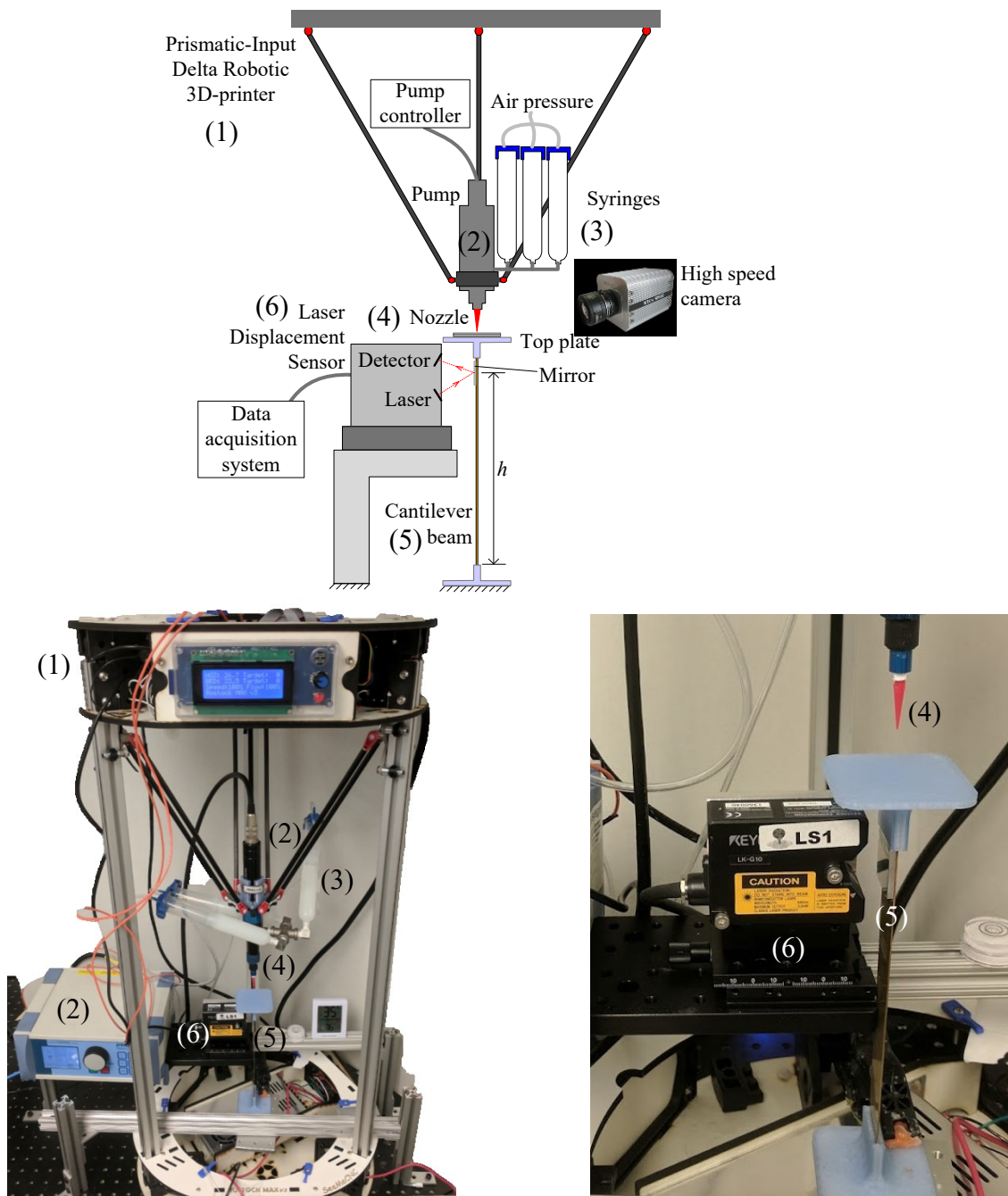


Figure 4.3: Experimental setup for extrusion-based silicone AM including: (1) delta robotic motion control platform, (2) progressive cavity pump and controller, (3) pressurized syringe barrels, (4) tapered nozzle, (5) cantilevered plate, and (6) laser displacement sensor.

4.3.3 Experimental Design

To test the effects of key parameters on the forces experienced by a soft part created through extrusion-based AM, a parametric study was performed. Three key process parameters were varied: flowrate Q , layer height t , and nozzle diameter d_i , as listed in Table 4.1. The nozzle speed in the layer, v , was held constant at 20 mm/s. The parameter range was selected based on previous studies in extrusion-based silicone AM [16,43] and preliminary exploration of process parameters for the AM of thin-walled silicone towers.

Table 4.1: Key AM process parameters used for parametric study.

Parameter	Value
Q [ml/min]	0.10, 0.16, 0.22, 0.28, 0.34, 0.40
t [mm]	0.10, 0.15, 0.20
d_i [mm]	0.20, 0.25, 0.41

A rounded-edge square part, as shown in Figure 4.4, was utilized for silicone extrusion experiments. The rounded-edge square part features a single line wall thickness with 25×25 mm side spacing and 3 mm total height. Four corners of the square are rounded with 4 mm radius to avoid rapid acceleration during the AM process. The part is printed using a continuously increasing layer height, rather than the discrete jump in height for each layer, to further minimize any rapid acceleration.

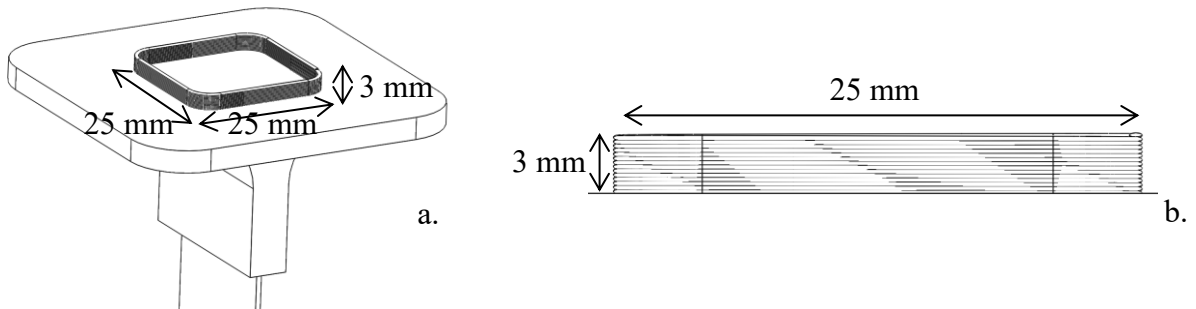


Figure 4.4: The (a) perspective and (b) side views of the single line wall rounded-edge square part for experimental force measurement ($25 \text{ mm} \times 25 \text{ mm} \times 3 \text{ mm}$) with 4 mm corner radius.

Figure 4.5 shows the process of building this rounded-edge square part on the cantilevered build plate. The square was centered on the platform such that two opposite sides were parallel and the other two opposite sides were perpendicular to the long axis of the cantilever beam. Due to this print orientation relative to the cantilever beam, specific displacements (and forces) are captured at different sections of the part building process.

Looking first at point A_1 , Figure 4.5a, the nozzle is moving parallel to the long axis of the cantilever beam. At this point, only the normal force, F_n , can deflect the beam. According point A_1 on the cantilever displacement vs. time graph, Figure 4.5f, the deflection of the beam at A_1 is small due to F_n since the effective moment arm for F_n is only 12 mm versus the 197 mm moment arm for F_t . The next section explains this in further detail.

As the nozzle rounds the corner and moves to point A_2 , as shown in Figure 4.5b, F_t deflects the beam along the direction of the nozzle movement with a 197 mm moment arm while F_n deflects the beam in the opposite direction of the nozzle movement with a 12 mm moment arm. From Figure 4.5f, the displacement at point A_2 (about 0.014 mm) is much higher than that at point A_1 , indicating that forces which comprise F_t are well detected by the experimental setup in comparison to F_n .

As the nozzle continues to travel past A_2 and reaches point M_1 , Figure 4.5c, the nozzle is directly above the cantilever beam. At this point, F_n no longer influences the beam deflection and only F_t is measured.

Once the nozzle moves past point M_1 to point B_1 , Figure 4.5d, both F_t and F_n act to deflect the beam along the direction of nozzle travel. As the nozzle rounds the corner to point B_2 , F_t is again moving parallel to the long axis of the cantilever beam and only the displacement due to F_n is detected. This cycle then repeats but in the opposite direction as the nozzle moves from point B_2 to C_1 , C_2 to D_1 , and D_2 to A_1 , as seen in Figure 4.5e-f.

In Figure 4.5f, there is a slope from points A_2 to B_1 and C_2 to D_1 . This can be due to F_n creating a moment on the beam, the momentum of the cantilever beam and top plate, and potential extrusion variations on the corners where the velocity might vary. Because of these potential effects, F_n is only calculated from points D_2 to A_1 and B_2 to C_1 , while F_t is only calculated at points M_1 and M_2 . These calculations are detailed in the next section.

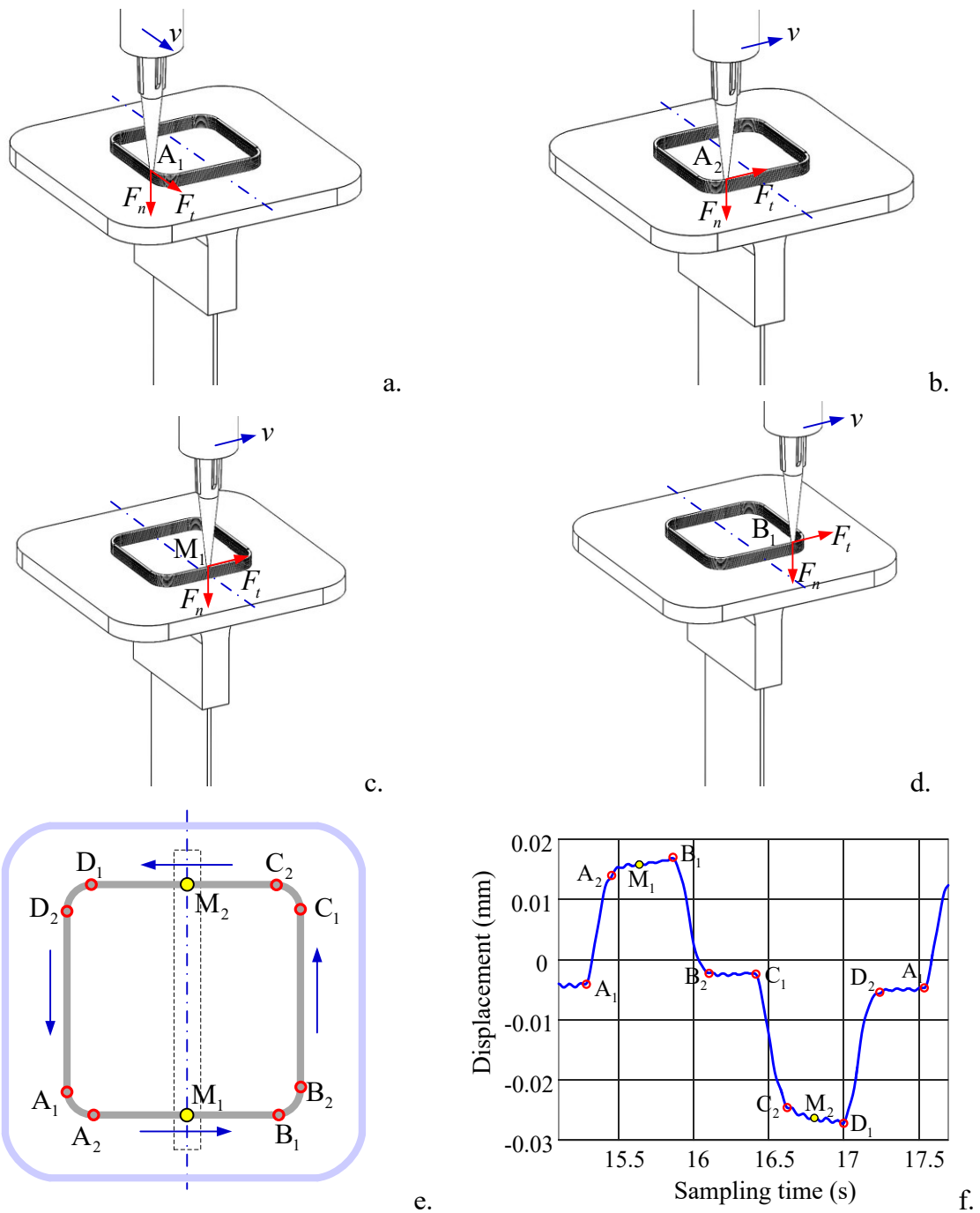


Figure 4.5: A rounded-edge square shape silicone part built on the cantilever beam. The displacement of the beam is measured by the laser displacement sensor (sample data in (f)). F_n is measured from points D_2 to A_1 and B_2 to C_1 ; F_t is measured at points M_1 and M_2 .

4.3.4 Displacement to Force Conversion

This section describes the procedure of converting the measured displacement of the cantilever beam to F_t and F_n . Three free body diagrams, as shown in Figure 4.6, are used to derive the force equations.

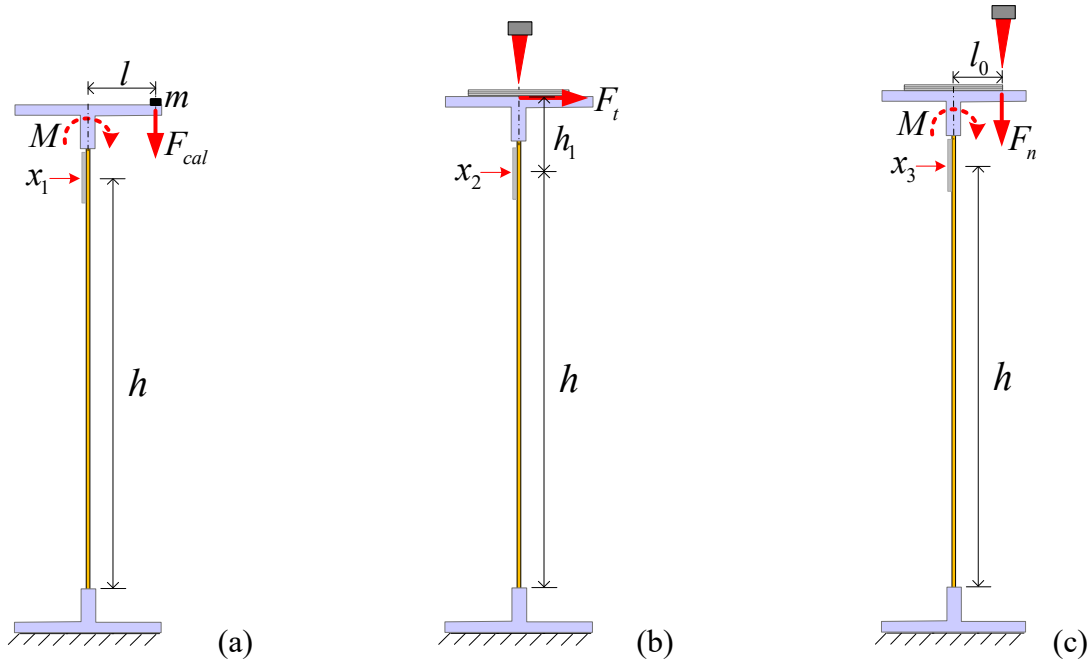


Figure 4.6: (a) Free body diagram of force vs. displacement calibration of the cantilever beam. A known mass generates a coupled moment M at the free end of the beam which creates displacement x_1 . (b) Free body diagram of the force imparted on the cantilever beam due to the F_t . (c) Free body diagram of the force imparted on the cantilever beam due to F_n .

4.3.4.1 Cantilever Beam Calibration Curve

Although F_t and F_n could be approximated from the beam displacements using beam bending theory and elastic modulus assumptions, a calibration curve was created to improve the force estimation accuracy.

To obtain the calibration curve, a series of six metallic washers with various masses (m) were placed on the top plate at a known distance, l , from the center of the cantilever beam, Figure 4.6a. These masses create a normal force $F_{cal} = mg$, where g is the acceleration due to gravity. F_{cal} creates a coupled moment M at the free end of the cantilever beam which causes the

displacement x_1 of the mirror. This displacement is measured by the laser displacement sensor (Figure 4.3). Six masses for calibration were adjusted to make the range of displacement x_1 within that which was observed during the AM experiments. Results of these six coupled moments, corresponding displacements, and calibration line are shown in Figure 4.7. The relationship between the mass and its moment on the cantilever beam and the displacement of the beam is linear in the measured range.

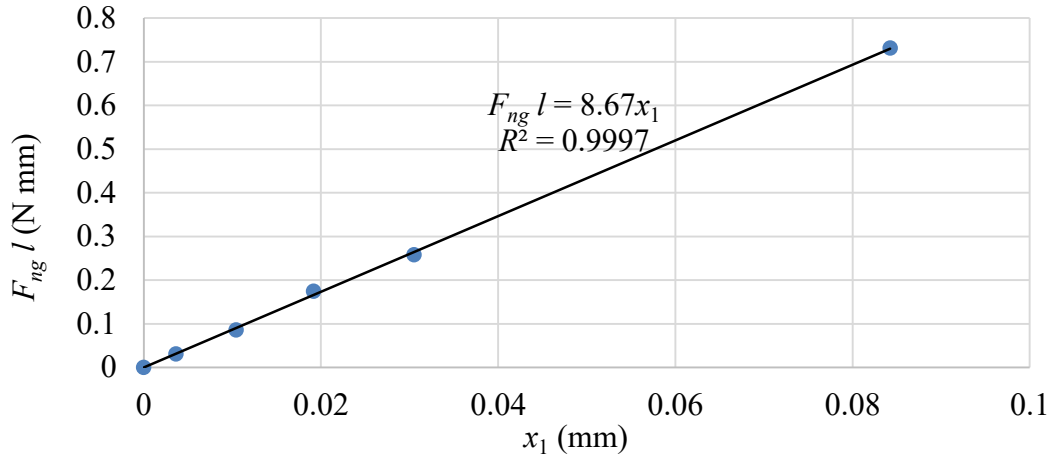


Figure 4.7: Calibration curve to convert cantilever beam displacements to F_t and F_n .

Using the cantilever beam bending equation for a coupled moment M at the free end [47] and substituting $M = F_{cal} l = mgl$,

$$x_1 = \frac{Mh^2}{2EI} = \frac{F_{cal}lh^2}{2EI} = \frac{mglh^2}{2EI} \quad (4.1)$$

where h is the distance from the fixed base of the cantilever beam to the laser measurement point ($h = 156$ mm in this study), E is the elastic modulus of the beam material, and I is the second moment of area of the beam. Together, EI is the experimentally determined constant of the beam. It is also assumed that the top plate is rigid and the mirror extending slightly below the point x_1 has a negligible effect on the overall beam bending.

Rearranging Eqn. (4.1) and substituting the linear fit in Figure 4.7 along with $h = 156$ mm, the constant $EI = 105$ kN mm² is calculated.

Additionally, since dimensions of the cantilever beam can be easily measured, the second moment of area, I , can be calculated and substituted in EI to determine the modulus of the beam, E . The second moment of area for a rectangular beam is $I = \frac{bd^3}{12}$ where b is the measured width of the beam (25.83 mm) and d is the measured thickness of the beam (0.82 mm). The $I = 1.19 \text{ mm}^4$ and $E = 88.9 \text{ GPa}$, which is reasonable for the brass cantilever beam material.

4.3.4.2 Tangential Force F_t Conversion

With these calibration results, the displacements recorded during the silicone extrusion experiments at points M_1 and M_2 , Figure 4.5f, can be converted to F_t using the beam bending equation for a concentrated load F_t at the free end [47],

$$x_2 = \frac{F_t(h^3 - 3(h+h_1)h^2)}{6EI} \quad (4.2)$$

where x_2 is the displacement of the mirror caused by F_t and h_1 is the distance between the laser measurement point and the cantilever top plate surface ($h_1 = 41.0 \text{ mm}$, as shown in Figure 4.6b). Eqn. 4.2 can be rearranged and simplified to solve for F_t ,

$$F_t = \frac{6x_2EI}{2h^3 + 3h_1h^2} \quad (4.3)$$

4.3.4.3 Normal Force F_n Conversion

From the displacement data, the total normal force F_n can be calculated when the nozzle is extruding between points D_2 to A_1 and B_2 to C_1 , as shown in Figure 4.5. Using the cantilever beam bending equation for a coupled moment M at the free end in Figure 4.6c,

$$x_3 = \frac{Mh^2}{2EI} = \frac{F_n l_0 h^2}{2EI} \quad (4.4)$$

where $M = F_n l_0$ and l_0 is the distance from the center line of the cantilever beam to the center of the nozzle when extruding between points D_2 to A_1 and B_2 to C_1 (12 mm), as shown in Figure 4.6c.

Rearranging Eqn. 4.4, we can solve for F_n .

$$F_n = \frac{2x_3EI}{l_0h^2} \quad (4.5)$$

While this equation provides the total normal force, F_n , it is also possible to calculate the three force components which compose the total normal force, F_{nd} , F_{ng} , and F_{nm} .

- F_{nd} : The force component F_{nd} is the normal force caused by deposited silicone decelerating as it impacts the build plate or part. Using the equation for jet forces on a stationary plate, the normal force component F_{nd} can be calculated.

$$F_{nd} = Q\rho V \quad (4.6)$$

Where ρ is the density of the silicone and V is the exit velocity from the nozzle.

Since values of Q (0.10 – 0.40 ml/min), ρ (1040 kg/m³), and V (12.6 – 212.2 mm/s) are known from the process parameters and material used, F_{nd} can be calculated. Results are shown in Figure 4.8. The smaller the nozzle, the greater F_{nd} becomes for a given Q .

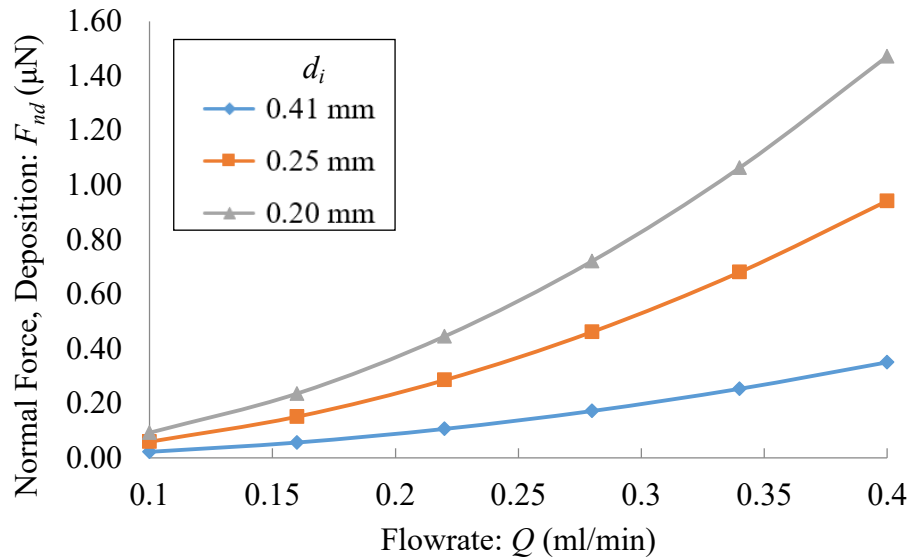


Figure 4.8: Theoretical F_{nd} for each set of process parameters in this study.

- F_{ng} : The force component F_{ng} is the normal force due to the weight of the deposited silicone. F_{ng} is calculated as:

$$F_{ng} = Q\rho s \quad (4.7)$$

where s is the time duration of material deposition. Since F_{ng} changes over time and the rounded-edge square part is axisymmetric, the amount of silicone deposited on one layer between the points D_2 to A_1 or B_2 to C_1 was calculated. The nozzle moves at a speed $v = 20$ mm/s and the length between those points (D_2 to A_1 and B_2 to C_1) is approximately 20 mm, therefore the weight of silicone deposition for 1 second was calculated. These results are shown in Figure 4.9. F_{ng} varies linearly with Q and is not dependent on d_i .

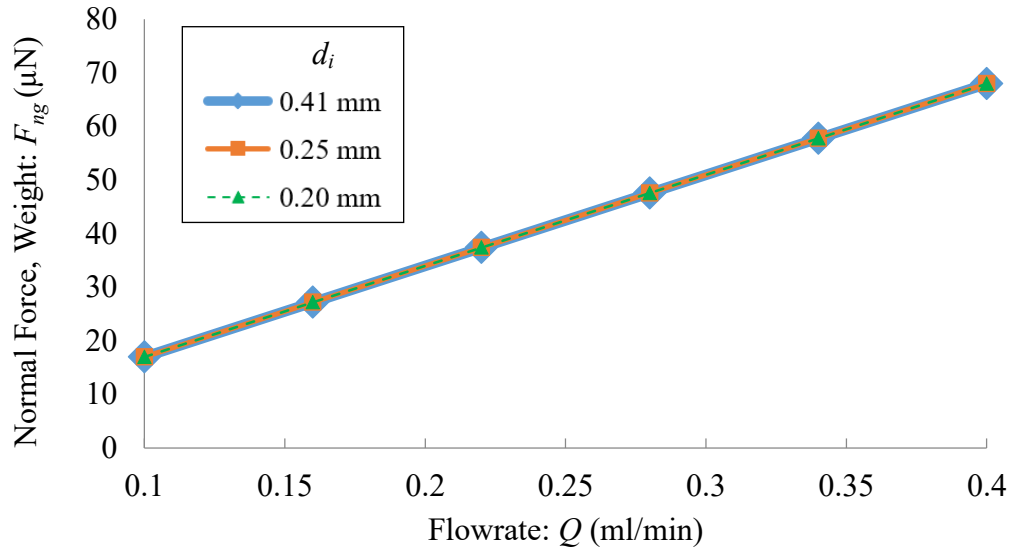


Figure 4.9: Theoretical F_{ng} for each set of process parameters in this study.

- F_{nn} : The force component F_{nn} is the normal force caused by the nozzle interaction with the silicone and is dependent on the level of normal compression between the extruded silicone and the nozzle tip. F_{nn} can be calculated by subtracting the other normal force components, F_{ng} and F_{nd} , from the total measured normal force F_n .

$$F_{nn} = F_n - F_{nd} - F_{ng} \quad (4.8)$$

4.4 Results

The force results obtained from the experimental and CFD models are presented in this section.

4.4.1 Cantilever beam displacements

Following the procedure outlined in Section 3, displacements of the cantilever beam were recorded throughout 54 different experiments corresponding to the process parameters listed in Table 4.1. An example of a displacement vs. time graph is shown in Figure 4.10. In the beginning layers (0-4 s), there is a significant variability due to: (1) inconsistencies in the initial material flow Q from the extrusion pump as internal pressure builds in the nozzle before equilibrium pressure/flow is reached, (2) variations in initial layer height due to imperfect build plate/nozzle leveling, and (3) over or under extrusion on the initial layers due to a non-deformable build plate. To compensate for this, the initial displacement data was ignored until a more uniform, periodic displacement was observed, typically after 5 seconds.

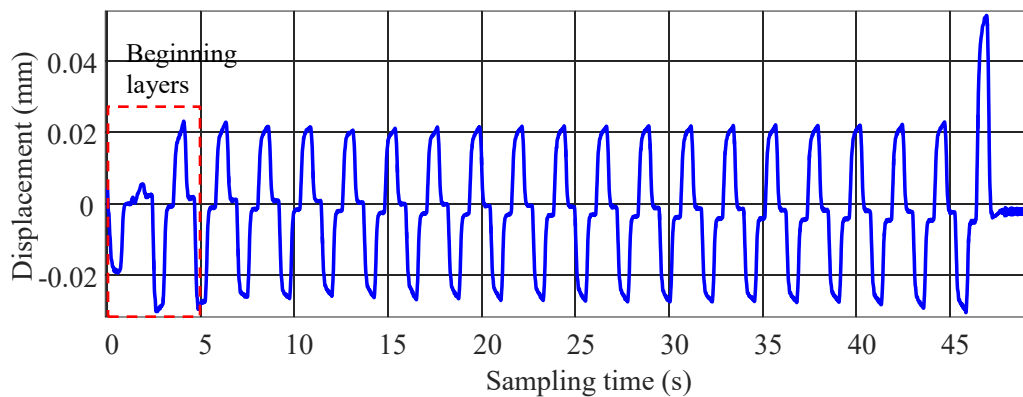


Figure 4.10: Displacement vs time graph for the following AM process parameters: $Q = 0.34$ ml/min, $t = 0.15$ mm, and $d_i = 0.41$ mm.

4.4.2. Experimental Results of F_t

To determine the magnitude of the tangential force, F_t , the first 20 peaks were selected after equilibrium was reached in the system. As shown in Figure 4.11, a least squares fit was imposed on the data to identify midpoints of the displacement peaks (points M_1 and M_2 in Figure 4.5).

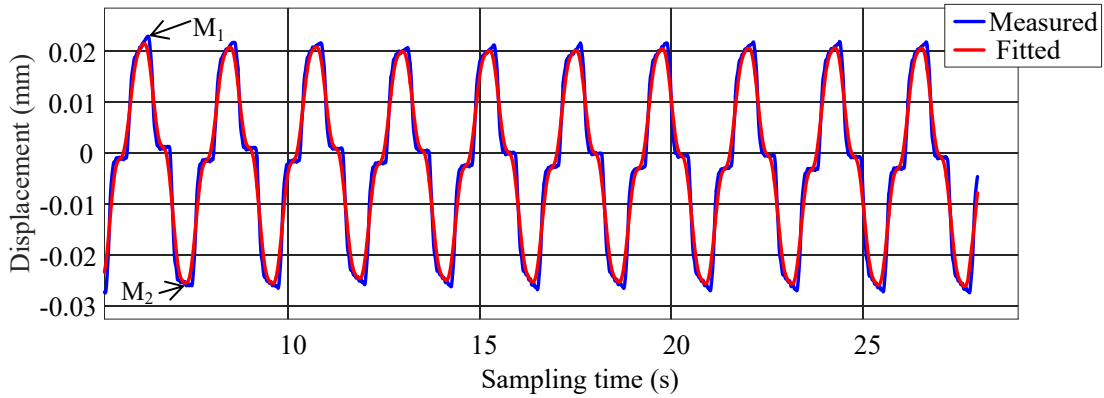


Figure 4.11: Selected displacement data including 20 peaks (10 layers) and the least squares fit to find the points M_1 and M_2 .

These peak displacements were converted to F_t using Eqn. 4.3. To determine the value of F_t and its associated error, the magnitudes of the first peak (point M_1) and valley (point M_2) were averaged to obtain the average F_t for the given layer. This step was then repeated for the next 10 layers to compensate for any potential measurement drift. The average of these F_t values was then calculated to determine the final F_t and the measurement error equals the standard deviation. Results are presented in Figure 4.12.

Figure 4.12 illustrates that process parameters can significantly impact F_t which ranges from 0.03 mN ($Q = 0.10$ ml/min, $d_i = 0.25$ mm, $t = 0.20$ mm) to 4.01 mN ($Q = 0.40$ ml/min, $d_i = 0.41$ mm and $t = 0.10$ mm). The wide range of F_t is due largely to the interaction between the nozzle tip and deposited silicone, as shown in Figure 4.2. In general, if the nozzle tip is not dragging through the deposited silicone bead, Figure 4.2a, F_t is significantly lower than if the nozzle tip is dragging through the deposited silicone bead, Figure 4.2b-d. The more extruded silicone the nozzle tip is dragging through, the greater F_t becomes.

One example where Q had a large influence on the interaction between the nozzle tip and extruded silicone occurred with $d_i = 0.25$ mm and $t = 0.15$ mm. At Q of 0.22 ml/min and below, F_t was very small (0.06 to 0.10 mN). Using a high-speed camera, we observed that although the nozzle was very close to the extruded silicone line, it did not drag through it, Figure 4.13a (top). This was also confirmed in Figure 4.13a (bottom) through the cross-section analysis which shows that the top of the silicone bead was smooth and rounded, indicating that no dragging occurred by the nozzle. The width of wall is the thinnest, about 1.20 mm, among all four Q in

Figure 4.13. Based on the incompressible flow condition, the theoretical value of line width is 1.22 mm, which is close to the measured width of 1.20 mm.

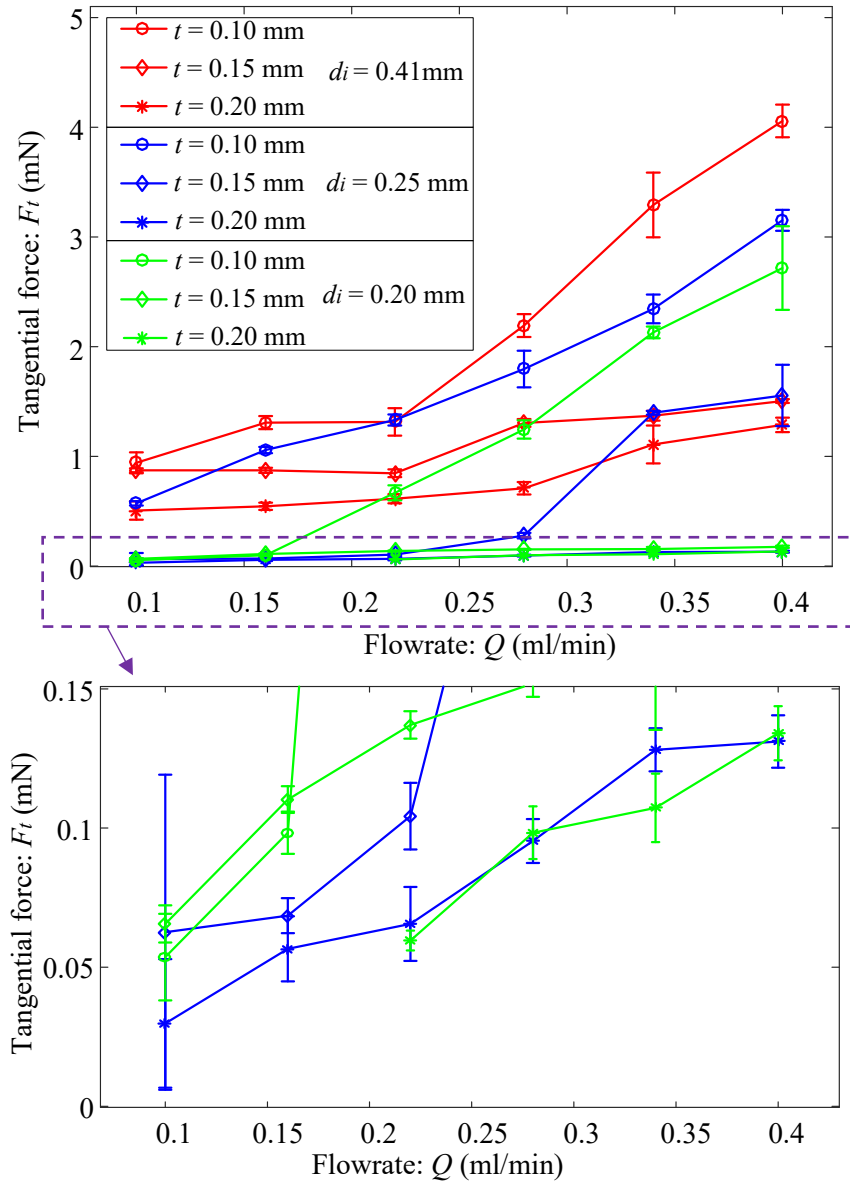


Figure 4.12: The average and standard deviation of F_t for three nozzles ($d_i = 0.41$, 0.25 , and 0.20 mm) at three layer heights ($t = 0.20$, 0.15 , and 0.10 mm).

When Q was further increased to 0.28 ml/min, we observed a distinct increase in F_t (0.27 mN). Using the high-speed camera and cross-section analysis, the back edge of the nozzle is

confirmed to have slightly dragged through the deposited silicone bead, Figure 4.13b (bottom). The width of the wall increased to 1.57 mm (vs. 1.56 mm calculated based on the incompressible flow condition).

Increasing Q further to 0.34 ml/min, we again observed an increase in F_t (1.38 mN). Through the high-speed camera images and cross-section analysis in Figure 4.13c, a greater area of the nozzle was dragging through the deposited silicone but there was still no buildup on the front of the nozzle. The width of the wall was 1.80 mm (vs. 1.89 mm calculated based on the incompressible flow condition).

Finally, with Q increased to the highest level, 0.40 ml/min, we saw the largest average F_t (1.54 mN). Through the high-speed camera and cross-section analysis in Figure 4.13d, the nozzle was dragging through the deposited silicone and excess silicone was building up on the sides of the nozzle. The width of the wall was 2.24 mm (vs. 2.22 mm calculated based on the incompressible flow condition), the thickest among all four flow rates.

From these results, we conclude that in order to minimize the tangential force F_t , it is ideal to select process parameters where the nozzle does not contact the extruded silicone line, Figure 4.2a, since $F_{td} \ll F_m$.

There are a number of approaches that can achieve this result with varying degrees of success. For example, selecting a large layer height, t , may prevent the nozzle from contacting the extruded silicone and yield a low F_t ; however, if this layer height is too large then the extrusion accuracy can be negatively affected. Additionally, this higher layer height may reduce the compression on the extruded silicone layers below, making it more difficult to achieve a “voidless” mesostructure [16].

Another approach might utilize a low Q . However, as Q decreases (all else equal), the extruded line width becomes thinner. A thinner line width may become problematic for fabricating thin wall structures as it will have a low structural stiffness and be more susceptible to the deformation by AM forces.

Yet another approach could include the use of a very small d_i to increase F_n , the force at which the deposited silicone compresses extruded silicone layer. This could be used to push the deposited silicone out of the way from the nozzle, preventing the nozzle from dragging and creating a large F_t . However, with high F_n , the part may deflect downward leading to accuracy issues.

As a general rule to reduce F_t , it is recommended to select process parameters which create an extrusion scenario where the nozzle is very close to the deposited surface, as shown in Figure 4.2b, while still residing in the extrusion scenario shown in Figure 4.2a and Figure 4.13a. This ensures a low F_t while at the same time compressing previous layers to minimize internal voids, maintaining deposition accuracy, and having a bead width with enough structural stability for producing thin-walled parts.

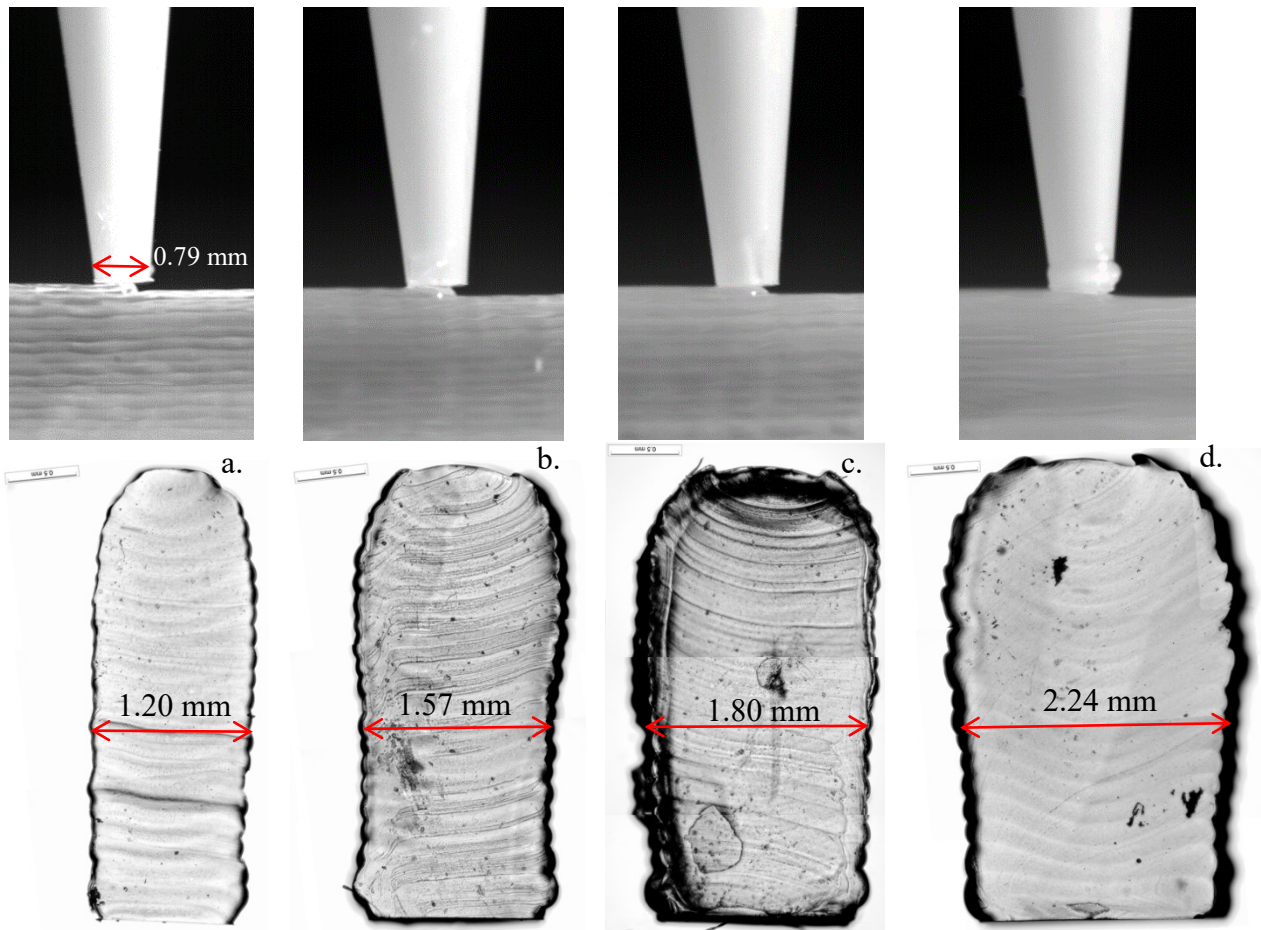


Figure 4.13: High-speed camera images taken during the extrusion process and corresponding cross-sectional images taken after curing with $d_i = 0.25$ mm, $t = 0.15$ mm, and $Q =$ (a) 0.22, (b) 0.28, (c) 0.34, and (d) 0.40 ml/min. As Q increased, the degree to which the nozzle impacts the extruded silicone increases, thereby increasing F_t and wall thickness.

4.4.3. Experimental Results of F_n

To determine the magnitude of F_n , regions from D_2 to A_1 and B_2 to C_1 , as shown in Figure 4.5 and Figure 4.14, were identified in the displacement vs. time graph. The difference of average displacement between regions D_2 to A_1 and B_2 to C_1 was $2x_3$, as shown in the close-up view in Figure 4.14. The x_3 in three selected measurement regions equally spaced in the 3rd to 11th layers was identified. Eqn. 4.5 was used to convert the measured x_3 to F_n . Three measured F_n values were averaged to calculate the average F_n for a given set of process parameters.

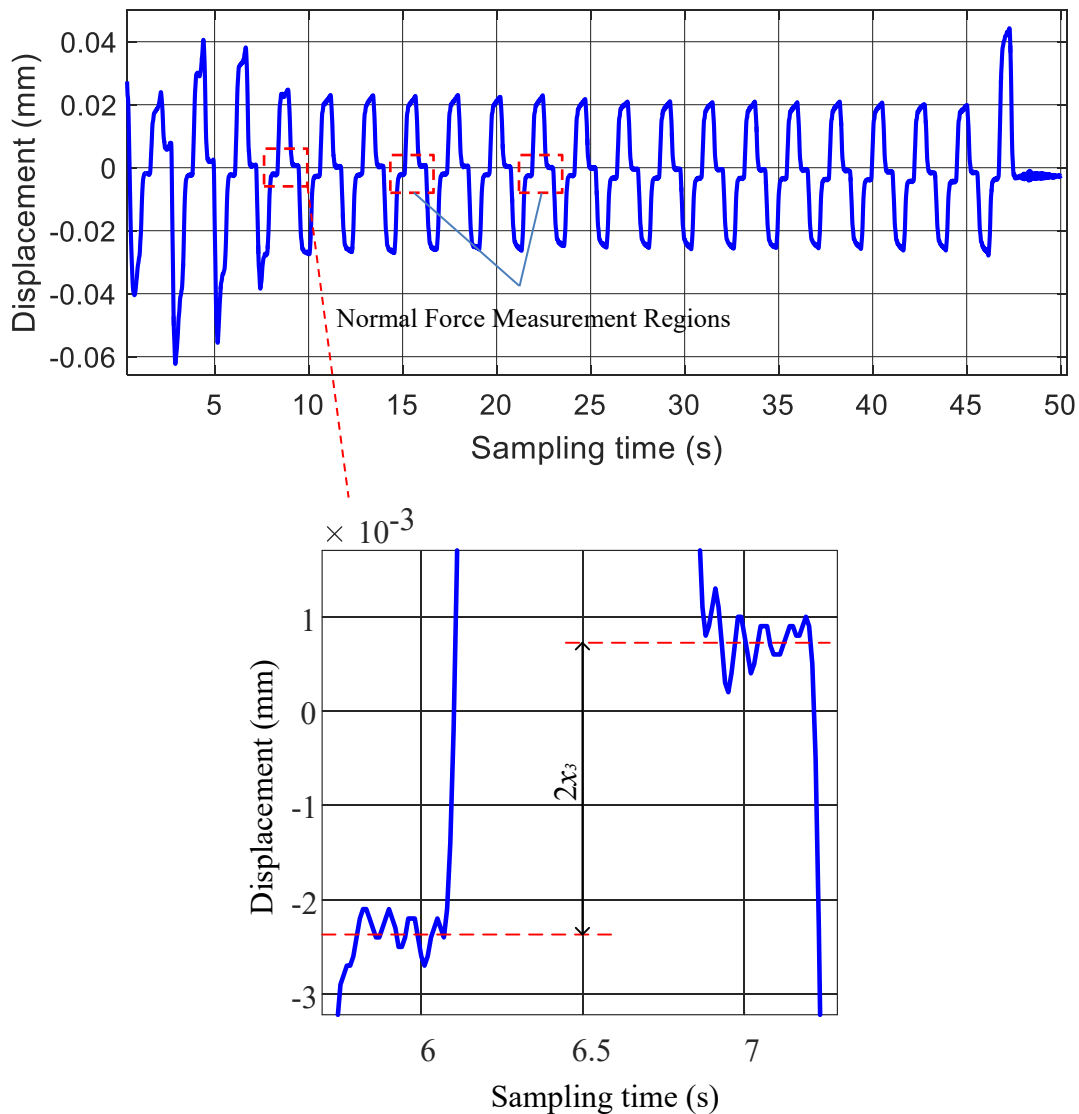


Figure 4.14: Displacement vs time graph for experimental F_n measurement: $Q = 0.40$ ml/min, $t = 0.15$ mm, $d_i = 0.25$ mm. Three regions where only F_n acts to deflect the cantilever beam were averaged to determine F_n for a given set of process parameters.

In some of the displacement vs. time data, especially with process parameter settings where the nozzle does not drag through the extruded silicone material (Figure 4.2a), F_n was undetectably small (experimental setup can only detect F_n values > 0.1 mN) and assumed to be 0. This correlates well to the theoretical normal force component calculations for F_{nd} and F_{ng} . Since the nozzle is not in close contact with the extruded silicone, F_{nn} is close to 0. Additionally, since the range of the experimental setup is limited to the mN force scale, it is expected that F_{nd} and F_{ng} would be undetectable since, in theory, F_{nd} and F_{ng} will be in the μN scale. An example of the low, undetectable F_n data is shown in Figure 4.15.

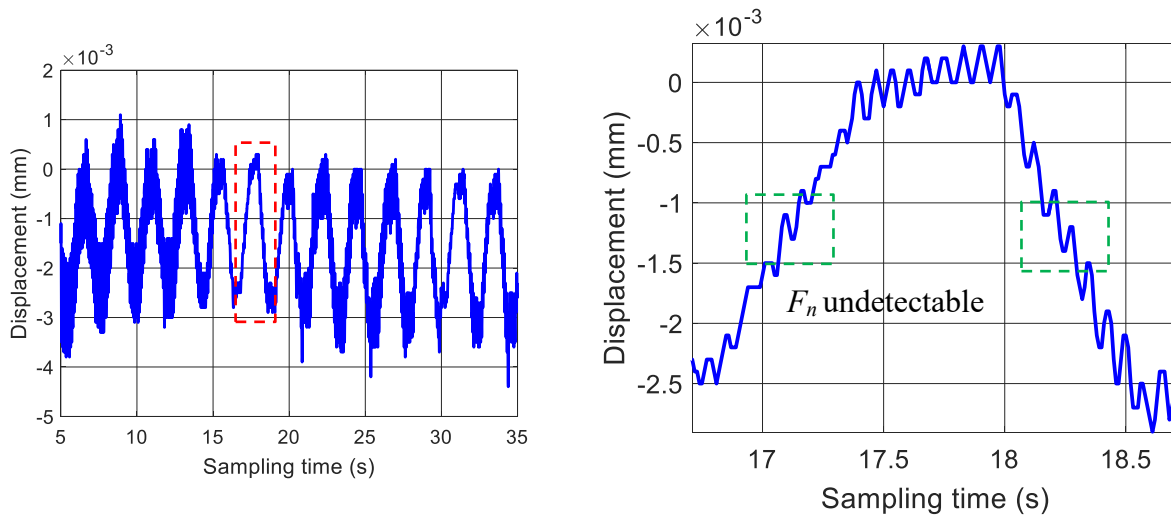


Figure 4.15: Displacement vs time graph: $Q = 0.16$ ml/min, $t = 0.15$ mm, $d_i = 0.25$ mm. F_n is undetectable, likely in the μN scale.

The normal force results, F_n , for all 54 process parameter combinations are shown in Figure 4.16. These results showed that F_n has a strong dependence on the process parameters, ranging from undetectable (< 0.1 mN) where the nozzle does not contact or come in close compression with the deposited silicone to 1.21 mN where significant compression takes place ($d_i = 0.41$, $t = 0.15$ and 0.10 mm, $Q = 0.4$ ml/min).

A key observation is that F_n was undetectable if the nozzle was not contacting the extruded silicone bead. However, the nozzle does not necessarily have to physically contact the extruded silicone for a jump in F_n to occur. An example of this is shown in the following process parameters: $d_i = 0.25$ mm, $t = 0.15$ mm, and $Q = 0.22$ ml/min. From Figure 4.13a, we observe that the nozzle does not contact the extruded silicone bead with those parameters (although it

comes very close). However, in Figure 4.16, a distinct increase in F_n was observed at this parameter set. This indicates that the nozzle does not necessarily need to contact the extruded silicone bead to create a detectable mN-scale F_n . In general, as Q is increased further, the degree to which the nozzle contacts the extruded silicone increases, causing an increase in F_n . Based on these results, F_{nn} is the dominating normal force component.

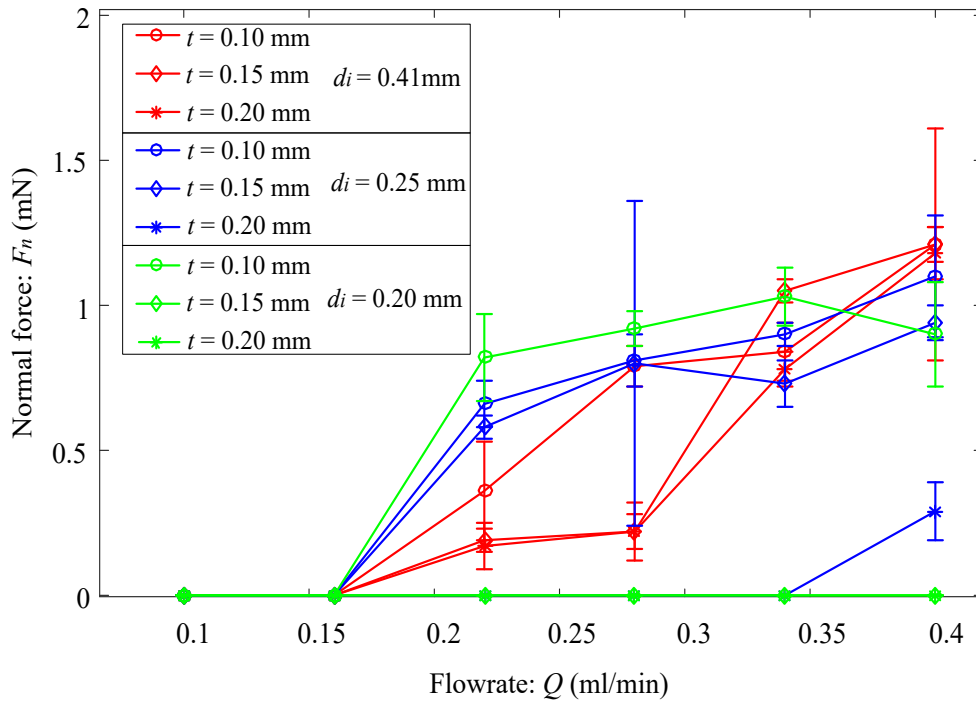


Figure 4.16: The average and standard deviation of F_n for three nozzles ($d_i = 0.41, 0.25,$ and 0.20 mm) at three layer heights ($t = 0.20, 0.15,$ and 0.10 mm).

4.4.4. Comparison of Results

Experimentally measured F_t and F_n show similarities and differences. As the nozzle tip begins contacting the extruded silicone, there is a significant increase in both F_t and F_n . Based on this we conclude that forces due to the nozzle tip contacting the extruded silicone, F_{tn} and F_{nn} , are much larger than the other force components caused by the extrusion-based AM process. We also observed that once the nozzle begins contacting the extruded silicone, F_{tn} and F_{nn} increase as Q increases. A slight difference in the behavior of F_{tn} and F_{nn} is that F_{nn} tends to onset before F_{tn} in certain scenarios since the nozzle is able to influence the normal compression even before it physically drags through the extruded silicone bead. This is observed in the spikes at three

process parameter combinations: (1) $Q = 0.22$ ml/min, $t = 0.15$ mm, $d_i = 0.25$ mm, (2) $Q = 0.22$ ml/min, $t = 0.10$ mm, $d_i = 0.20$ mm, and (3) $Q = 0.40$ ml/min, $t = 0.20$ mm, $d_i = 0.25$ mm, where the ratio of F_n to F_t quickly jumps and then flattens out, Figure 4.17.

A difference between the F_t and F_n measurements, assuming the nozzle is contacting the extruded silicone, is that a larger d_i creates a larger F_t and conversely creates a smaller F_n (all else equal), as shown in Figure 4.17.

We hypothesize that since a larger nozzle size has a greater bottom surface area, it has a greater tendency to flatten the top surface of the extruded silicone bead, creating a larger F_t than a small nozzle.

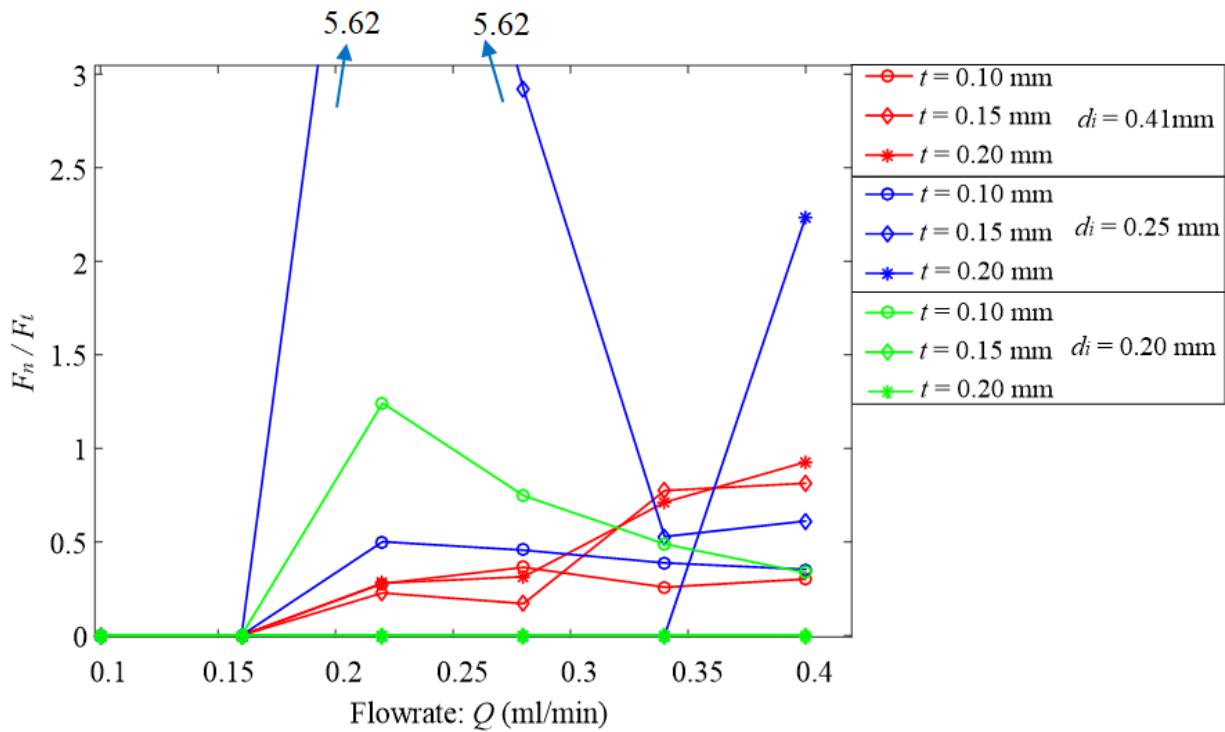


Figure 4.17: The ratio of F_n to F_t . A larger nozzle size generates a larger F_t than a smaller nozzle when the nozzle is sufficiently close or contacts the extruded silicone bead.

4.5 Conclusions

The tangential and normal forces imparted by the extrusion-based AM of silicone were experimentally determined for a variety of process parameter combinations. A CFD model was

also created and compared to the experimental results, as summarized in Appendix A. Experimental results showed that the F_t has a strong dependence on the process parameters, ranging from 0.03 mN ($Q = 0.10$ ml/min, $d_i = 0.25$ mm, $t = 0.20$ mm) to 4.01 mN ($Q = 0.40$ ml/min, $d_i = 0.41$ mm and $t = 0.10$ mm). Through high-speed camera footage and cross-section analysis, it was determined that F_m (tangential force caused by nozzle movement through the deposited silicone) is the dominating force component, causing an order of magnitude increase in F_t when present.

Experimental results showed that F_n also has a strong dependence on the process parameters, ranging from undetectable (< 0.1 mN) where the nozzle does not contact or come in close compression with the deposited silicone to 1.21 mN where significant compression takes place ($d_i = 0.41$, $t = 0.15$ and 0.10 mm, $Q = 0.4$ ml/min). Based on fluids theory, we predicted that F_{nd} (the normal force caused by deposited silicone decelerating) and F_{ng} (normal force due to the weight of the deposited silicone) provide μ N scale forces meaning that F_m (the normal force caused by the nozzle interaction with the silicone deposit layer) is the dominating force component causing an order of magnitude increase in F_n when present.

The CFD model simulated a single layer of silicone extrusion with a high degree of nozzle impact with the extruded silicone bead. In this model, $F_t = 0.21$ mN while $F_n = 4.5$ mN and slowly increased due to the weight of the deposited silicone, F_{ng} . While the CFD and experimental results match only at a few specific process conditions, they do predict similar force magnitudes given a similar extrusion scenario (nozzle impacting the extruded silicone).

Based on these findings, to reduce F_t and F_n in extrusion-based AM, it is recommended to select process parameters where the nozzle tip does not drag through the deposited silicone. By reducing these forces, it is possible to reduce the deflection of a soft AM silicone part and enable a greater level of design freedom. Even though these experiments were performed using one type of silicone, it is expected that similar findings will exist with other silicones and soft materials in extrusion-based AM.

Future work aims to expand the CFD model capability and study how force reduction and process parameter selection can enable to creation of tall, thick and thin-walled structures with high accuracy and mechanical strength.

CHAPTER 5

EXTRUSION-BASED SILICONE ADDITIVE MANUFACTURING GUIDELINES

5.1 Introduction

This dissertation presents several methods and techniques to be utilized during common printing scenarios of the extrusion-based silicone AM process. Three common scenarios are solid sections, support-less bridged sections, and tall/thin walled structures. From the findings of Chapters 2-4, it is observed that there is not necessarily one set of process parameters that is ideal for all printing scenarios. This section summarizes the key process parameter insights discovered in Chapters 2-4 and applies them to the manufacturing of a hollow silicone hand.

5.2 Solid Base Section

Since a solid base section is a wide and stable structure close to the build plate, as shown in the example of the base of the hand in Figure 5.1, it is highly resistant to deformation due to extrusion forces. Therefore, extrusion forces explored in Chapter 4 will not play a significant role and are not a main driving factor in process parameter selection for this region. Instead, the main driving factor is extrusion bead uniformity and surface roughness, Chapter 2, Section 2.3, Figure 2.4. From Chapter 2, it is observed that extrusion bead uniformity and surface roughness are dependent on five key process parameters: Compression factor X , adjacent line spacing c , Material flowrate Q , layer height t , and nozzle speed v . The governing equation for these variables is found in Eq. (2.2). This equation has several limitations. First, the variable limits are unknown and will be dependent on the flow properties of the extruded material; a higher viscosity material will be less likely to deform than a lower viscosity material. The suggested order of determining the process parameters in Eq. (2.2) are:

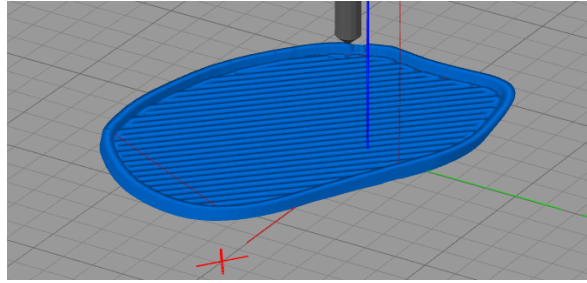


Figure 5.1: Example for printing of a solid base section of the hand.

- **Compression Factor, X :** Since a solid, voidless section is desired, X should be set at ≥ 1 (Section 2.4). A higher value of X will provide greater compression of silicone but at the potential cost of over extrusion.
- **Adjacent Line Spacing, c :** It is expected that the extruded material will swell as it leaves the nozzle by a factor of 1.05 to 1.3 [45,46]. By minimizing the required deformation of the extruded material, the chances of a voidless solid cross section are increased. Based on this, a line spacing c that is 1.05 to 1.3 times the nozzle diameter d_i is a good starting point. Since the silicone is liquid and can be compressed or stretched, other c values that are above or below the expected swollen value are certainly possible but may not be ideal for voidless printing. However, these scenarios can be useful in minimizing the deflection of tall and thin wall areas and will be discussed later.
- **Layer Height, t :** Layer height t is the next value to determine. Similar to other extrusion-based AM methods, a lower t will lead to increased print time and typically improved surface finish. However, as t is decreased, the liquid material compression is increased. If the material compression is too great, the extruded silicone will tend to flow in front of the nozzle, Figure 4.2d, causing an over-extrusion scenario and a breakdown of Eq. 2.2 (some extruded material is now on the nozzle and not in the part). Similar to the compression factor, this limit is also dependent on the material viscosity and the subject of future studies. If the layer height is increased, the material compression will be reduced along with print time. However, the surface roughness will tend to increase making it more difficult to eliminate internal voids (Figure 2.4).
- **Nozzle Speed, v , and Flowrate, Q :** The nozzle speed v was not subject to variation in this study (held constant at $v = 20$ mm/s). Since all of the other values in Eq. (2.2) have been

determined, the ratio of Q/v scales linearly. However, this linear relationship doesn't take into account the swell ratio's dependence on Q . As Q/v is increased, larger pressures will exist inside the nozzle. This may lead to variations in the expansion of silicone as it leaves the nozzle opening, entering atmospheric pressure. Increasing the ratio of Q/v will also increase the downward momentum of the extruded silicone, causing larger deformations of previous layers. This again will be dependent on the material flow properties, a subject for future study, and could be compensated for by adjusting c , t , and X .

- **Infill:** From Chapter 3, it was found that infill direction does not play a significant role in tensile strength so long as voids were less than approximately 500 μm and circular in shape. If elongated voids exist, it is expected that tensile strength will be reduced, especially perpendicular to that direction. It is also important to minimize jagged edge geometry, internal tangency voids, and surface roughness. These should be the driving factors for selecting an infill pattern.
- **Outlines:** From Section 2.5, it is shown that a compression factor $X = 1.02$ is not sufficient to eliminate internal voids between adjacent lines at the outer ends of a part. In this region it is recommended to slightly increase X ($X = 1.16$ in this study) thereby making $c_{edge} < c$ to eliminate edge voids. This required increase in X (decrease in adjacent line spacing) will again depend on the silicone material properties and part geometry. From Section 2.6, it was discovered that using at least 4 outlines between the edge of the part and the infill provided a sufficient deformation buffer to maintain enough accuracy at the outer edge to facilitate part bridging.

5.3 Support-less Bridging

Beyond the solid base structure, another common AM scenario is the support-less bridging, Section 2.6. This bridge can be connected to a solid section, as seen in Figure 2.10 and Figure 2.11, or be a thin wall, as shown in Figure 5.2, depending on the desired wall thickness. In Table 2.2, a parametric stair stepping approach was utilized, adjusting parameters in Eq. (2.2), to bridge a solid rectangular section with a resulting overhang angle of $\sim 45\%$. From Chapter 4, it was discovered that an additional factor should be considered, part deflection, to further drive the choice of process parameters.

The main cause of part deflection, neglecting external forces, is the tangential forces F_t and normal forces F_n caused by the extrusion-based process. If too much deformation of the part occurs, surface finish and part accuracy could be deteriorated and may even cause print failure. From Chapter 4, it was discovered that F_t and F_n are strongly dependent on the process parameters c , Q , and t . Furthermore, based on root causes of these forces, it is also expected that increasing v and X will increase F_t and F_n although they were not specifically studied in this dissertation.

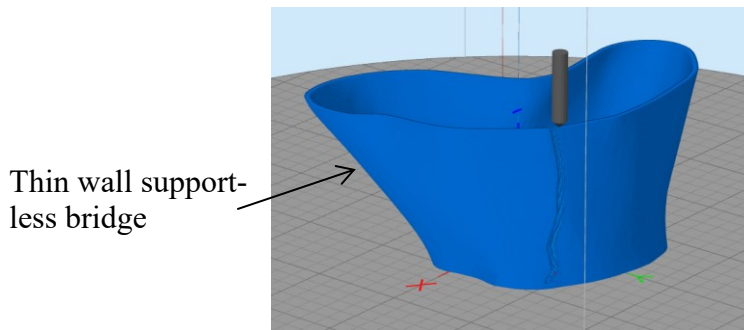


Figure 5.2: Toolpath of thin wall support-less bridging.

For areas requiring support-less bridging, it is important to minimize the deflection ratio of force acting to deflect the structure downward, F_n , with the structure's resistance to deformation. In this scenario, to determine the structure's resistance to deformation, it is assumed that the cross section approximates a solid rectangular beam deflecting along its long axis.

According to the second moment of area for a rectangular beam, $I = \frac{db^3}{12}$, where d is the wall thickness and b is the length of the wall, the beam's resistance to deflection is linearly dependent on the wall thickness, W_t . Wall thickness $W_t = cn$, where n is the number of lines that make up the thin wall. For a single line wall, c is approximated by setting $X = 1$ in Eq. (2.2) and $n = 1$. Utilizing the F_n data obtained in Section 4.4.3 and dividing by W_t to obtain the deflection ratio, the following graph is obtained, Figure 5.3.

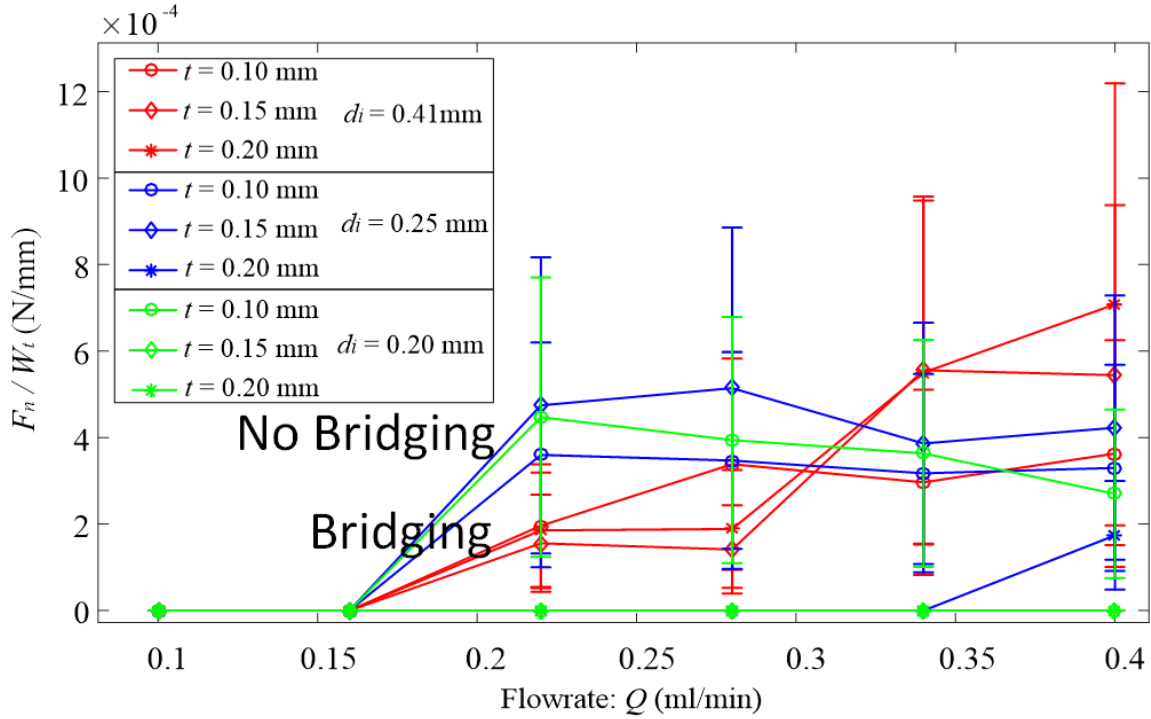


Figure 5.3: Deflection ratio F_n/W_t at various Q . A larger nozzle d_i has a greater tendency for unsupported bridging.

Although there is a large amount of variability in this graph, a general trend can be observed. Ignoring the process parameter combinations where $F_n = 0$ (forces undetectable via the measurement methods deployed in Chapter 4), Figure 5.3 shows that the larger nozzle size d_i has a lower and more favorable deflection ratio F_n/W_t than the nozzle with smaller d_i (all else equal). These findings were validated at a flowrate $Q = 0.22$ ml/min, layer height $t = 0.10$ mm, and $c = 1.83$ mm where $d_i = 0.41$ mm had a greater bridging ability than $d_i = 0.20$ mm.

5.4 Tall/Thin Walled Structures

Tall and thin walled silicone structures are easily deformed by forces caused during the extrusion-based AM process, Chapter 4. To optimize the process parameters for these structure types, a deflection ratio approach is again utilized but with different criteria from that of support-less bridging, Section 5.3. Since this type of structure is more greatly affected by tangential forces than normal forces, the F_t data measured in Section 4.4.2 is instead used in the numerator

of the deflection ratio. To determine the denominator of the deflection ratio, the tall and thin walled structure is approximated as a hollow rectangular prism. The second moment of area for a hollow rectangular prism is $I = \frac{EF^3 - ef^3}{12}$ where E and F are the outer dimensions of the rectangular prism and e and f are the inner dimensions of the rectangular prism. For validation purposes, a 10 mm \times 10 mm single wall square tower was assumed, Figure 5.4a, where $E = F = 10 + c/2$ mm and $e = f = 10 - c/2$ mm and c is calculated by assuming $X = 1$ in Eq. (2.2). The graph of this relationship, along with the maximum build height of the finger approximating towers, is shown in Figure 5.4b.

From Figure 5.4b, it is observed that deflection ratio criteria for F_t and a hollow rectangular prism correlates well to the maximum tower height for all tested values, as the deflection ratio is reduced the maximum tower height is increased, with the exception of $d_i = 0.41$ mm, $t = 0.10$ mm, and $Q = 0.22$ and 0.40 ml/min. This poor correlation is believed to exist due to a different failure mechanism than that of the assumed rectangular prism bending. An example of a failed tower due to rectangular prism bending is shown in Figure 5.5a. In this example, as the height of the tower grew, the tower deflection moment increased due to F_t until it no longer provided a stable platform for printing. The non-correlating towers did not fail due to rectangular prism bending, but rather due to an over extrusion and buildup of material, Figure 5.5b and c. Here the nozzle continually dragged the extruded silicone until the top of the tower closed off and could no longer provide a suitable printing surface. To predict the maximum tower build heights in this over extrusion scenario, a new deflection ratio assuming a linear correlation to the line width W_t was imposed (deflection resistance along the long axis of a solid rectangular beam), Figure 5.6. This appears to better correlate the maximum tower heights for flowrates $Q = 0.22$ ml/min and above at the t and d_i values tested.

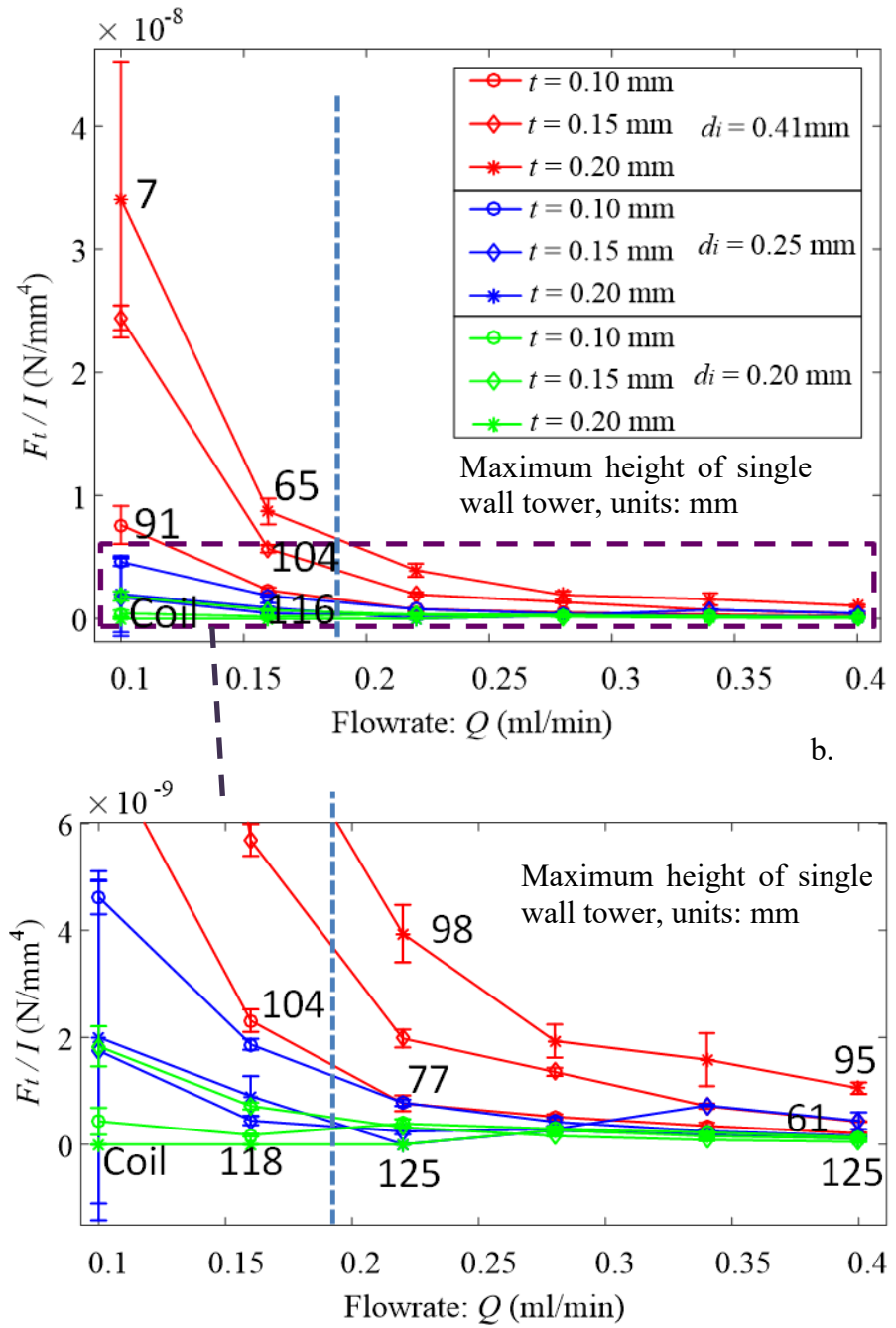
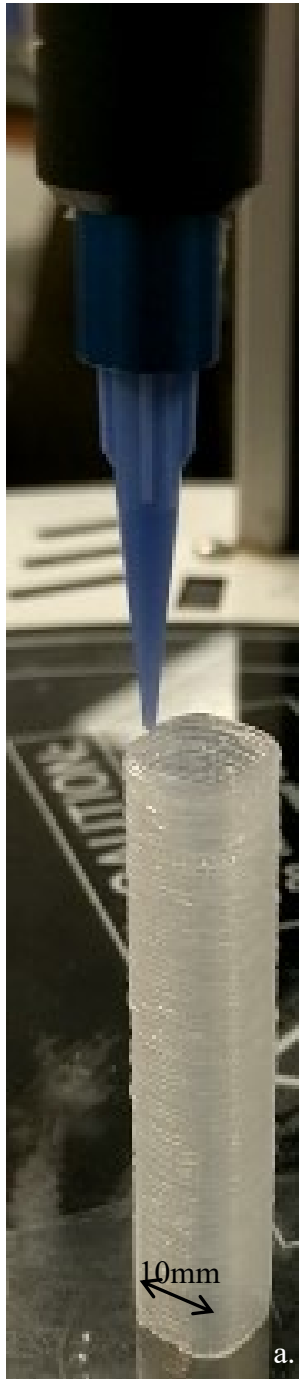


Figure 5.4: (a) A 10 × 10 mm single wall tower used to validate the deflection ratio assumption, F_t/I . (b) The graph of deflection ratio F_t/I at various Q with the maximum tower height before failure denoted on the graph (unit: mm). Coil denotes a process parameter combination where a rope coiling phenomenon was observed.

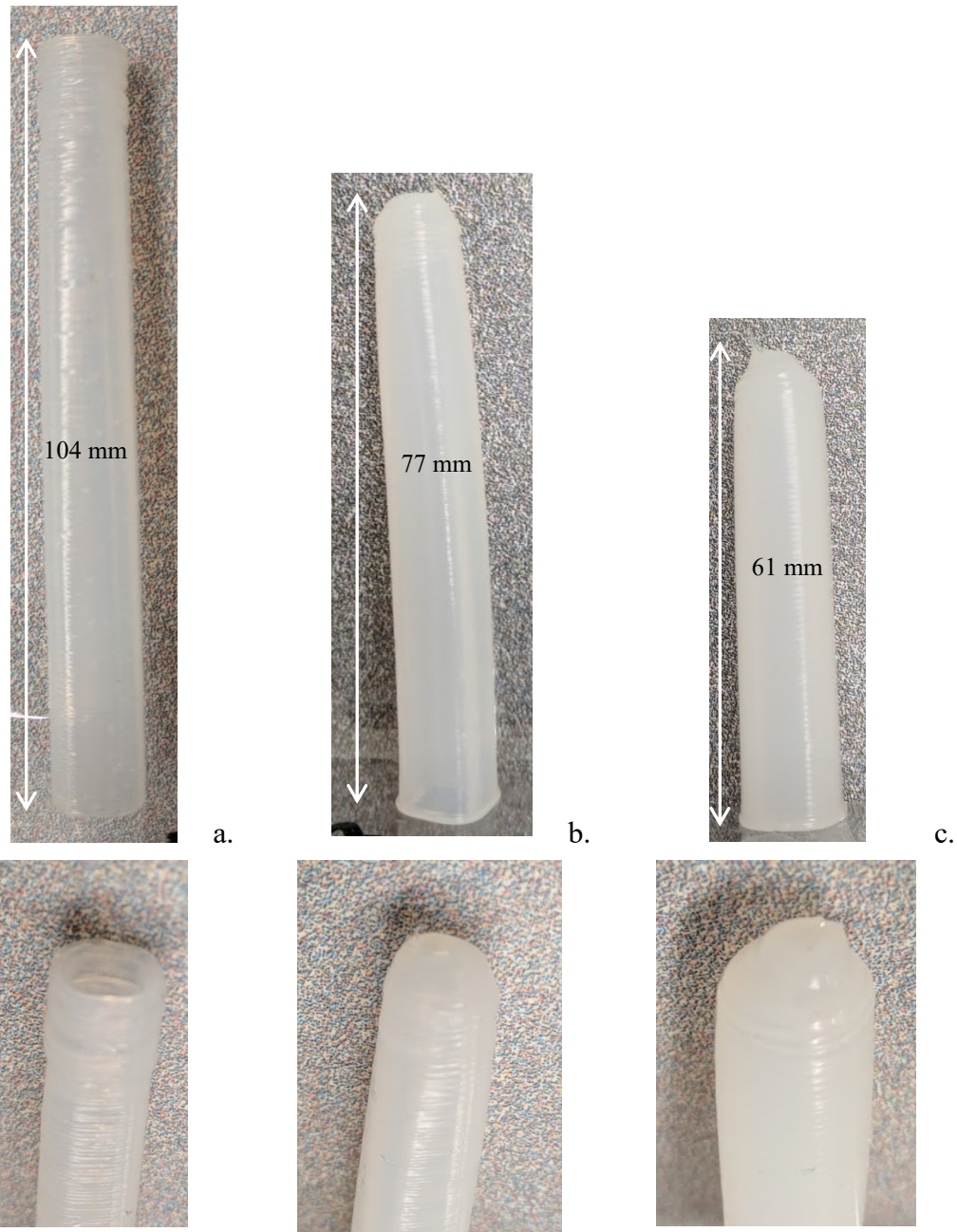


Figure 5.5: Side view (top) and top view (bottom) of tall/thin wall towers with $d_i = 0.41$ mm, $t = 0.10$ mm, and $Q =$ (a) 0.16, (b) 0.22, and (c) 0.40 ml/min.

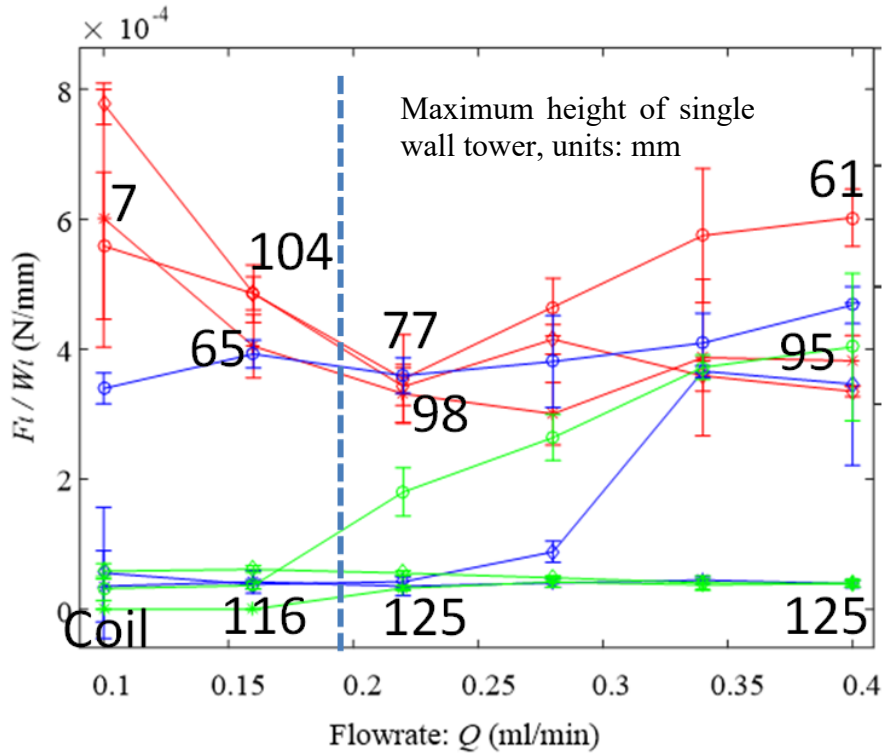


Figure 5.6: Deflection ratio F_t/W_t at various Q with the maximum tower height before failure denoted on the graph (unit: mm).

From these results, a smaller nozzle d_i has a more favorable force deflection ratio than a larger nozzle d_i . As d_i becomes smaller, the force deflection ratio also becomes less dependent on Q and t . Based on these results, when selecting the process parameters for tall and thin structures, it is best to minimize d_i . When utilizing a small d_i , other parameters such as t and Q can be selected based on the desired surface finish and wall thickness, Eq. (2.2).

5.5 Hollow Silicone AM Hand Example

The findings described in Sections 5.2 - 5.4 to select optimal process parameter for solid sections, support-less bridged sections, and tall/thin walled structures were utilized for the creation of a hollow hand produced through extrusion-based silicone AM, Figure 5.7.

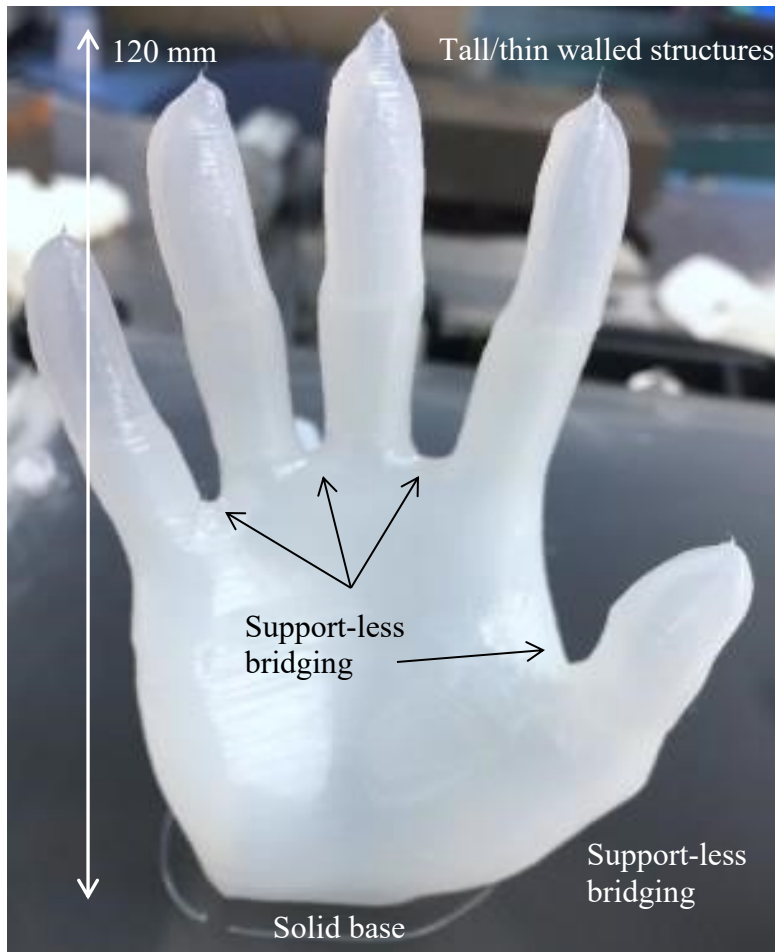


Figure 5.7: Complete hollow hand produced through extrusion-based silicone AM.

The base of the hand approximates a solid base section, the angled base of the thumb and in-between the finger joints approximates support-less bridges sections, and the rest of the hand (especially the fingers) approximates tall/thin walled structures.

5.6 Conclusions

There are many different types of printing scenarios in extrusion-based AM of silicone and each scenario has its own set of process optimization parameters. Shown from the findings of this dissertation, the optimal process parameters for each scenario may be drastically different from another scenario. For example, in unsupported bridging a larger nozzle d_i is desired

whereas to minimize the deflection of tall tower-like structures a smaller nozzle d_i is desired. By understanding the printing scenario and its corresponding key process parameters, it is possible greatly expand the potential design space for soft parts created through extrusion-based AM.

CHAPTER 6

CONCLUSIONS AND FUTURE WORK

6.1 Conclusions and Major Contributions

This dissertation studied the extrusion-based additive manufacturing of moisture-cured silicone elastomer parts. Experiments were conducted to observe the deformation of the silicone layers to achieve a voidless mesostructure. Techniques were proposed to enable the creation of thin-walled pneumatic actuators. Tensile tests were performed to evaluate process parameter and void effects on the AM part strength and failure modes. The tangential and normal forces generated by the extrusion-based AM process were measured and modeled.

Three major achievements of this dissertation are:

(1) *The extrusion-based additive manufacturing of moisture-cured silicone elastomer with minimal void for pneumatic actuators*: A methodology for identifying process parameters to fabricate voidless solid and thin-wall structures using extrusion-based AM of moisture-cured silicone was presented. A geometric theory was proposed and validated, providing a guideline for predicting process parameters which can enable a “voidless” mesostructure. This approach was not previously used in process parameter selection for extrusion-based methods and enables the fabrication of thin-walled pneumatic actuators with high elongation and fatigue life.

(2) *Void and tensile properties in extrusion-based additive manufacturing of moisture-cured silicone elastomer*: The tensile strength and strain properties as well as failure modes in silicone dumbbell specimens fabricated by extrusion-based additive manufacturing were investigated. Effects of process parameters, specifically the infill direction (0° , $\pm 45^\circ$, and 90° relative to the tensile direction) and adjacent line spacing on the void formation and maximum tensile strength were studied and compared to the baseline of stamped silicone specimens. To

maximize the tensile strength of silicone parts made by extrusion-based AM, it is important to select process parameters which minimize the elongated voids, infill tangency voids, and surface edges. If these conditions can be achieved, the infill direction does not play a significant role in the tensile strength of a part. This is a unique demonstration of isotropic part creation using extrusion-based AM.

(3) *Measurement and Modeling of Forces in Extrusion-based Additive Manufacturing of Moisture-Cured Silicone Elastomer*: The tangential and normal forces imparted by the extrusion-based AM of silicone were experimentally determined for a variety of process parameter combinations. A CFD model was also created (Appendix A). Results showed that the tangential and normal forces are strongly dependent on the process parameters and nozzle tip interaction with the extruded silicone. By controlling this interaction, it is possible to reduce the deformation of a soft silicone part during the AM process, enabling a significant increase in part height and a greater level of design freedom. This is the first time the forces during an extrusion-based AM of silicone process have been measured.

The original discoveries and key conclusions of this dissertation are:

- (1) The deposition of material can compress and deform previously extruded silicone layers.
- (2) The resultant line-width can be predicted and utilized to achieve a voidless mesostructure.
- (3) Different degrees of compression can be created based on the process parameters used. These different compression factors are optimally utilized for different AM scenarios. For example, the amount of compression needed in initial layers is less than the amount of compression needed at the top layers to achieve a voidless section. Similarly, the amount of compression needed in a solid section is less than that of a thin walled section.
- (4) A stair-stepping technique is presented to allow for horizontal bridging of a material which is unable to self-support (support-less printing), enabling the creation of soft pneumatic actuators and hollow structures.
- (5) By utilizing process parameters which create a voidless or near-voidless mesostructure (so long as the voids are circular), isotropic parts can be created with average tensile strength of approximately 90% to a non-AM baseline specimen.

- (6) The tangential and normal forces experienced by the extrusion-based AM process can have a significant impact on the ability to build tall silicone parts. By adopting certain process parameters, particularly those where the nozzle does not impact the extruded silicone bead, it is possible to reduce these tangential and normal forces by orders of magnitude.

These findings lay the groundwork for the extrusion-based additive manufacturing (AM) of silicone and other soft materials. By utilizing these results, control methods can be developed which will enable the creation of high quality, custom silicone parts capable of high strength and elongations.

6.2 Future Work

The methodologies and models proposed in this dissertation could be further improved and extended in the following directions:

- (1) A predictive model could be developed based on the findings of this study to automate the process parameter selection based on the AM scenario. This could be implemented during the tool path creation process, during the AM process through closed-loop monitoring techniques, or a combination thereof.
- (2) A dynamically changing nozzle diameter could be developed so the process parameters can be further optimized if multiple different printing scenarios are encountered in the same layer/part.
- (3) Validation could be performed on other types of silicones and soft materials to determine the limits of the proposed models. With further model validation, these results can be extended to predict the ideal process parameter settings based solely on the material properties of the extruded material.
- (4) Fluid flow within the nozzle during the extrusion start/stop can be modeled and compensated for within the AM process to further improve the AM parts.
- (5) Selective material cure methods (such as heat and UV cure) can be studied to improve part stability during AM while maintaining high interlayer bonding strength. Specifically, lower layers could be selectively cured to increase the stiffness of the printed structure, reducing part deformation during the AM process while the upper most layer could be left uncured to maximize interlayer

bonding. These varying cure kinetics can also impact previous layer deformations and may require additional compensation techniques to achieve voidless mesostructures and minimize the forces from the AM process

- (6) Conductive materials can be selectively embedded within the silicone parts, creating unique, flexible, and wearable 2D and 3D sensors.

APPENDIX A

CFD Modeling

Appendix 4A details the initial CFD modeling setup and predicted F_n and F_t for the extrusion-based AM of silicone.

A.1. Silicone Extrusion CFD Model

The silicone deposition process for $Q = 0.10$ and 0.22 ml/min, $t = 0.10$ mm, and $d_i = 0.2$ mm was modeled by simulating the multiphase flow (silicone and air) around the nozzle as shown in Figure A1a and b. In the mesh, the nozzle has an outer diameter of 0.44 mm. The computing domain is a $5 \times 2 \times 0.2$ mm box. The silicone is a non-Newtonian fluid and the shear thinning effect is described by the Carreau model:

$$\mu_{\text{silicone}} = \mu_{\infty} + (\mu_0 - \mu_{\infty})(1 + (\lambda\dot{\gamma})^2)^{\frac{n-1}{2}} \quad (\text{A1})$$

where μ_{silicone} is the silicone viscosity, μ_{∞} is viscosity at infinite shear rate, μ_0 is viscosity at zero shear rate, λ is relaxation time, $\dot{\gamma}$ is shear rate, and n is power index. In this study, $\mu_0 = 62.5$ Pa · s, $\mu_{\infty} = 0$, $\lambda = 0.0173$ s, and $n = 0.5$ [15]. The silicone has a density of 1040 kg/m³ [36] and surface tension of 0.02 N/m² [48].

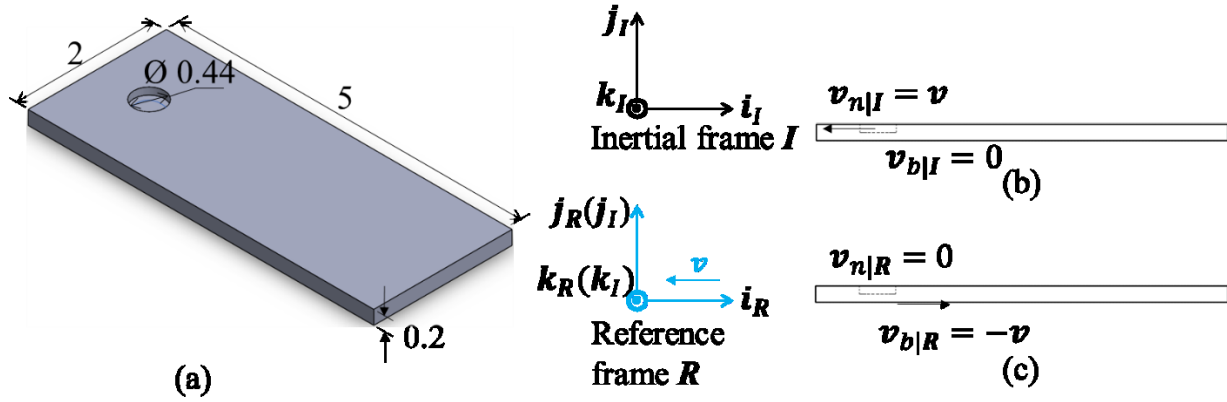


Figure A1: Silicone deposition CFD modeling: (a) fluid domain, (b) front view an inertial frame, and (c) in a moving reference frame. (unit: mm)

A.2 Governing equations and boundary condition in a moving reference frame

A moving reference frame, R , was introduced, as shown in Figure A1c, to simulate the relative movement between the nozzle and build plate without using dynamic mesh. Relative to the inertial frame I , R has a velocity vector of the nozzle \mathbf{v} . By assuming an isothermal and incompressible flow, the deposition process is governed by mass continuity and momentum conservation for both the silicone and air.

The mass continuity equation is:

$$\nabla \cdot \mathbf{u} = 0 \quad (\text{A2})$$

where \mathbf{u} is the velocity vector of silicone and air observed in R .

The momentum equation is:

$$\rho \frac{\partial \mathbf{u}}{\partial t} + \rho(\mathbf{u} + \mathbf{v}) \cdot \nabla \mathbf{u} = -\nabla p + \nabla \cdot [\mu(\nabla \mathbf{u} + \nabla \mathbf{u}^T)] + \rho \mathbf{g} + \mathbf{f} \quad (\text{A3})$$

where ρ is the density, t is the time, p is the static pressure, \mathbf{g} is the vector of gravity, and \mathbf{f} is the vector of body force other than gravity.

To track the interface between silicone and air, the volume of fluid (VOF) method was adopted. VOF assumes the silicone and air are immiscible. VOF resolves the interface by solving a continuity equation for the volume fraction of silicone, α :

$$\frac{\partial \alpha}{\partial t} + \nabla \cdot \alpha \mathbf{u}_{\text{silicone}} = 0 \quad (\text{A4})$$

where $\mathbf{u}_{\text{silicone}}$ is the velocity vector of silicone. The value of α ranges from 0 to 1, where $\alpha = 0$ means pure air, $\alpha = 1$ means pure silicone and $0 < \alpha < 1$ means a mixture of silicone and air. For each cell in the flow domain, the density and viscosity are computed as:

$$\rho = (1 - \alpha)\rho_{\text{air}} + \alpha\rho_{\text{silicone}} \quad (\text{A5})$$

$$\mu = (1 - \alpha)\mu_{\text{air}} + \alpha\mu_{\text{silicone}} \quad (\text{A6})$$

where ρ_{air} and ρ_{silicone} are the density of air and silicone, respectively.

The boundary conditions change while the reference frame is moved from I to R, as shown in Figure A1b and c. In R, the nozzle has a velocity $\mathbf{v}_{n|R} = 0$. The build plate has a velocity $\mathbf{v}_{b|R} = -\mathbf{v}$. Both the nozzle and build plate assume the non-slip condition. For the inlet of the nozzle, a silicone speed of u_{inlet} is imposed. By assuming the silicone flow is fully developed with the parabolic profile, the distribution of u_{inlet} is:

$$u_{\text{inlet}} = \frac{8Q}{\pi d_i^2} \left(1 - \frac{4r^2}{d_i^2}\right) \quad (\text{A7})$$

where r is the distance from the center of the nozzle. All other boundary conditions are set as outlet with zero static gage pressure. Although the experimental forces were measured after at least two layers for deposition, for simplicity, the extruded silicone in the CFD model is deposited directly on a flat build plate.

A.3 Numerical method

The CFD software, Fluent (v16.2, ANSYS, Canonsburg, Pennsylvania), was used to solve Eqns. (A2)-(A7). The estimated Reynolds number for air is $Re_{\text{air}} = \frac{\rho_{\text{air}} v L}{\mu_{\text{air}}} = 6.8$ and for silicone it is $Re_{\text{silicone}} = \frac{\rho_{\text{silicone}} v L}{\mu_{\text{silicone}}} = 0.002$, where L is the build plate length 5 mm. Both Re_{air} and Re_{silicone} are much smaller than the critical value for turbulent flow, 5×10^5 , meaning the flow is laminar. The second order scheme was applied to discretize the momentum. Semi-implicit pressure linked equations were utilized to handle the velocity-pressure coupling. The

convergence criterion was 10^{-3} for the residuals of continuity and 3 velocity components. A variable time step method was used to limit the maximum Courant number to 0.5 to maintain the stability and accuracy of the solution. At the beginning of the simulation, the entire flow domain was initialized with $\alpha = 0$.

The mesh was generated using Pointwise (v17.3, Pointwise, Fort Worth, Texas) with hexahedral cells. Hexahedral cell was chosen over tetrahedral or prism cell due to reduce error caused by numerical diffusion. Figure A2 shows the mesh with 246,000 cells.

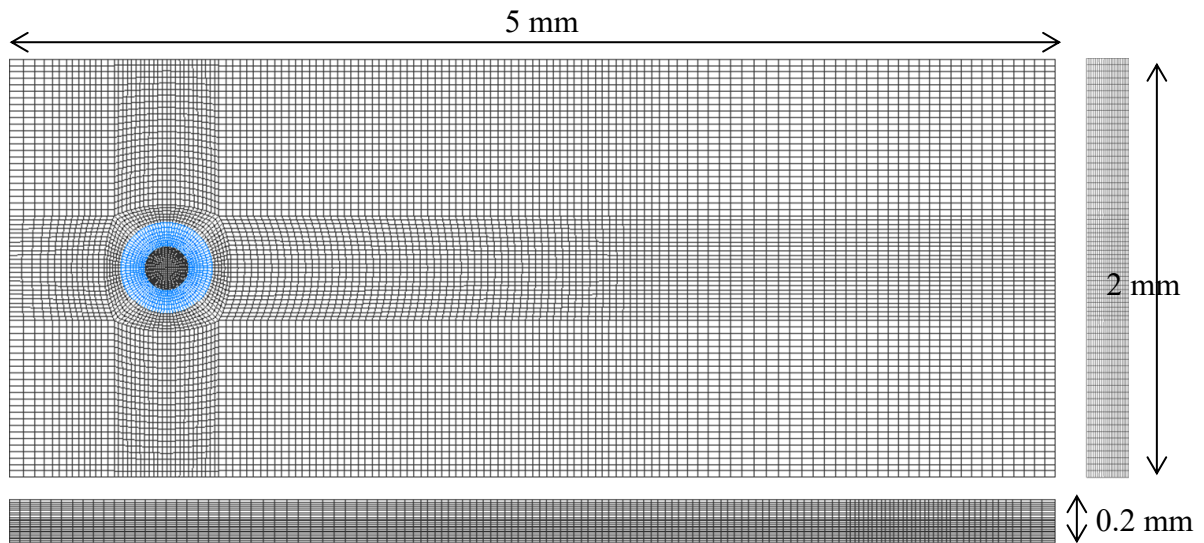


Figure A2: Top, front, and side view of the mesh.

A.4. CFD Results

The results of the CFD modeled volume fraction of silicone, α , for $d_i = 0.20$ mm, $t = 0.10$ mm, $v = 20$ mm/s, and $Q = 0.10$ ml/min and 0.22 ml/min, with single layer deposition on a rigid build plate are shown in Figure A3. After extrusion from the nozzle, silicone is compressed between the nozzle and build plate, as shown in Figure 4.2c and d. This compression has three effects on the deposition of the silicone: (1) the deposited silicone bead expands and the bead width is larger than d_i ; the bead width for $Q = 0.22$ ml/min is larger than that for $Q = 0.10$ ml/min, (2) some silicone is pushed out in front of the nozzle opening, and (3) for $Q = 0.10$ ml/min, the nozzle tip face remains in contact with the silicone bead during deposition, creating a flat top surface on the deposited silicone; for $Q = 0.22$ ml/min, in addition to the nozzle tip face,

the side of the nozzle is also dragging through the deposited silicone. From the experimental results for $Q = 0.10$ ml/min, the nozzle was not expected to contact the silicone bead based on the given process parameters. However, since only the first layer was modeled, the silicone was not able to deform the previous layers below, causing an artificial over extrusion scenario.

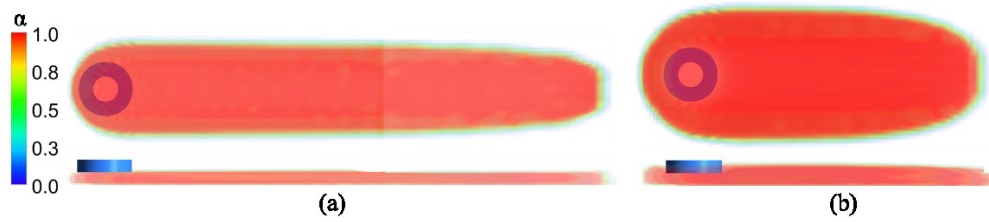


Figure A3: Top view and side view of CFD result of silicone fluid deposited on a rigid build plate with (a) $Q = 0.10$ ml/min and (b) $Q = 0.22$ ml/min. The nozzle is contacting the extruded silicone bead.

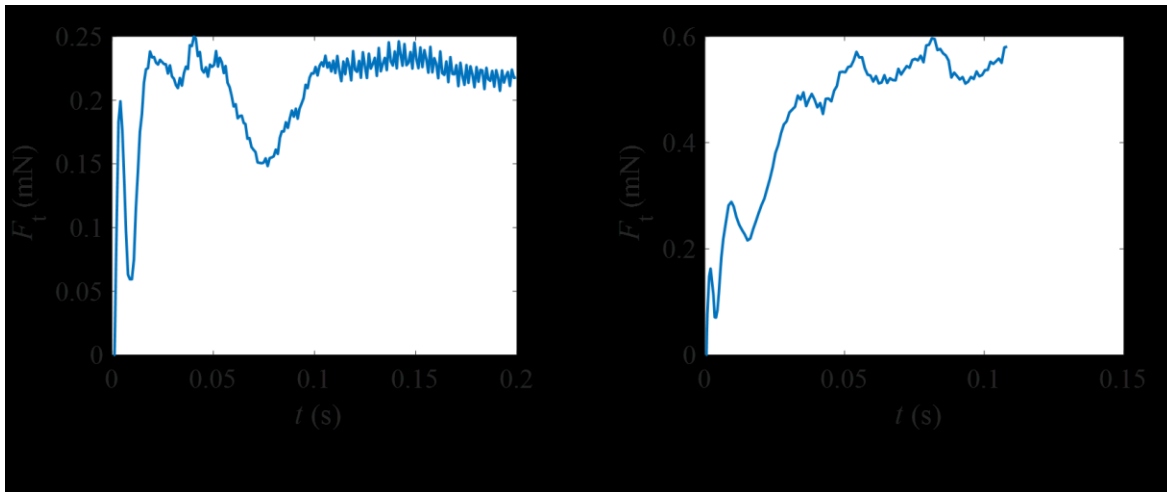


Figure A4: Predicted F_t on the rigid build plate from the CFD model for: (a) $Q = 0.10$ ml/min and (b) $Q = 0.22$ ml/min.

Figure A4 shows the predicted forces F_t on the build plate. As shown in Figure A4a, F_t fluctuates from 0 to about 0.15 s before the steady-state was established. F_t reaches a steady-state at about 0.21 mN. In Figure A4b, F_t increases from 0 to about 0.05 s and reaches a quasi-steady state with a small fluctuation and a mean value of about 0.55 mN. For $Q = 0.22$ ml/min, the modeled F_t (0.55 mN) correlates closely to the experimental F_t (0.66 mN). For $Q = 0.10$ ml/min, the modeled F_t (0.21 mN) does not correlate closely to the experimental F_t (0.05

mN). This poor correlation is expected due to the over extrusion scenario from only simulating the first layer. The match between CFD and experiment result for $Q = 0.22$ ml/min brings great confidence to the accuracy of both the experimental and CFD Results.

REFERENCES

- [1] T. Method-, Standard Terminology for Additive Manufacturing – General Principles –, i (2016) 1–9.
- [2] Smooth-On Durometer Shore Hardness Scale, (n.d.). <https://www.smooth-on.com/page/durometer-shore-hardness-scale/>.
- [3] A.N. Gent, On the Relation between Indentation Hardness and Young’s Modulus, Rubber Chem. Technol. 31 (1958) 896–906. doi:10.5254/1.3542351.
- [4] K. Larson, Can You Estimate Modulus From Durometer Hardness for Silicones?, 2016. http://www.dowcorning.com/content/publishedlit/11-3716-01_durometer-hardness-for-silicones.pdf (accessed May 31, 2017).
- [5] 3D Systems, DuraForm ® TPU Elastomer, 2016. 09-16 datasheet.
- [6] Stratasys, Stratasys PolyJet Materials Data Sheet, 2014. MSS_PJ_PJMaterialsDataSheet_EN_0815 datasheet.
- [7] Stratasys, Agilus30 Polyjet Rubber-like Material, 2017. MSS_PJ_Agilus30_0317a datasheet.
- [8] D.K. Patel, A.H. Sakhaei, M. Layani, B. Zhang, Q. Ge, S. Magdassi, Highly Stretchable and UV Curable Elastomers for Digital Light Processing Based 3D Printing, Adv. Mater. (2017) 1606000. doi:10.1002/adma.201606000.
- [9] B.N. Peele, T.J. Wallin, H. Zhao, R.F. Shepherd, 3D printing antagonistic systems of artificial muscle using projection stereolithography., Bioinspir. Biomim. 10 (2015) 55003. doi:10.1088/1748-3190/10/5/055003.
- [10] spot-A materials, Spot-E 10kg | Spot-A Materials, 2016. datasheet.
- [11] Carbon3D, CarbonResin EPU 40, 2016. DOC #103208 REV A datasheet.
- [12] NinjaTek, NinjaFlex ® 3D Printing Filament Flexible Polyurethane Material for FDM Printers, 2016. 2016_04_NF_MSPEC datasheet.
- [13] H.K. Yap, High-Force Soft Printable Pneumatics for Soft, 3 (2016) 144–158. doi:10.1089/soro.2016.0030.
- [14] Wacker Chemie AG, Solid and Liquid Silicone Rubber Material and Processing Guidelines, n.d. 6709_EN report.

- [15] Y. Jin, J. Plott, A.J. Shih, Extrusion-based additive manufacturing of the moisture-cured silicone elastomer, *Proc. Solid Free. Fabr. Symp.* (2015) 308–318. doi:10.1017/CBO9781107415324.004.
- [16] J. Plott, A.J. Shih, The Extrusion-based Additive Manufacturing of Moisture-Cured Silicone Elastomer with Minimal Void for Pneumatic Actuators, *Addit. Manuf.* (2017). Accepted.
- [17] Discov3ry Extruder: A Universal Paste Extruder For Your Desktop 3D Printer, (n.d.). <https://www.structur3d.io/discov3ry-products/discov3ry>.
- [18] Nordson EFD Performus Series Dispensers, (n.d.). <http://www.nordson.com/en/divisions/efd/products/fluid-dispensing-systems/performus-series-dispensers>.
- [19] preeflow by ViscoTec, (n.d.). <https://www.preeflow.com/media/Broschuere-preeflow-en-2017-digital-1.pdf>.
- [20] H.-H. Moretto, M. Schulze, G. Wagner, Silicones, *Ullmann's Encycl. Ind. Chem.* (2000). doi:10.1002/14356007.a24.
- [21] I.M. Koo, K. Jung, J.C. Koo, J. Do Nam, Y.K. Lee, H.R. Choi, Development of soft-actuator-based wearable tactile display, *IEEE Trans. Robot.* 24 (2008) 549–558. doi:10.1109/TRO.2008.921561.
- [22] R.K. Kramer, C. Majidi, R.J. Wood, Wearable tactile keypad with stretchable artificial skin, *Proc. - IEEE Int. Conf. Robot. Autom.* (2011) 1103–1107. doi:10.1109/ICRA.2011.5980082.
- [23] Y. Menguc, Y.L. Park, E. Martinez-Villalpando, P. Aubin, M. Zisook, L. Stirling, R.J. Wood, C.J. Walsh, Soft wearable motion sensing suit for lower limb biomechanics measurements, *Proc. - IEEE Int. Conf. Robot. Autom.* (2013) 5309–5316. doi:10.1109/ICRA.2013.6631337.
- [24] D. Rus, M.T. Tolley, Design, fabrication and control of soft robots, *Nature.* 521 (2015) 467–475. doi:10.1038/nature14543.
- [25] K.J. Cho, J.S. Koh, S. Kim, W.S. Chu, Y. Hong, S.H. Ahn, Review of manufacturing processes for soft biomimetic robots, *Int. J. Precis. Eng. Manuf.* 10 (2009) 171–181. doi:10.1007/s12541-009-0064-6.
- [26] H. Zhao, Y. Li, A. Elsamadisi, R. Shepherd, Scalable manufacturing of high force wearable soft actuators, *Extrem. Mech. Lett.* 3 (2015) 89–104. doi:10.1016/j.eml.2015.02.006.
- [27] E. Selbertinger, F. Achenbach, B. Pachaly, Method for producing silicone elastomer parts, *PCT/EP2015/075329*, 2014.

- [28] T. Fripp, N. Frewer, L. Green, Method and apparatus for additive manufacturing, US 2016/0263827, 2016.
- [29] ViscoTec, Dosing technology Dosing system eco-PEN450, n.d. V1.1 05/11 datasheet.
- [30] J.F. Rodriguez, J.P. Thomas, J.E. Renaud, Characterization of the mesostructure of fused-deposition acrylonitrile-butadiene-styrene materials, *Rapid Prototyp. J.* 6 (2000) 175–186. doi:10.1108/13552540010337056.
- [31] J.F. Rodriguez, J.P. Thomas, J.E. Renaud, Maximizing the strength of fused-deposition ABS plastic parts, *Solid Free. Fabr. Proceedings, Notre Dame, IN.* (1999) 335–342.
- [32] O.S. Es-Said, J. Foyos, R. Noorani, M. Mendelson, R. Marloth, B.A. Pregger, Effect of Layer Orientation on Mechanical Properties of Rapid Prototyped Samples, *Mater. Manuf. Process.* 15 (2000) 107–122. doi:10.1080/10426910008912976.
- [33] A. Bellini, S. Güçeri, Mechanical characterization of parts fabricated using fused deposition modeling, *Rapid Prototyp. J.* 9 (2003) 252–264. doi:10.1108/13552540310489631.
- [34] S.-H. Ahn, M. Montero, D. Odell, S. Roundy, P.K. Wright, Anisotropic material properties of fused deposition modeling ABS, *Rapid Prototyp. J.* 8 (2002) 248–257. doi:10.1108/13552540210441166.
- [35] O.A. Mohamed, S.H. Masood, J.L. Bhowmik, Optimization of fused deposition modeling process parameters: a review of current research and future prospects, *Addit. Manuf.* (2015) 42–53. doi:10.1007/s40436-014-0097-7.
- [36] D. Corning, Silicone Sealants Dow Corning® 737 Neutral Cure Sealant Clear, 2011. datasheet.
- [37] J. Comyn, F. De Buyl, N.E. Shephard, C. Subramaniam, Kinetics of cure, crosslink density and adhesion of water-reactive alkoxy silicone sealants, *Int. J. Adhes. Adhes.* 22 (2002) 385–393. doi:10.1016/S0143-7496(02)00019-2.
- [38] N. Westerhof, N. Stergiopoulos, M.I.M. Noble, Law of Laplace, in: *Snapshots Hemodynamics An Aid Clin. Res. Grad. Educ.*, Springer US, Boston, MA, 2010: pp. 45–48. doi:10.1007/978-1-4419-6363-5_9.
- [39] B. Mosadegh, P. Polygerinos, C. Keplinger, S. Wennstedt, R.F. Shepherd, U. Gupta, J. Shim, K. Bertoldi, C.J. Walsh, G.M. Whitesides, Pneumatic networks for soft robotics that actuate rapidly, *Adv. Funct. Mater.* 24 (2014) 2163–2170. doi:10.1002/adfm.201303288.
- [40] R.K. Chen, T.T. Lo, L. Chen, A.J. Shih, Nano-CT Characterization of Structural Voids and Air Bubbles in Fused Deposition Modeling for Additive Manufacturing, in: *Vol. 1 Process.*, ASME, 2015: p. V001T02A071. doi:10.1115/MSEC2015-9462.
- [41] ASTM, D412-06 Standard Test Methods for Vulcanized Rubber and Thermoplastic

- Elastomers–Tension, 2006. doi:10.1520/D0412-06AR13.2.
- [42] B. Zhu, Dow Performance Silicones, Private Conversation, (2017).
- [43] J. Plott, X. Tian, A.J. Shih, Voids and Tensile Properties in Extrusion-based Additive Manufacturing of Moisture-Cured Silicone Elastomer, *Addit. Manuf.* (2017). Submitted.
- [44] W. Michaeli, *Extrusion Dies for Plastics and Rubber Design and Engineering Computations*, Carl Hanser Verlag GmbH & Co. KG, 2003.
- [45] A. Bellini, Fused deposition of ceramics: A comprehensive experimental, analytical and computational study of material behavior, fabrication process and equipment design, 2002. doi:10.16953/deusbed.74839.
- [46] B. N. Turner, R. Strong, S. A. Gold, A review of melt extrusion additive manufacturing processes: I. Process design and modeling, *Rapid Prototyp. J.* 20 (2014) 192–204. doi:10.1108/RPJ-01-2013-0012.
- [47] R.C. Hibbeler, *Statics and Mechanics of Materials*, Pearson Prentice Hall, 2004.
- [48] K. Grundke, S. Michel, G. Knispel, A. Grundler, Wettability of silicone and polyether impression materials: Characterization by surface tension and contact angle measurements, 317 (2008) 598–609. doi:10.1016/j.colsurfa.2007.11.046.